




ADVERTIMENT. L'accés als continguts d'aquesta tesi queda condicionat a l'acceptació de les condicions d'ús establertes per la següent llicència Creative Commons:  <https://creativecommons.org/licenses/?lang=ca>

ADVERTENCIA. El acceso a los contenidos de esta tesis queda condicionado a la aceptación de las condiciones de uso establecidas por la siguiente licencia Creative Commons:  <https://creativecommons.org/licenses/?lang=es>

WARNING. The access to the contents of this doctoral thesis it is limited to the acceptance of the use conditions set by the following Creative Commons license:  <https://creativecommons.org/licenses/?lang=en>

UNIVERSITAT AUTONÒMA DE BARCELONA

DOCTORAL THESIS

Flexoelectricity in two-dimensional materials from Density Functional Perturbation Theory

Author:

Matteo SPRINGOLO

Supervisors:

Dr. Massimiliano STENGEL

Dr. Miquel ROYO

Tutor:

Dr. Aitor LOPEANDIA

*A thesis submitted in fulfillment of the requirements
of the PhD in Physics program of the UAB
in the*

Institut de Ciència de Materials de Barcelona

Academic Year 2023/2024

Contents

Resumen	v
Summary	v
1 Introduction	5
2 Methodological framework	9
2.1 Density Functional Theory	9
2.1.1 Energy of an interacting many-body system	9
2.1.2 The Hohenberg-Kohn theorems	11
2.1.3 The Kohn-Sham auxiliary system	11
2.1.4 The exchange and correlation functional	12
2.2 Practical methods for ground-state calculations	13
2.2.1 Bloch theorem and Brillouin-zone integration	13
2.2.2 Plane-wave basis set	14
2.2.3 Pseudopotentials	15
2.3 Density Functional Perturbation Theory (DFPT)	16
2.3.1 Sternheimer equation	16
2.3.2 Second-order energy and its variational formulation	17
2.3.3 Monochromatic perturbations and factorization of the phase	18
2.4 Specific perturbations	19
2.4.1 Phonons	19
2.4.2 Electric field perturbation	20
2.4.3 Uniform strain perturbation	21
2.5 Long-wave DFPT	22
2.5.1 Treatment of inhomogeneous strain	22
2.5.2 Treatment of inhomogeneous polarization from current-density	23
2.5.3 Spatial dispersion from analytical \mathbf{q} -expansion	24
3 First-principles theory of flexoelectricity	27
3.1 General definitions: deformations, strain and strain gradients	28
3.2 Macroscopic flexoelectric coefficients in 3D crystals	28
3.2.1 Bulk flexoelectric tensor from long-wave acoustic phonons	29
3.2.2 Dynamical nature of the effect	31
3.2.3 Treatment of the macroscopic electric field	32
3.3 Treatment of finite samples in curvilinear coordinates	33
3.3.1 General principles	33
3.3.2 Curvilinear electrostatics	34
3.3.3 Perturbative expansion	34
3.3.4 3D flexovoltage	36

4	Out-of-plane response	39
4.1	Flexural deformations in quasi-2D materials	39
4.1.1	Nanotube geometry	39
4.1.2	Curvature tensor	40
4.2	Flexovoltage in 2D crystals	42
4.3	Electric Boundary Conditions	43
4.4	First-principles theory and methods	44
4.4.1	Clamped-Ion and Lattice-Mediated contributions	45
4.5	Computational parameters	46
4.6	Results	48
4.6.1	Generalized-gradient approximation	49
4.7	Consistency checks	50
4.7.1	The longitudinal case	50
4.7.2	Nanotube calculations	51
4.8	An illustrative toy model: Xe monolayer	52
4.9	Coupling between out-of-plane electric fields and flexural phonons	55
4.9.1	Macroscopic electric fields in 2D	55
4.9.2	Flexovoltage	57
4.9.3	Converse flexoelectric effect in 2D	57
4.9.4	Continuum modeling of PFM experiments	58
5	In-plane response	61
5.1	2D in-plane polarization field	61
5.2	Symmetry requirements and D_{3d} crystals	62
5.3	First-principles theory	65
5.3.1	Clamped-ion 2D flexocoefficient	65
5.3.2	Lattice-mediated 2D flexocoefficient	66
5.4	Computational results	66
5.4.1	Generalized-gradient and Van der Waals XC functionals	68
5.5	Consistency check and comparison with second-order effect	69
5.6	Topological in-plane polarization in rippled D_{3d} crystals	70
5.7	Spontaneous polarization in D_{3d} crystal nanotubes	72
6	Conclusions	75
A	Out-of-plane response	79
A.1	Clamped-ion and lattice-mediated coefficients	79
A.1.1	Bulk flexoelectric tensor in 3D	79
A.1.2	From SC to mixed-EBCs	80
A.2	Supplemental results	82
A.2.1	Analysis of the clamped-ion contribution	82
A.2.2	Analysis of the lattice-mediated contribution	83
A.2.3	Toy model	84
B	In-plane response	87
B.1	Relation to type-I bulk flexocoefficients	87
B.2	Nontrivial topological examples	87
B.2.1	Single Gaussian bump	88
B.2.2	Hexagonal lattice of Gaussian bumps	89
B.2.3	Three-phonon perturbation	90
	Case 1	90

Case 2	90
Case 3	91

List of Figures

2.1	Illustration of the coordinate transformation to the comoving frame. (a) Unperturbed crystal lattice; black circles represent the atomic sites, horizontal and vertical lines represent the coordinate system. (b) Transverse acoustic phonon in the laboratory frame. (c) The same phonon in the curvilinear frame; note that the atoms do not move in this coordinate system: the mechanical deformation is described via the metric.	23
3.1	Bending of a finite slab. The electric field induced within the surface- and bulk-regions of the sample is schematically shown. The surface and bulk electric fields are discussed in more detail in Fig.3.2.	37
3.2	Macroscopic electric, (a)-(c), and potential, (b)-(d), fields induced in the slab by a uniform strain, (a)-(b), and a uniform strain-gradient, (c)-(d), respectively. In panel (c) the surface and bulk contributions to the induced electric field are separately shown.	37
4.1	Illustration of the macroscopic deformation field in a vicinity of a bent layer; the two-dimensional crystal is indicated by a thicker red curve.	39
4.2	Schematic illustration of the flexoelectric response in BN. (a): Cross-section of a BN nanotube; the voltage drop between its inner and outer sides is highlighted. (b): Flexural phonon, corresponding to an in-plane modulation of the same strain field as in (a). (c): Lattice-mediated and purely electronic effects contributing to the dipole. Gray/green circles represent the B/N atoms. The deformed electronic orbitals are shown as yellow shaded ellipses.	43
4.3	Top and side view of the crystal structures used in the calculations. (a) graphene, (b) silicene, (c) BN, (d) phosphorene, (e) MoS ₂ and (f) SnS ₂	47
4.4	Convergence of clamped-ion (a) and lattice-mediated (b) MoS ₂ flexovoltages as a function of the in-plane \mathbf{k} -points mesh resolution. A plane-wave cutoff of 80 Hartree was employed in the calculations.	48
4.5	Clamped-ion flexovoltage coefficient calculated as $\varphi = \Delta V R$, plotted as a function of the nanotube radius R . Our linear-response result [Eq. (4.27)] is shown as a red line. The inset shows φ as a function of $1/R$, the dashed line being a linear extrapolation from the last two calculated points to $R \rightarrow \infty$	52
4.6	Crystal structure of the hexagonal Xe monolayer discussed in the text.	52

4.7	Computed values for $\varphi^{(M)}$, $\varphi^{(D)}$, $\varphi^{(tot)}$ (nVm) and the analytical curves given by $(\mp Q[\rho^{(Xe)}]/2\epsilon_0)$, as a function of the increasing in-plane lattice constant. $Q[\rho^{(Xe)}]$ is the quadrupolar moment of the isolated atom divided by the unit cell surface $S \propto a^2$. The inset shows the computed values of the “total” flexovoltage, otherwise indistinguishable from zero, being three orders of magnitude smaller than the dipolar and metric terms reported in the figure.	53
4.8	Impact of curvature on the charge density of a rigid spherical object. For illustration purposes, we use a Gaussian function centered in the origin of the type $\phi(\mathbf{r}) = \frac{1}{\pi\sigma^2}e^{-r^2/\sigma^2}$. (a): Cartesian representation; the dashed curve indicates the curved layer plane. (b): curvilinear $\hat{\rho}(\mathbf{r})$ as defined in Eq. (4.40); the deformation of the original Gaussian is clear. (c): first-order variation of $\hat{\rho}(\mathbf{r})$	54
4.9	Atomic forces induced by a spatially modulated transverse electric field on a BN monolayer in its unperturbed equilibrium structure. Modulation periods of 24 (left) and 12 (right) cells are shown. Black circles and red squares refer to B and N atoms, respectively. Solid curves are fits to the data (see text).	58
4.10	Amplitude of the flexural phonon response to an externally applied transverse electric field of 1 GV/m, modulated at a given in-plane wavevector q . Results for $g = 10^{-1}$ eV/Å ⁴ (black), $g = 10^{-2}$ eV/Å ⁴ (red), $g = 10^{-3}$ eV/Å ⁴ (green) and the free-standing layer (dashed) are shown.	59
5.1	(a) Schematic illustration of a slab bent along the (principal) direction λ_1 with a (principal) curvature K_1 . Red arrows indicate the principal bending directions. (b) 2D geometry for SnS ₂ . θ indicates the angle between the axis x and the principal direction λ_1 . The induced in-plane polarization $P_{ }$ is indicated for an angle $\theta = 15^\circ$. (c) Orientation evolution of the induced in-plane polarization with respect to the bending direction (θ). Threefold symmetry is highlighted by use of blue lines.	62
5.2	Top view of the crystal structures employed in the linear-response calculations for the materials considered. The primitive cell is highlighted. Upper and lower atoms of the same type are indicated with the same color but different shade. Upper atoms are explicitly indicated with an asterisk.	63
5.3	Convergence of the CI (a) and LM (b) independent component $ \mu $ as a function of the in-plane \mathbf{k} -points mesh resolution, for SnS ₂	67
5.4	Rippled surface and the related in-plane polarization induced within the material. The reported ripple corresponds to a superposition of three sinusoidal deformations, as described in the upper side of figure 5.6 (refer to the same figure for color scale details). The induced in-plane polarization field corresponds to an hexagonal lattice of clockwise vortices, each described by a winding number $Q = 1$ and centered in correspondence of the 1D nodes of the ripple (see Fig) 5.6.	70

- 5.5 Top and bottom left panels: Polarization texture associated with a single Gaussian bump of the type $z = Ae^{-(x^2+y^2)/\sigma^2}$ and an hexagonal lattice of Gaussian bumps of the same type. The arrows indicate the polarization direction, its amplitude (in units of $|P_{\parallel}|^{\max} \simeq 1.48 \frac{A\mu}{\sigma^2}$ and $|P_{\parallel}|^{\max} \simeq 6.94 \frac{A\mu}{\sigma^2}$ respectively) is defined by the color scale. Top and bottom right panels: Contour plot for the considered deformation. Their amplitudes (in units of $u_z^{\max} = A$ and $u_z^{\max} \simeq 1.11A$ respectively) are defined by the color scale. 71
- 5.6 Top and bottom left panels: Polarization texture associated with two periodic patterns of the type $z = A \sum_{i=1}^3 \sin(\mathbf{q}_i \cdot \mathbf{r})$, with $\mathbf{q}_1 = q(1, 0, 0)$, $\mathbf{q}_2 = q(-1/2, \sqrt{3}/2, 0)$, $\mathbf{q}_3 = q(-1/2, -\sqrt{3}/2, 0)$, and $\mathbf{q}_1 = q(\sqrt{3}/2, 1/2, 0)$, $\mathbf{q}_2 = q(-\sqrt{3}/2, 1/2, 0)$, $\mathbf{q}_3 = q(0, -1, 0)$ respectively. $q = 2\pi/L$. The arrows indicate the polarization direction, its amplitude (in units of $|P_{\parallel}|^{\max} = 1.75A\mu q^2$) is defined by the color scale. Top and bottom right panels: Contour plot of the periodic deformations considered. Their amplitudes (in units of $u_z^{\max} \simeq 2.6A$) are defined by the color scale. 72
- 5.7 Nanotube constructed by folding a SnS₂ layer along its zigzag direction. The fully axial spontaneous polarization is schematically sketched. 73
- B.1 Amplitude of the in-plane polarization field induced by a Gaussian bump, as a function of the radial coordinate and in units of $\frac{A\mu}{\sigma^2}$ 89

List of Tables

4.1	Equilibrium structural parameters for the unperturbed flat configuration of the materials considered in this work. h corresponds to the thickness of the buckled materials.	46
4.2	Clamped-ion (CI), lattice-mediated (LM) and total flexovoltages (nV·m) of the 2D crystals studied in this work. Due to its lower symmetry, for phosphorene two independent bending directions (armchair and zigzag) exist.	48
4.3	Interlayer spacing in the bulk (extracted from Ref. (1)), total flexovoltage and volume-averaged flexoelectric coefficient of the 2D crystals studied in this work. Data between round brackets in the third column has been extracted from the literature: ^a Ref. (2), ^b Ref. (3), ^c Ref. (4), ^d Ref. (5)	49
4.4	GGA values of the clamped-ion (CI), lattice-mediated (LM) and total flexovoltage (nV·m) coefficients of the 2D crystals studied in this work.	50
4.5	Decomposition of the longitudinal (zz,zz) flexovoltage coefficients, Eq.(4.38).	51
4.6	Explicit calculation of the converse flexoelectric effect. Z_κ are the fitted atomic forces in response to the modulated field; $\bar{\mu}^{2D}$ is the estimated clamped-ion flexoelectric coefficient calculated according to Eq. (4.57). All values are in units of electron charge.	58
5.1	Primitive-cell atomic structures, expressed in reduced coordinates, for the materials considered in this work. h refers to the parameter reported in Table.5.2, except for BN-bilayer where B and N occupy sublattices positions described by slightly different z-components ($h_B = 3.0661$ Bohr and $h_N = 3.0703$ Bohr for B and N respectively).	64
5.2	Equilibrium structural parameters for the unperturbed flat configuration of the materials considered in this work. h corresponds to half the thickness of the buckled materials.	67
5.3	Characteristic 2D flexocoefficients due to a flexural deformation. Three left-most columns show the Clamped-Ion(CI), Lattice-Mediated(LM), and Relaxed-Ion(RI) contributions to the in-plane response $\mu_{yz,xx}^{2D}$. Fourth column shows the out-of-plane RI response, $\mu_{zz,xx}^{2D}$. Results are provided in units of electronic charge.	68

5.4	Calculated 2D flexoelectric coefficients within PBE. Left columns show the Clamped-Ion(CI), Lattice-Mediated(LM), and Relaxed-Ion(RI) contributions to the in-plane response $\mu_{yz,xx}^{2D}$. The right column shows the out-of-plane RI response, $\mu_{zz,xx}^{2D}$. Results are provided in units of electronic charge. 2-BN corresponds to the BN bilayer, which we calculated either directly or by means of the piezoelectric model ($\mu^{2D} = Eh$) within PBE. The values of the CI and LM longitudinal piezoelectric constant are $E^{CI} = 0.1208$ e/bohr and $E^{LM} = -0.0749$ e/bohr, respectively, in good agreement with the LDA values reported in the main text. The calculated PBE interlayer distance is $h = 8.29$ bohr.	69
5.5	Results from direct calculations for nanotubes of two different radii R [in bohr] (two top rows) and from the linear-response calculation (bottom row). The two left-most columns show the average axial forces [times R and in hartree units] on the Sn and S atoms. The two right-most columns show the clamped-ion and lattice-mediated 1D axial nanotube polarizations [in e]. Direct 1D polarizations are calculated as $\Omega P_z / c$, with Ω , c and P_z being, respectively, the volume, dimension and 3D polarization component along the axial direction of the simulation supercell. In turn, linear response ones are calculated with Eq.(5.20) of the main text.	73
A.1	Decomposition of the clamped-ion flexovoltage coefficient, φ^{CI} , into the three contributions of Eq.(4.27).	83
A.2	Dynamical charge (Z), flexocoupling coefficient (f) and ZO mode stiffness (a) for selected materials (atomic units) calculated with LDA and GGA. The sign of the polar mode eigenvector is set in such a way that the cation moves outwards.	84

List of Abbreviations

FxE	FlexoElectricity
DFT	Density Functional Theory
DFPT	Density Functional Perturbation Theory
HK	Hoheneberg-Kohn
KS	Kohn-Sham
LDA	Linear Density Approximation
GGA	Geleralized Gradient Approximation
BvK	Born- von Karman
PBCs	Periodic Boundary Conditions
BZ	Brillouin Zone
3D	3-Dimensional
2D	2-Dimensional
EBCs	Electric Boundary Conditions
OC	Open - Circuit
SC	Short - Circuit
r.h.s.	right hand side
l.h.s.	left hand side
H	Hartree
xc	exchange - correlation
Hxc	Hartree and exchange - correlation
psp	pseudopotential
loc	local
NL	Non-Local
sep	separable
KB	Kleinman - Bylander

Resumen

En esta tesis desarrollamos un método general para calcular la respuesta flexoeléctrica de un material bidimensional (2D) en respuesta a una deformación flexural. Tal respuesta eléctrica ha sido generalmente definida y calculada como un momento dipolar inducido a lo largo de la dirección fuera del plano. Sin embargo, el cálculo del momento dipolar de un cristal 2D doblado sufre de diversas ambigüedades que han conllevado un alto grado de desacuerdo entre los resultados previamente publicados. Además, esta definición como dipolo tiene un uso práctico limitado, ya que es difícil establecer su relación con los parámetros medidos experimentalmente, a saber, campos y potenciales eléctricos.

Aquí resolvemos estos problemas definiendo y calculando la respuesta, a lo largo de la dirección fuera del plano, de un material 2D como el voltaje de circuito abierto (flexovoltaje) en respuesta a una curvatura. Haciendo uso de implementaciones de flexoelectricidad 3D recientemente desarrolladas en nuestro grupo de investigación, demostramos que el flexovoltaje de una capa de material 2D es una propiedad de respuesta lineal intrínseca del cristal, y que puede ser calculada en el contexto de la Teoría del Funcional de Densidad partiendo de la celda primitiva sin deformar. De este modo, nuestro formalismo elimina la necesidad de usar estructuras dobladas de gran tamaño, como por ejemplo nanotubos, las cuales requieren una alta carga computacional. Mediante la aplicación de nuestro formalismo al estudio de sistemas tales como grafeno, siliceno, fosforeno, nitruro de boro, y dicalcogenuros de metales de transición, demostramos que la respuesta flexoeléctrica se compone de dos contribuciones distintas: una de naturaleza puramente electrónica y otra debida al relajamiento de los grados de libertad iónicos. En la contribución electrónica, aparece un término métrico, correspondiente al momento cuadrupolar de la densidad de carga no perturbada, que resulta esencial para alcanzar una descripción física sólida. Entre nuestras simulaciones numéricas, también incluimos el estudio de un modelo físico intuitivo y de resolución analítica que nos permite demostrar la validez de nuestra definición física de flexovoltaje como respuesta flexoeléctrica físicamente consistente. Además, demostramos que los coeficientes de flexovoltaje describen sea el efecto flexoeléctrico directo que el inverso, y aprovechamos esta dualidad para construir un modelo continuo que conecta nuestros resultados numéricos con las medidas experimentales disponibles obtenidas a través de la técnica de microscopía de fuerza piezoeléctrica.

Adicionalmente, identificamos las condiciones de simetría bajo las cuales un cristal 2D desarrolla una polarización en el plano en respuesta a una deformación flexural, y presentamos un método general para calcular los coeficientes que describen este efecto físico. Aplicando nuestro método a una serie de cristales 2D con simetría D_{3d} , descubrimos que el módulo de la polarización en el plano es hasta un orden de magnitud más grande que la componente a lo largo de la dirección fuera del plano, en el mismo material. Además, la amplitud de la respuesta en el plano es independiente de la dirección a lo largo de la cual se dobla el material, mientras que su orientación rota de manera continua en el plano con una periodicidad que es compatible con la simetría del cristal no perturbado. Como consecuencia de esta

simetría, encontramos que *i*) los cristales D_{3d} presentan una textura de polarización topológica en el plano cuando son deformados con una ondulación genérica y *ii*) los nanotubos contruidos doblando este tipo de materiales presentan una polarización espontánea.

Summary

In this thesis we provide a general and powerful method to calculate the flexoelectric response of a two-dimensional (2D) material to a flexural deformation. Such electrical response has been mostly defined and calculated as the out-of-plane dipolar moment induced in the deformed layer. However, calculating the dipole moment of a curved crystalline slab is not free from ambiguities, and this fact has led to a remarkable scattering of the reported results. In addition, such a definition has limited practical value since it is difficult to establish its relationship with the experimentally relevant parameters, namely, electric fields and potentials.

Here, we overcome the aforementioned issues by defining and calculating the out-of-plane flexoelectric response of a quasi-2D material in terms of the open-circuit voltage ("flexovoltage") in response to curvature. Building on implementations of bulk flexoelectricity recently developed in our group, we show that the flexovoltage coefficient is a fundamental linear-response property of the crystal, that can be calculated in the framework of Density Functional Perturbation Theory by using the primitive 2D cell of the unperturbed flat layer. In this way, our formalism eliminates the need to use large bent structures (e.g., nanotube geometries) that can be computationally very demanding. By applying our approach to graphene, silicene, phosphorene, boron nitride, and transition-metal dichalcogenides, we reveal that the flexoelectric response is composed of two distinct contributions: one of purely electronic nature and another originated in the relaxation of the lattice degrees of freedom. Within the former, we identify a key metric term, consisting in the quadrupolar moment of the unperturbed charge density, that becomes essential to reach a meaningful physical description. Among our numerical simulations, we also consider an intuitive toy model analytically solvable that allows us to corroborate the validity of our definition of flexovoltage as a physically consistent flexoelectric response. We also prove that the flexovoltage coefficients describe both the direct and converse flexoelectric effect; a fact that we exploit to build a continuum model that connects our numerical results with the available experimental measurements obtained via piezoelectric-force microscopy.

In addition, we identify the symmetry conditions for a 2D crystal to develop an in-plane polarization response to a flexural deformation, and provide a general method to calculate the characteristic flexoelectric coefficients describing such an effect. By applying our method to a set of 2D crystals of the D_{3d} point group, we find that the ensuing response is up to one order of magnitude larger than the out-of-plane component in the same material. Besides, the polarization magnitude turns out to be insensitive to the bending direction, while its orientation continuously rotates in plane with an angular periodicity that matches the threefold axis of the flat configuration. As a consequence of this symmetric behavior, we find that *i*) D_{3d} crystals are endowed with topologically nontrivial in-plane polarization textures when rippled and *ii*) nanotubes constructed by folding these kind of materials are spontaneously polarized.

Chapter 1

Introduction

Electromechanical phenomena are ubiquitous in biology, materials science and engineering. Generating electrical signals in response to a deformation and viceversa is necessary for the living organisms to perform basic functions, such as hearing and muscle contraction, and is also the basic working principle of popular commercial devices, including sensors, actuators and energy harvesters. (6) Until very recently, when referring to electromechanical properties, one generally meant piezoelectricity and/or electrostriction-coupling of homogeneous deformation to the polarization or the square of polarization, respectively. These two effects have already a long history and, in spite of the many open questions that still exist (7), their fundamentals can now be considered well established.

The coupling between polarization and strain gradient, known as flexoelectricity (FxE), has also been known for quite some time (the effect was predicted by Kogan in 1964 (8), and the inverse effect of bending of a parallel-plate capacitor induced by an applied voltage experimentally demonstrated in 1968 by Bursian et al. (9)), but it has traditionally been regarded as a very weak effect, hardly detectable in macroscopic samples. Only in the past few years research has taken off on this front, triggered by the measurement in Penn State of unexpectedly large flexoelectric coefficients in some electroceramics such as (Ba, Sr)TiO₃ (10), and finally impelled by the breathtaking progress in the design and control of nanoscale structures. Since the uniform strain gradient that can be sustained by a sample before material failure is inversely proportional to its thickness, scaling down the active elements implies enhancing the FxE effect by orders of magnitude. Another particularly enticing characteristic of flexoelectricity is its universality: unlike piezoelectricity, it occurs in any insulating material regardless of its crystal symmetry. Meanwhile, the appeal of flexoelectricity is not only limited to its potential application in pseudo-piezoelectric (6; 11; 12), units; in fact the peculiar symmetry of the FxE tensor points to new functional properties that are qualitatively different from other forms of electromechanical coupling, with applications, e.g. in high-density information storage. (13)

The above considerations imply that two-dimensional (2D) materials such as boron nitride, graphene or a MoS₂ sheet should be among the strongest flexoelectric systems available on the market: One simply cannot go any thinner (or more flexible) than this. There is a strong fundamental motivation as well: Indeed, curvature is ubiquitous in 2D layers, either in form of spontaneous rippling or thermal population of flexural modes, which implies a potentially strong impact of flexoelectricity on their physical properties - even beyond electromechanics. To verify these hypotheses, a quantitative understanding of the flexoelectric effect in 2D crystals, and in particular of the out-of-plane dipolar response to curvature, appears essential. Several authors have taken on this challenge in the past few years, both experimentally and theoretically.

Recently, several experimental works (14; 15; 16) reported a significant out-of-plane electromechanical response in graphene, BN, transition-metal dichalcogenides (TMDs) and related materials. These materials are all nonpiezoelectric, so flexoelectricity was identified as the most natural explanation for the effect. Most measurements were performed via piezoelectric force microscopy (PFM) of supported films on various substrates. The converse effect (deformations in response to an applied voltage) was generally probed, and quantified in terms of an effective piezoelectric coefficient, d_{33}^{eff} . These studies have been hardly conclusive regarding the magnitude of the intrinsic flexoelectric coefficient of the 2D layer, though. First, the presence of a substrate implies that the mechanical response of the layer is (at least) partially clamped due to interaction, whose impact on d_{33}^{eff} remains poorly understood. Second, flexoelectricity is a non-local effect, where electromechanical stresses depend on the gradients of the applied external field. It is natural then to expect that the magnitude of such gradients will depend critically on the details (shape, size, material) of the PFM tip, and this substantially complicates the analysis. Unless these questions are settled by establishing reliable models of the converse flexoelectric effect in 2D crystals, the interpretation of the experimental data remains to a large extent speculative, which severely limits further progress towards a quantitative understanding.

Theoretical simulations are a natural choice to shed some light on the aforementioned issues. Several groups have studied flexoelectricity in a variety of monolayer crystals including graphene, hexagonal BN, and transition metal dichalcogenides; calculations were performed either from first principles (17; 18; 4; 19; 5; 3) or by means of classical force fields. (2; 20) Unfortunately, the reported results for any given material wildly disagree both in magnitude and sign. There are several reasons that may explain the disagreement between different computational strategies. First and foremost, the very definition of the dipole moment of a curved layer is problematic, since the textbook Cartesian expression is clearly inapplicable. Some authors have advocated a reformulation of the latter in cylindrical coordinates, which solves some of the existing issues; however, how the resulting "radial dipole" of the layer relates to the experimentally measured properties (which typically depend on the interaction with an external electrostatic potential) remains to be seen. Second, many studies have adopted large-scale calculations on isolated samples that were heuristically bent by imposing a variety of constraints on the atomic positions. Such strategies raise the obvious questions of how the applied constraints may affect the calculated values, and of possible contributions from boundary effects; neither issue was convincingly dealt with thus far.

Meanwhile, there are several indications from the theory that a flexural deformation may induce an in-plane polarization response as well under some specific conditions. Several years ago, for example, Naumov *et al.* (18) predicted a large in-plane flexoelectric response in monolayer BN, occurring at nonlinear order in the applied curvature. Soon afterwards, Duerloo *et al.* (21) demonstrated that a linear in-plane polarization response to curvature is present in bilayer BN, and explained it in terms of the piezoelectric response of the constituent layers. These findings are intriguing, in that such a response is forbidden by symmetry in most three-dimensional (3D) bulk material that were considered thus far in the context of flexoelectricity. Illustrations of the effect were reported only for one material (BN), though, and no criteria to identify other candidate systems (let alone to quantify the magnitude of the response therein) were known at the time this thesis started.

Thanks to the considerable recent progress in the computational methods, (22; 23; 24; 25; 26; 27; 28) addressing these questions in the framework of first-principles linear-response theory appears now well within reach. Within a handful of years

prior to this thesis, the theory and methods to calculate flexoelectric properties of solids had evolved from a pioneering explorative stage to a full-fledged implementation in ABINIT, a publicly distributed community code. Thanks to a number of fundamental advances in the treatment of inhomogeneous strains (22; 25) and polarizations (24), and on the development of a powerful long-wavelength approach (27; 28) to capture their coupling at leading order in the gradient expansion, the flexoelectric coefficients are now part of the standard toolkit of density-functional perturbation theory (DFPT). Both purely electronic and lattice-mediated contributions to the effect can be calculated with the same ease and accuracy as the traditional workhorses of linear-response methods, e.g., phonons or dielectric constants. All in all, this was a particularly timely moment, where new methods became available and opened a wealth of exciting opportunities in the framework of first-principles theory; this thesis is indeed aimed at building on such a potential.

Yet, at the time this thesis started, most of the fundamental developments had targeted bulk 3D crystals, and adapting them to the specifics of 2D systems was a clear prerequisite to performing the actual calculations we had in mind. Note that the relevant theory and computational framework to deal with a finite membrane (which can be regarded as a special case of a 2D geometry) did already exist; (29; 23; 26) these, however, were only applicable to the limit of a macroscopically thick sample, where the surfaces can be clearly identified and treated separately from the inner bulk. Such a separation is clearly not possible in the case of a truly 2D layer, which is atomically thin along the out-of-plane coordinate. Overcoming this limitation was the first task we had to face, and a significant part of this thesis is dedicated to reporting on our formal and methodological work in this direction. It is important to stress that this activity was not only technical, but involved a great deal of conceptual challenges. First and foremost, we had to establish a proper definition of the flexoelectric effect in 2D that do not suffer from the aforementioned drawbacks. Second, we had to make sure that our results were physically sound, by devising appropriate benchmarks (also in the form of analytically solvable toy models) to test our qualitative conclusions in some well-defined limits. As we said, experimental values on 2D systems are still scarce and unreliable: this is a clear case where "we were on our own" in making sure that our predictions provide a solid reference for future studies, and are state-of-the art within the approximations to density-functional theory that we adopted in each case.

(Outline.) In Chapter 2, we describe the underlying methodological framework of the fundamental developments presented in this thesis. In particular, after reviewing the basics of Density Functional Theory (DFT) and Density Functional Perturbation Theory (DFPT), we summarize three preexisting methodological milestone studies in the field of first-principles simulations of spatial dispersion: the treatments of inhomogeneous strains and inhomogeneous polarization responses to monochromatic perturbations, and a long-wavelength analytical approach to spatial-dispersion properties. In Chapter 3, we review the first-principles theory of bulk flexoelectricity and then incorporate the surface contributions, along with a curvilinear coordinates formalism to deal with them, that participate in the total flexoelectric response of real (finite) samples. In Chapter 4, we first discuss the formal treatment of flexural deformations from a geometrical point of view. Then, we develop the theoretical formalism to calculate the out-of-plane response of a quasi-2D material to a flexural deformation, analyze our numerical results and provide tests that validate our method. Finally, we illustrate the relevance of the physical quantities we define and

calculate by formally connecting them with the electrical signals experimentally detected with a piezoresponse force microscopy. In Chapter 5, we study the in-plane polarization response to a flexural deformation, identifying the symmetry requirements for the effect to be observed, and provide and analyze our numerical results. Then, we discuss two physical implications of the effect: the topological character of the polarization field induced in arbitrary rippled quasi-2D D_{3d} crystals, and the appearance of a spontaneous polarization in nanotube structures constructed by folding this kind of materials. Finally, in Chapter 6, we discuss the relevance of our achievements and outline the possible future outlooks.

Chapter 2

Methodological framework

In this chapter we will provide the basics concerning the methodological background that constitute the building blocks needed to develop the methods presented in this work. After revising the fundamentals of Density Functional Theory and its perturbative version (Density Functional Perturbation Theory) in their general form, we consider their application to crystal systems and inspect the special cases regarding the perturbations that are relevant for our purposes. Finally, we illustrate the methodological achievements that allowed the calculation of spatial dispersion properties within a first-principles framework.

2.1 Density Functional Theory

The appeal of Density Functional Theory (DFT), whose modern formulation was provided by Hohenberg and Kohn in 1964 (30), lies in the fact that any property of a quantum system of interacting electrons can be expressed as a *functional* of the ground state electronic particle-density. However, while DFT is in principle built as an exact theory of many-body systems, no prescriptions on how one can construct the required functionals is provided, and the exact form of the latter are generally unknown. The aforementioned issue was overcome by Kohn and Sham (31). They considered the existence of an effective equivalent auxiliary independent-particle system and provided a scheme to obtain approximated forms for the sought-after functionals. In the following we will summarize the principal results of DFT that enable one to perform practical calculations on electron-structure in solid-state physics.

2.1.1 Energy of an interacting many-body system

Let us consider a generic system composed of M ions and N electrons, both considered as quantum point-like particles. The (stationary) non-relativistic energy of such a system can be written, in full generality, as

$$E = E[\Psi] = \langle \Psi | \hat{H} | \Psi \rangle, \quad (2.1)$$

where $|\Psi\rangle$ is the many-body quantum state referring to both the ionic and electronic degrees of freedom and solution of the time-independent Schrödinger equation associated to the Hamiltonian operator \hat{H} describing the quantum system,

$$\hat{H}|\Psi\rangle = E|\Psi\rangle, \quad (2.2)$$

$$\hat{H} = \hat{T}_i + \hat{T}_e + \hat{V}_{ii} + \hat{V}_{ee} + \hat{V}_{ie}. \quad (2.3)$$

\hat{T}_i and \hat{T}_e are the kinetic energy operators of the ionic and electronic subsystems respectively, while \hat{V}_{ii} , \hat{V}_{ee} and \hat{V}_{ie} are the potential energy operators corresponding to the ion-ion, electron-electron, and ion-electron Coulomb interactions respectively. The notation $E[\Psi]$ indicates that the quantum energy E is a functional of the $(M + N)$ -particle wave-function $\Psi([\alpha])$, with $[\alpha]$ indicating the many-body variables within the space of degrees of freedom (ionic and electronic) the wave-function can be represented on.

In order to solve Eq.(2.2) the Born-Oppenheimer approximation is generally assumed. (32) Within the latter an electron is supposed to remain always in a given quantum state, despite the change in the ionic degrees of freedom: *even if the electronic wavefunction and energy can change, no excitations occur*. Such a approximation allows one to decouple the eigenvalues problem (Eq.(2.2)) and solve it separately for the ionic and electronic degrees of freedom respectively. In such a way the two kinds of different degrees of freedom depend each other in a parametric way. In the following, we shall also consider the ions as classical point-like particles. The quantum energy of the N electrons is the given by

$$E_e[\psi] = \langle \psi | \hat{H}_e | \psi \rangle, \quad (2.4)$$

$$\hat{H}_e = \hat{T}_e + \hat{V}_{ee} + \hat{V}_{ie}. \quad (2.5)$$

where \hat{V}_{ie} plays the role of an external potential for the electronic subsystem (we shall refer to it as \hat{V}_{ext} henceforth), while $|\psi\rangle$ and $E_e[\psi]$ are the electronic eigenvectors and eigenvalues, respectively, associated to the electronic Schrödinger equation, $\hat{H}_e|\psi\rangle = E_e|\psi\rangle$. The external potential \hat{V}_{ext} depends parametrically on the spatial configuration describing the ionic subsystem (classic) state, that in turn introduces a parametric dependence of the electronic solutions $|\psi\rangle$ and $E_e[\psi]$ (the latter known as Born-Oppenheimer surface) on the ionic (spatial) degrees of freedom $[R]$ through the eigenvalue problem,

$$\hat{H}_e([R])|\psi([R])\rangle = E_e([R])|\psi([R])\rangle. \quad (2.6)$$

In the following we will assume the electronic system as nonmagnetic, and reduce our focus on the orbital degrees of freedom ($[\alpha_{el}] = [r] = (\mathbf{r}_1, \dots, \mathbf{r}_N)$). We also consider the system as embedded in the 3D space.

From the invariance of the electronic Hamiltonian under exchange of particles (the electrons are identical by definition) and the locality of \hat{V}_{ext} , one finds that the electronic energy related to the external potential $E_{ext}[\psi] = \langle \psi | \hat{V}_{ext} | \psi \rangle$ can be written as a *functional* of the *particle density* field $n(\mathbf{r})$,

$$\begin{aligned} E_{ext}[\psi] &= E_{ext}[n] = \int d^3r V_{ext}(\mathbf{r}) n(\mathbf{r}), \\ n(\mathbf{r}) &= N \int [d^3r']^{N-1} |\psi(\mathbf{r}, [\mathbf{r}']^{N-1})|^2. \end{aligned} \quad (2.7)$$

Here $[\mathbf{r}]^{N-1} = (\mathbf{r}_{i_1}, \dots, \mathbf{r}_{i_{N-1}})$ indicates an element of the vectorial space corresponding to the Cartesian product $\mathbb{R}^{d(N-1)}$, d being the dimensionality of the space where the system is embedded in (in this case $d = 3$). Notice that, from the normalization condition $\langle \psi | \psi \rangle = 1$, we have $\int d^3r n(\mathbf{r}) = N$, consistent with the definition of the particle density.

2.1.2 The Hohenberg-Kohn theorems

Density Functional Theory builds on two theorems proved by Hohenberg and Kohn.⁽³⁰⁾ The **first theorem** states that two external potentials that differ by more than a constant induce different Ground State particle densities. This means that there exist a one-to-one correspondence between $[V_{ext}]$ and $[n_0]$. From this fact follows that there exists a universal (in the sense that is the same for any electronic system) *functional* of $[n_0]$, $F[n_0]$, such that $(T + V_{ee})[\psi] = F[n_0]$ and then the electronic energy can be written through the Hohenberg-Kohn (HK) functional as

$$E_e[\psi] = E_e^{HK}[n] = F[n] + \int d^3r V_{ext}(\mathbf{r})n(\mathbf{r}). \quad (2.8)$$

The **second theorem** states that the exact ground state energy of the system is the minimum value of $E_e[n]$ with respect to n , and that the density that minimizes such a functional exactly corresponds to the ground state one, $n_0(\mathbf{r})$. Then the exact ground-state energy E_0 can be obtained from a variational (more precisely, a minimum) principle as

$$\left. \frac{\delta E_e^{HK}[n]}{\delta n(\mathbf{r})} \right|_{[n]=[n_0]} = 0, \quad (2.9)$$

$$E_0 = E_e^{HK}([n_0]),$$

along with the constraint that the integral of the particle density over the whole space corresponds to the total number of particles N ($\int d^3r n(\mathbf{r}) = N$).

The main advantage of the particle-density-representation for the electronic energy functional is that one has to deal with functionals of a field that is, in turn, function of a d -dimensional variable, instead of the Nd -dimensional original one. However, while the formalism presented so far is in principle an exact approach, its application is limited by the fact that the form of the functional F is unknown. A first step towards the applicability of the density functional theory was done by Kohn and Sham, as illustrated in the following section.

2.1.3 The Kohn-Sham auxiliary system

In their seminal work⁽³¹⁾, Kohn and Sham proposed to manipulate the Hohenberg-Kohn functional by considering the existence of an auxiliary independent-particles system whose (ground state) particle density is supposed to be equal to the one describing the interacting electrons system. From the independent-particles assumption, the particle density of the auxiliary system can be written as

$$n(\mathbf{r}) = \sum_i f_i |\varphi_i(\mathbf{r})|^2, \quad (2.10)$$

where $\{\varphi_i(\mathbf{r})\}_i$ are unknown single-particle states satisfying the orthonormalization conditions $\langle \varphi_i | \varphi_j \rangle = \delta_{ij}$, and $\{f_i\}_i$ a set of occupation numbers normalized to the total number of particle constituting the electronic system, $\sum_{i=1} f_i = N$. In order to reach a solvable scheme, Kohn and Sham rewrote the Hohenberg-Kohn functional, Eq.(2.8), into the following form

$$E_e^{HK}[n] = T_0[n] + E_H[n] + E_{xc}[n] + \int d^3r V_{ext}(\mathbf{r})n(\mathbf{r}), \quad (2.11)$$

where $T_0[n]$ is the independent particles-like kinetic functional, $E_H[n]$ is the Hartree energy corresponding to the non-local classical-kind Coulombic self-interaction of the electronic cloud,

$$E_H[n] = \frac{1}{2} \int d^3r d^3r' \frac{n(\mathbf{r})n(\mathbf{r}')}{|\mathbf{r} - \mathbf{r}'|}, \quad (2.12)$$

with $v(\mathbf{r}, \mathbf{r}') = \frac{1}{|\mathbf{r} - \mathbf{r}'|}$ the (non-local) Coulomb kernel, and $E_{xc}[n]$ is defined as

$$E_{xc}[n] = F[n] - T_0[n] - E_H[n], \quad (2.13)$$

and retains the exchange and correlation effects characterizing the interacting electronic system. Within the Kohn-Sham ansatz of independent-particles-like density, the constrained minimization with respect to $n(\mathbf{r})$ can be equivalently recast into a minimization with respect to the set of the single-particle states $\{\varphi_i(\mathbf{r})\}_i$ (see Eq. 2.10), with the constraint $\int d^3r n(\mathbf{r}) = N$ substituted by the orthonormalization requirement(s) $\langle \varphi_i | \varphi_j \rangle = \delta_{ij}$. The functional in the r.h.s. of Eq. (2.11) is suitable to such a purpose. Indeed, despite the n -representation of T_0 , $T_0[n]$, is unknown even in the simple case of non-interacting particles, its $\{\varphi_i\}_i$ -representation $T_0[\{\varphi_i\}_i]$ is well known. Then, constrained minimization with respect to the set of states $|\varphi_i\rangle$ leads to a system of N single-particle Shrödinger-like equations of the form

$$\hat{H}_{KS}|\varphi_i\rangle = \varepsilon_i|\varphi_i\rangle, \quad (2.14)$$

where H_{KS} is the Kohn-Sham Hamiltonian, defined through the Kohn-Sham *local* potential V_{KS} ; we shall refer to ε_i and $|\varphi_i\rangle$ as Kohn-Sham eigenvalues and eigenstates, respectively. In Atomic Units,

$$H_{KS} = -\frac{1}{2}\nabla^2 + V_{KS}(\mathbf{r}), \quad (2.15)$$

$$V_{KS}(\mathbf{r}) = V_{ext}(\mathbf{r}) + V_H(\mathbf{r}) + V_{xc}(\mathbf{r}), \quad (2.16)$$

with

$$V_H(\mathbf{r}) = \frac{\delta E_H[n]}{\delta n(\mathbf{r})} = \int d^3r' \frac{n(\mathbf{r}')}{|\mathbf{r} - \mathbf{r}'|}, \quad (2.17)$$

$$V_{xc}(\mathbf{r}) = \frac{\delta E_{xc}[n]}{\delta n(\mathbf{r})}, \quad (2.18)$$

Recall that in general the Kohn-Sham potential $V_{KS}(\mathbf{r})$ retains a parametric dependence on the spatial configuration of the ions.

Both the Hartree and XC potentials depend on the electronic particle density, that in turn depends on the set of the sought-after solutions $\{\varphi_i\}_i$ through Eq. (2.10). This means that, in order to obtain the ground-state particle density and the related physical properties of the electronic system, one has to find the *self-consistent* solutions of a system of N differential *coupled* equations.

2.1.4 The exchange and correlation functional

The scheme presented above allows one to solve the many-body problem once the XC potential is provided. Unfortunately, no exact form of the XC potential is known. However, many approximated forms have been proposed, with remarkable capability of reproducing the experimental data. Two of them have been especially popular

over the years; we discuss them in some detail in the following, as they are directly relevant to this thesis.

- The Local Density Approximation (LDA) builds on the assumption that the spatial variation of the density is slow. In such a regime, the exchange and correlation properties of the system must be well reproduced by those of the uniform electron gas, which are exact by construction in the uniform limit. In particular, the XC functional is written as

$$E_{\text{xc}}^{\text{LDA}}[n] = \int d^3r n(\mathbf{r}) \epsilon_{\text{xc}}^{\text{hom}}(n(\mathbf{r})), \quad (2.19)$$

with $\epsilon_{\text{xc}}^{\text{hom}}[n]$ being the exchange-correlation energy per electron of the homogeneous electron gas and n the electronic particle density describing the system. Even though LDA remains the most popular way of performing electronic-structure calculations based on DFT, its validity in describing solids with very inhomogeneous densities is not completely justified and needs to be verified by actual applications.

- The first step beyond LDA is the so called Generalized Gradient Approximation (GGA). It consists in considering an exchange-correlation functional that locally depends on both the density, n , and the density-gradient, ∇n ,

$$E_{\text{xc}}^{\text{GGA}}[n, |\nabla n|] = \int d^3r n(\mathbf{r}) \epsilon_{\text{xc}}^{\text{hom}}(n(\mathbf{r}), |\nabla n(\mathbf{r})|). \quad (2.20)$$

This allows, in principle, to improve the accuracy of the Kohn-Sham energy in situations where the density is far from uniform, which is the case of essentially all known condensed-matter systems. In practice, however, the improvement over LDA is far from systematic. There is an additional drawback, in that unlike the LDA there is no unique choice for the dependence of $E_{\text{xc}}^{\text{GGA}}$ on the local gradients of the density. Thus, many flavors of GGA exist in the literature, and their construction is usually targeted at a specific physical context (molecules, solids, etc.) where the performance is expected to be optimal.

2.2 Practical methods for ground-state calculations

In the following we shall specialize the formalism presented in the previous sections to the case of crystal systems.

2.2.1 Bloch theorem and Brillouin-zone integration

Let us consider an *infinitely extended crystal* system, composed of a ionic subsystem whose spatial configuration is described by a Bravais lattice,

$$\mathbf{R}_{l\kappa} = \mathbf{R}_l + \boldsymbol{\tau}_\kappa, \quad (2.21)$$

where $\mathbf{R}_l = \sum_i l_i \mathbf{a}_i$ and $\boldsymbol{\tau}_\kappa$ are 3-dimensional vectors referring to the position of the unit cell, identified by the set of integer numbers $l = (l_1, l_2, l_3)$, and the position of the sublattice κ within the former, respectively. \mathbf{a}_i are the primitive lattice vectors and correspond to the generators of the points constituting the lattice. As a consequence of the periodic spatial distribution of the ions, the Kohn-Sham potential,

$V_{\text{KS}}(\mathbf{r})$, turns out to be invariant under any translation vector \mathbf{R}_l and then, from the Bloch theorem, the Kohn-Sham eigenstates $|\varphi_i\rangle$ can be equivalently written as

$$\varphi_i(\mathbf{r}) = \varphi_{n\mathbf{k}}(\mathbf{r}) = e^{i\mathbf{k}\cdot\mathbf{r}} u_{n\mathbf{k}}(\mathbf{r}). \quad (2.22)$$

Where, \mathbf{k} is a so-called Bloch vector belonging to the *first Brillouin zone* of the reciprocal space that is spanned by the lattice vectors $\{\mathbf{b}_i\}_i$ such that

$$\mathbf{b}_i \cdot \mathbf{a}_j = 2\pi\delta_{ij}. \quad (2.23)$$

In turn, $u_{n,\mathbf{k}}(\mathbf{r})$ is the cell-periodic function of the n band at the point \mathbf{k} , and is solution of the following eigenvalue problem

$$\hat{H}_{\mathbf{k}}|u_{n\mathbf{k}}\rangle = \varepsilon_{n\mathbf{k}}|u_{n\mathbf{k}}\rangle, \quad \hat{H}_{\mathbf{k}} = e^{-i\mathbf{k}\cdot\hat{\mathbf{r}}} \hat{H} e^{i\mathbf{k}\cdot\hat{\mathbf{r}}}. \quad (2.24)$$

Therefore, any (Kohn-Sham) single-particle state describing an electron in a crystal is completely specified by the quantum numbers \mathbf{k} and n . From Eqs. (2.22) and (2.10), it also follows that the particle density is a cell-periodic function given by

$$n_0(\mathbf{r}) = s \int_{\text{BZ}} [d^3k] \sum_{n \in \mathcal{V}} |u_{n\mathbf{k}}(\mathbf{r})|^2, \quad (2.25)$$

where, an occupation factor, $s = 2$, for nonmagnetic systems has been assumed, the sum over n runs over the valence (\mathcal{V}) band manifold and we have introduced the following notation for the Brillouin zone averages

$$\int_{\text{BZ}} [d^3k] = \frac{\Omega}{(2\pi)^3} \int_{\text{BZ}} d^3k. \quad (2.26)$$

2.2.2 Plane-wave basis set

In the previous sections we have illustrated how the many-body problem can be solved within DFT by following the Kohn-Sham prescriptions, and specialize it to the specific case of a crystal. In particular the real-space representation of the resulting Kohn-Sham eigenvalue problem was provided. However, in a crystal, the Kohn-Sham equation is conveniently solved within a *reciprocal-space representation*. Indeed a Bloch-like state labelled by quantum numbers (n, \mathbf{k}) can be written as a combination of *plane waves* of the kind

$$u_{n,\mathbf{k}}(\mathbf{r}) = \sum_{\mathbf{G}} c_{n,\mathbf{k}+\mathbf{G}} e^{i\mathbf{G}\cdot\mathbf{r}}, \quad (2.27)$$

with $c_{n,\mathbf{k}+\mathbf{G}}$ the Fourier coefficients of $u_{n,\mathbf{k}}(\mathbf{r})$ and \mathbf{G} a vector belonging to the reciprocal lattice, consistent with the cell-periodicity of $u_{n\mathbf{k}}$. In practical implementations, the sum is truncated to those vectors whose kinetic energy is smaller than a chosen cutoff energy, E_{cutoff} ,

$$\frac{1}{2}|\mathbf{k} + \mathbf{G}|^2 < E_{\text{cutoff}}, \quad (2.28)$$

that is to those vectors that lie within the reciprocal-space sphere centered in \mathbf{k} ; E_{cutoff} is then treated as a convergence parameter.

The advantage of a plane-wave representation lies in that the kinetic operator becomes diagonal, and reads as (in atomic units)

$$T_{\mathbf{k}}(\mathbf{G}, \mathbf{G}') = \frac{|\mathbf{k} + \mathbf{G}|^2}{2} \delta_{\mathbf{G}, \mathbf{G}'}. \quad (2.29)$$

Another advantage lies in the efficient solution of the Poisson equation in reciprocal space, where the Fourier components of the Hartree potential are

$$V_{\mathbf{k}}^H(\mathbf{G}) = 4\pi \frac{n(\mathbf{G})}{|\mathbf{G}|^2}. \quad (2.30)$$

The external atomic potential requires some additional considerations; we shall go through them in the next Section.

2.2.3 Pseudopotentials

So far we have considered an all-electron picture, where the bare nuclei are represented by point charges. Dirac delta functions are highly impractical to represent on a plane-wave basis set, as they would require a prohibitively high value of E_{cutoff} in order to converge the results. Meanwhile, it is a well known fact that only the outer (valence) orbitals participate to chemical bonding, while the inner (core) electrons remain essentially inert. In other words, the latter are largely irrelevant to most physical properties one is interested in, and describing them explicitly in calculations of real materials is a waste.

The so-called *pseudopotentials* are aimed at addressing both issues at once. They consist in effectively replacing the atomic core (composed of the nucleus and the remaining core electrons) with a smooth ionic potential, which ideally reproduces the scattering properties of the former in a range of energy that is relevant to the valence electrons. In order to fulfill the latter requirement, however, the pseudopotential needs to be *non-local*, and constructed separately for each angular-momentum channel. Most implementations of DFT nowadays adopt a separable form due to Kleinman and Bylander. In particular, the pseudopotential (*psp*) of a given atom κ is written as a sum of a local (*loc*) and separable (*sep*) parts,

$$V_{\kappa}^{psp}(\mathbf{r}, \mathbf{r}') = V_{\kappa}^{loc}(\mathbf{r}) \delta^3(\mathbf{r} - \mathbf{r}') + V_{\kappa}^{sep}(\mathbf{r}, \mathbf{r}'). \quad (2.31)$$

where the latter is

$$V_{\kappa}^{sep}(\mathbf{r}, \mathbf{r}') = \sum_{\alpha} e_{\alpha\kappa} \zeta_{\alpha\kappa}(\mathbf{r} - \mathbf{R}_{\kappa}) \zeta_{\alpha\kappa}^*(\mathbf{r}' - \mathbf{R}_{\kappa}). \quad (2.32)$$

Here α runs on the angular momentum components, $\{l, m\}$, $\zeta_{\alpha\kappa}(\mathbf{r} - \mathbf{R}_{\kappa})$ the KB projectors, and $e_{\alpha\kappa}$ the related coefficients.

Within the context of plane-waves basis sets, the *hardness* of a pseudopotential is related with the amount of Fourier components it requires for its accurate representation. In the early days of the pseudopotentials developments, it was soon realized that the potentials required to accurately describe some ionic cores, such as the ones for transition metals, turned out to be extremely hard, i.e. they required too large basis sizes, for their use in practical calculations. Different sophistications have been proposed since then, such as the ultrasoft Vanderbilt pseudopotentials (33) or

the related projector-augmented-wave method (34), in order to improve the convergence problems and, hence, the computational efficiency. In this thesis, we shall employ norm-conserving pseudopotentials generated via the Hamann's approach (35) for their optimized trade-off between accuracy and computational efficiency, but also for their conceptual simplicity. In fact, the last factor becomes crucial to not overcomplicate the fundamental developments and computational implementations pursued in our works.

2.3 Density Functional Perturbation Theory (DFPT)

Let us consider a Hamiltonian depending on a (small) perturbative parameter λ , $\hat{H} = \hat{H}(\lambda)$. Then, the physical quantities of the system will depend on the parameter λ through the Kohn-Sham eigenvalue problem, Eq.(2.14), and their expansion in powers of λ can be calculated by applying the well-established rules of first-order perturbation theory. In particular, we shall write the energy, Hamiltonian and wave functions via a perturbative expansion around $\lambda = 0$ as

$$E(\lambda) = E^{(0)} + \lambda E^{(1)} + \lambda^2 E^{(2)} + \dots, \quad (2.33)$$

$$\hat{H}(\lambda) = \hat{H}^{(0)} + \lambda \hat{H}^{(1)} + \lambda^2 \hat{H}^{(2)} + \dots, \quad (2.34)$$

$$\varphi_i(\lambda) = \varphi_i^{(0)} + \lambda \varphi_i^{(1)} + \dots \quad (2.35)$$

The theoretical tools to perform the above expansions within DFT are broadly known as Density Functional Perturbation Theory (DFPT); we shall outline its basic principles in the following.

2.3.1 Sternheimer equation

By incorporating Eqs.(2.33),(2.34) and (2.35) into the Kohn-Sham equation, Eq.(2.14), while taking care of some subtleties that we shall discuss shortly, one finds that the first-order variation of the i -th state can be carried out by solving the so-called *Sternheimer equation*,

$$\left(\hat{H}^{(0)} - \alpha \hat{P} - \varepsilon_i^{(0)} \right) |\varphi_i^{(1)}\rangle = -\hat{Q} \hat{\mathcal{H}}^{(1)} |\varphi_i^{(0)}\rangle. \quad (2.36)$$

Here $\hat{P} = \sum_{i \in \mathcal{V}} |\varphi_i^{(0)}\rangle \langle \varphi_i^{(0)}|$ and $\hat{Q} = 1 - \hat{P}$ are the projector on the valence and conduction manifolds respectively (notice that the sum in the definition of \hat{P} runs over the occupied unperturbed states, $i \in \mathcal{V}$), and α is a positive constant that avoids the singularity of the l.h.s. of the above equation. In turn, $\hat{H}^{(0)}$ and $\varepsilon_i^{(0)}$ are, respectively, the ground-state KS hamiltonian and energies, whereas $\hat{\mathcal{H}}^{(1)}$ is the first-order variation of the KS Hamiltonian which includes the self-consistent fields contribution, as we shall show below.

The introduction of the band projectors, \hat{P} and \hat{Q} , on either side of Eq. (2.36) is not a direct consequence of Eq.(2.14), but reflects an additional constraint that we have implicitly imposed on the first-order wave functions. Indeed, the solutions of Eq. (2.36) are bound to be orthogonal to the valence manifold (\mathcal{V}),

$$\langle \varphi_i^{(0)} | \varphi_j^{(1)} \rangle = 0, \quad \forall i, j \in \mathcal{V}. \quad (2.37)$$

(It follows that the first-order response of any occupied state can be written as a linear combination of the unoccupied states $|\varphi_j^{(0)}\rangle$.) This condition is known as *parallel-transport gauge*, and is essential to guaranteeing that the solutions of Eq. (2.36) are unique. Indeed, the first-order expansion of the orthonormality constraint, $\langle \varphi_i(\lambda) | \varphi_j(\lambda) \rangle = \delta_{ij}$, alone leads to a less restrictive condition,

$$\langle \varphi_i^{(0)} | \varphi_j^{(1)} \rangle + \langle \varphi_i^{(1)} | \varphi_j^{(0)} \rangle = 0, \quad (2.38)$$

which leaves the valence components of the perturbed orbitals undefined. [This has to do with the gauge freedom in the choice of $|\varphi_j(\lambda)\rangle$ along the path.]

Note that in Eq. (2.36), the first-order Hamiltonian, $\hat{\mathcal{H}}^{(1)}$, depends on the first-order particle density, $n^{(1)}(\mathbf{r})$, via

$$\hat{\mathcal{H}}^{(1)} = \hat{H}^{(1)} + \int d^3r' K_{\text{Hxc}}(\mathbf{r}, \mathbf{r}') n^{(1)}(\mathbf{r}'), \quad (2.39)$$

where we have indicated with $\hat{H}^{(1)}$ the first-order variation of the *non* self-consistent part of the KS Hamiltonian and with $K_{\text{Hxc}}(\mathbf{r}, \mathbf{r}')$ the Hartree and exchange correlation (Hxc) kernel. The latter is defined as the variation of the self-consistent potential $V_{\text{Hxc}}(\mathbf{r})$, i.e. sum of Eqs. (2.17) and (2.18), due to a charge-density perturbation at \mathbf{r}' , $\delta n(\mathbf{r}')$, and calculated at the unperturbed density n_0 ,

$$K_{\text{Hxc}}(\mathbf{r}, \mathbf{r}') = \left. \frac{\delta V_{\text{Hxc}}(\mathbf{r})}{\delta n(\mathbf{r}')} \right|_{[n_0]} = \left. \frac{\partial E_{\text{Hxc}}[n]}{\partial n(\mathbf{r}) \delta n(\mathbf{r}')} \right|_{[n_0]}. \quad (2.40)$$

The first-order response of the density, in turn, is written as

$$n^{(1)}(\mathbf{r}) = s \sum_{i \in \mathcal{V}} \left(\varphi_i^{(0)*}(\mathbf{r}) \varphi_i^{(1)}(\mathbf{r}) + \varphi_i^{(1)*}(\mathbf{r}) \varphi_i^{(0)}(\mathbf{r}) \right), \quad (2.41)$$

where the sum runs, again, over the occupied states. Therefore, similarly to the unperturbed Kohn-Sham states, the solutions $|\varphi_i^{(1)}\rangle$ of the Sternheimer equation, Eq.(2.36), must be found in a self-consistent way.

2.3.2 Second-order energy and its variational formulation

The second-order variation of the electronic energy can be written as

$$E_e^{(2)} = \sum_{i \in \mathcal{V}} \langle \varphi_i^{(0)} | \hat{H}^{(1)} | \varphi_i^{(1)} \rangle + \sum_{i \in \mathcal{V}} \langle \varphi_i^{(1)} | \hat{H}^{(1)} | \varphi_i^{(0)} \rangle + \sum_{i \in \mathcal{V}} \langle \varphi_i^{(0)} | \hat{H}^{(2)} | \varphi_i^{(0)} \rangle. \quad (2.42)$$

Notice that the second derivatives of the wave functions are not needed. To see why, recall Hellmann-Feynman's theorem, which allows us to write the first derivative of the energy (e.g., the atomic forces) as

$$\frac{dE_e}{d\lambda} = \frac{\partial E_e}{\partial \lambda} = s \sum_{i \in \mathcal{V}} \langle \varphi_i^{(0)} | \hat{H}^{(1)} | \varphi_i^{(0)} \rangle. \quad (2.43)$$

Straight differentiation of Eq. (2.43) with respect to λ directly yields Eq. (2.42).

This is, in fact, a special case of a more general result, the so called $(2n+1)$ -theorem. The latter states that, to determine the response to a perturbation λ at order $(2n+1)$, the knowledge of the perturbed wavefunctions up to order n is sufficient;

moreover, the response at order $(2n)$ can be written as a variational functional of $|\varphi_i^{(n)}\rangle$. And indeed, by applying this result to the $n = 1$ case, Gonze (36; 37) showed that the second-order DFPT energy can be alternatively written as

$$\begin{aligned} E_e^{(2)} = & \sum_{i \in \mathcal{V}} \langle \varphi_i^{(1)} | (\hat{H}^{(0)} - \varepsilon_i^{(0)}) | \varphi_i^{(1)} \rangle \\ & + \sum_{i \in \mathcal{V}} \langle \varphi_i^{(0)} | \hat{H}^{(1)} | \varphi_i^{(1)} \rangle + \sum_{i \in \mathcal{V}} \langle \varphi_i^{(1)} | \hat{H}^{(1)} | \varphi_i^{(0)} \rangle \\ & + \frac{1}{2} \int_{\Omega} \int d^3r d^3r' K_{\text{Hxc}}(\mathbf{r}, \mathbf{r}') n^{(1)}(\mathbf{r}) n^{(1)}(\mathbf{r}') \\ & + \sum_{i \in \mathcal{V}} \langle \varphi_i^{(0)} | \hat{H}^{(2)} | \varphi_i^{(0)} \rangle. \end{aligned} \quad (2.44)$$

This formula, when used in combination with the orthogonality constraint Eq.(2.37), is *stationary* with respect to $|\varphi_i^{(1)}\rangle$. Indeed, by differentiating it with respect to $|\varphi_i^{(1)}\rangle$ the Sternheimer equation, Eq.(2.36), is recovered. If the latter is satisfied (i.e., at the variational minimum of $E_e^{(2)}$), Eq. (2.44) reduces then to Eq. (2.42). The present variational formulation will be key to the calculation of spatial dispersion via long-wave expansions, as we shall discuss later on.

We recall that, in general, the total second-order energy may also include a non self-consistent ionic contribution. We will come back to this point in the next section, when introducing the different type of perturbations.

2.3.3 Monochromatic perturbations and factorization of the phase

One of the main advantages of DFPT is the fact that it allows one to calculate the response to a spatially inhomogeneous perturbation, modulated at an arbitrary wave vector \mathbf{q} , by using the primitive unit cell of the crystal (38). Within the linear regime, such a “monochromatic” (referring to spatial frequencies) perturbation (λ) can be described as

$$\hat{H}^\lambda = e^{i\mathbf{q} \cdot \hat{\mathbf{r}}} \hat{H}_{\mathbf{q}}^\lambda, \quad (2.45)$$

where $H_{\mathbf{q}}^\lambda$ is a cell-periodic operator. Following Ref.(38), the Sternheimer equation then takes the following form,

$$\left(\hat{H}_{\mathbf{k}+\mathbf{q}}^{(0)} + \alpha \hat{P}_{\mathbf{k}+\mathbf{q}} - \varepsilon_{n\mathbf{k}}^{(0)} \right) |u_{n\mathbf{k},\mathbf{q}}^\lambda\rangle = -\hat{Q}_{\mathbf{k}+\mathbf{q}} \hat{H}_{\mathbf{k},\mathbf{q}}^\lambda |u_{n\mathbf{k}}^{(0)}\rangle. \quad (2.46)$$

Note that all quantities involved are cell-periodic: the \mathbf{q} -dependent complex phase has been conveniently reabsorbed by operating a shift of the band projectors ($\hat{P}_{\mathbf{k}+\mathbf{q}}$ and $\hat{Q}_{\mathbf{k}+\mathbf{q}}$) and ground-state Hamiltonian in momentum space. As a consequence, the first-order variation of the wave functions at \mathbf{k} now belongs to $\mathbf{k} + \mathbf{q}$,

$$|\varphi_{n\mathbf{k},\mathbf{q}}^\lambda\rangle = e^{i(\mathbf{k}+\mathbf{q}) \cdot \mathbf{r}} |u_{n\mathbf{k},\mathbf{q}}^\lambda\rangle. \quad (2.47)$$

Note that the first-order charge density can also be represented in the same form as Eq.(2.45),

$$n^\lambda(\mathbf{r}) = e^{i\mathbf{q} \cdot \mathbf{r}} n_{\mathbf{q}}^\lambda(\mathbf{r}), \quad (2.48)$$

where

$$n_{\mathbf{q}}^{\lambda}(\mathbf{r}) = s \int_{\text{BZ}} [d^3k] \sum_{n \in \mathcal{V}} \left(u_{n\mathbf{k}}^{(0)*}(\mathbf{r}) u_{n\mathbf{k},\mathbf{q}}^{\lambda}(\mathbf{r}) + u_{n\mathbf{k},\mathbf{q}}^{\lambda*}(\mathbf{r}) u_{n\mathbf{k}}^{(0)}(\mathbf{r}) \right), \quad (2.49)$$

is, again, a cell-periodic function. Similarly, by considering two monochromatic perturbations λ_1 and λ_2 , the nonstationary formula for the second derivative of the total energy reads as

$$E^{\lambda_1^* \lambda_2}(\mathbf{q}) = \int_{\text{BZ}} [d^3k] E_{\mathbf{k}}^{\lambda_1^* \lambda_2}(\mathbf{q}), \quad (2.50)$$

where the integrand has a similar form as Eq. (2.42)

$$\begin{aligned} E_{\mathbf{k}}^{\lambda_1^* \lambda_2}(\mathbf{q}) = & \sum_{n \in \mathcal{V}} \langle u_{n\mathbf{k},\mathbf{q}}^{\lambda_1} | \hat{H}_{\mathbf{k},\mathbf{q}}^{\lambda_2} | u_{n\mathbf{k}}^{(0)} \rangle + \sum_{n \in \mathcal{V}} \langle u_{n\mathbf{k}}^{(0)} | \left(\hat{H}_{\mathbf{k},\mathbf{q}}^{\lambda_1} \right)^{\dagger} | u_{n\mathbf{k},\mathbf{q}}^{\lambda_2} \rangle + \\ & \sum_{n \in \mathcal{V}} \langle u_{n\mathbf{k}}^{(0)} | \hat{H}_{\mathbf{k}}^{\lambda_1 \lambda_2}(\mathbf{q}) | u_{n\mathbf{k}}^{(0)} \rangle. \end{aligned} \quad (2.51)$$

Of course, also at finite \mathbf{q} , the second-order energy enjoys a stationary expression: we defer presenting it to the specific context of the analytic long-wave expansion (Sec. 2.5.3), where its importance will become most apparent.

2.4 Specific perturbations

The most common type of perturbations that are considered in DFPT are atomic displacements (phonons), electric fields, and strains. In the following we shall briefly describe the standard treatment of such a perturbations, as they are directly relevant to the calculation of the flexoelectric tensor.

2.4.1 Phonons

Phonon perturbations are defined (Gonze (37), and Gonze and Lee (39)) by a distortion of the lattice in the following form,

$$R_{\kappa\alpha}^l \longrightarrow R_{\kappa\alpha}^l + \lambda_{\kappa\alpha}^{\mathbf{q}} e^{i\mathbf{q} \cdot \mathbf{R}_l}, \quad (2.52)$$

with $\mathbf{R}_{\kappa}^l = \mathbf{R}_l + \boldsymbol{\tau}_{\kappa}$, where, as usual, \mathbf{R}_l refers to the position of the l -th unit cell and $\boldsymbol{\tau}_{\kappa}$ to the location of the κ sublattice within the latter. α refers to the Cartesian direction. The second derivatives of the total energy with respect to $\lambda_{\kappa\alpha}^{\mathbf{q}}$ define the force-constant matrix,

$$C_{\kappa\alpha,\kappa'\beta}^{\mathbf{q}} = \frac{\partial^2 E}{\partial \lambda_{\kappa\alpha}^{-\mathbf{q}} \partial \lambda_{\kappa'\beta}^{\mathbf{q}}} = E_e^{\lambda_{\kappa\alpha}^* \lambda_{\kappa'\beta}}(\mathbf{q}) + E_{\kappa\alpha,\kappa'\beta}^{\text{Ew}}(\mathbf{q}), \quad (2.53)$$

where $E_e^{\lambda_{\kappa\alpha}^* \lambda_{\kappa'\beta}}(\mathbf{q})$ is the electronic contribution and $E_{\kappa\alpha,\kappa'\beta}^{\text{Ew}}(\mathbf{q})$ is a nonvariational Ewald term that originates from the electrostatic ion-ion interactions. The electronic contributions to the second derivative can be readily calculated via Eqs. (2.50)-(2.51); the derivation of the the Ewald part is straightforward and can be found in the original references (39).

Physically, the force-constant matrix can be understood as the Fourier transform of the real-space interatomic force constants,

$$C_{\kappa\alpha,\kappa'\beta}^{\mathbf{q}} = \sum_l C_{\kappa\alpha,\kappa'\beta}^l e^{i\mathbf{q}\cdot\mathbf{R}_l}, \quad C_{\kappa\alpha,\kappa'\beta}^l = \frac{\partial^2 E}{\partial R_{\kappa\alpha}^0 \partial R_{\kappa'\beta}^l}. \quad (2.54)$$

Its knowledge allows for the calculation of the vibrational modes of the crystal across the full Brillouin zone by means of the following generalized eigenvalue problem,

$$\omega^2(\mathbf{q}) m_\kappa U_{\kappa\alpha}^{\mathbf{q}} = C_{\kappa\alpha,\kappa'\beta}^{\mathbf{q}} U_{\kappa'\beta}^{\mathbf{q}}. \quad (2.55)$$

The above equation corresponds to the equation of motion for the ions in the crystal. $U_\kappa^{\mathbf{q}}$ is the periodic part of the vibrational mode, $\omega(\mathbf{q})$ its frequency, and m_κ the mass of the κ -sublattice.

Note that one is free to choose the origin of the complex phase factor in Eq.(2.52) independently for each sublattice. This choice won't change the calculated physical properties (e.g. the calculated phonon frequencies), it is instead a matter of convenience. Eq.(2.52) reflects the standard conventions of the DFPT literature, whose motivation lies in the particularly simple form of the Fourier transform (Eq.(2.54)) it leads to. In the remainder of this work we will adopt a different choice, which is incomparably more convenient when studying the long-wavelength limit (22),

$$R_{\kappa\alpha}^l \longrightarrow R_{\kappa\alpha}^l + \lambda_{\kappa\alpha} e^{i\mathbf{q}\cdot(\mathbf{R}_l + \boldsymbol{\tau}_\kappa)}. \quad (2.56)$$

Our choice is motivated by the fact that Eq.(2.56) assigns a common origin to the phase factor $e^{i\mathbf{q}\cdot\mathbf{r}}$ "seen" by all sublattices, which is essential for a long-wave analysis to be physically meaningful. (22) This results in a trivial redefinition of the response functions, e.g.,

$$\Phi_{\kappa\alpha,\kappa'\beta}^{\mathbf{q}} = C_{\kappa\alpha,\kappa'\beta}^{\mathbf{q}} e^{i\mathbf{q}\cdot(\boldsymbol{\tau}_{\kappa'} - \boldsymbol{\tau}_\kappa)}. \quad (2.57)$$

2.4.2 Electric field perturbation

The linear response to a uniform electric field entails an additional complication, in that the corresponding external potential acting on the electrons, $V(\mathbf{r}) = \mathbf{E} \cdot \mathbf{r}$, grows linearly as a function of position, and hence breaks translational invariance. This problem has been traditionally overcome (37) by considering, instead, the long-wave limit of a scalar potential perturbation modulated in space at a small wave-vector \mathbf{q} ,

$$\hat{H}_{\mathbf{q}}^\phi(\mathbf{r}) = \phi e^{i\mathbf{q}\cdot\mathbf{r}}. \quad (2.58)$$

One recovers a formulation of the electric-field perturbation that fits nicely in the DFPT formalism that we outlined earlier, with a (nonlocal and \mathbf{k} -dependent) first-order Hamiltonian acting on the Bloch states as

$$\hat{H}_{\mathbf{k}}^{E_\alpha} |u_{n\mathbf{k}}^{(0)}\rangle = |iu_{n\mathbf{k}}^{k_\alpha}\rangle, \quad |iu_{n\mathbf{k}}^{k_\alpha}\rangle = i\hat{Q}_{\mathbf{k}} \frac{\partial |u_{n\mathbf{k}}^{(0)}\rangle}{\partial k_\alpha}. \quad (2.59)$$

Note that the formalism requires the calculation of an auxiliary quantity: the derivative of the ground-state wave functions with respect to their wave vector (often indicated as " d/dk " wave functions). In practice, the latter can be obtained via a non-selfconsistent DFPT calculation where the role of the first-order Hamiltonian in the Sternheimer equation is played by the velocity operator,

$$\hat{H}_{\mathbf{k}}^{k_\alpha} = \frac{\partial \hat{H}_{\mathbf{k}}^{(0)}}{\partial k_\alpha}. \quad (2.60)$$

Note that the velocity operator coincides with the “uniform electromagnetic vector potential” perturbation and, indeed, the same conclusions can be reached by working in the velocity gauge and taking an adiabatic expansion in powers of the frequency. (27)

In combination with the phonon perturbation described earlier, the strategy outlined here enables the calculation in periodic boundary conditions of important physical properties of insulating crystals, such as the dielectric susceptibility or the Born effective charges (39).

2.4.3 Uniform strain perturbation

The main difficulty in treating a homogeneous deformation within DFPT consists in that, upon a change in the lattice parameters, the Hilbert space describing the electronic system changes. In other words, the wave functions of the deformed configuration cannot be represented on the same plane-wave basis describing the unperturbed states, contrary to the cases (phonon or uniform electric field) considered so far.

Hamann *et al.* (40) overcame the problem by employing a *reduced coordinates* formulation. The idea consists in expressing the real- and reciprocal-space vectors as

$$\mathbf{r} = \sum_i \mathbf{a}_i \tilde{r}_i, \quad \mathbf{G} = \sum_i \mathbf{b}_i \tilde{G}_i, \quad (2.61)$$

where \mathbf{a}_i and \mathbf{b}_i are the primitive lattice vectors and their duals (see Section 2.2.1). Crucially, the reduced-coordinate representations of both \mathbf{r} and \mathbf{G} (tilded quantities) does not depend on the shape or dimensions of the cell. This means that, the plane-wave basis set becomes cell-independent in reduced coordinates,

$$e^{i\mathbf{G} \cdot \mathbf{r}} = e^{2\pi i \tilde{\mathbf{G}} \cdot \tilde{\mathbf{r}}}, \quad (2.62)$$

i.e., neither the Hilbert space nor the boundary conditions on $\tilde{\mathbf{G}}$ and $\tilde{\mathbf{r}}$ depend on the cell parameters any longer. Thanks to this observation, the uniform strain perturbation can be then recast as a parametric derivative of the reduced-coordinate Hamiltonian, and treated within the standard framework of DFPT.

It is interesting to observe that all terms in the total energy depend on \mathbf{r} and \mathbf{G} only via their scalar products. Thus, the real- and reciprocal-space vectors enter the energy functional only indirectly via the *metric tensor*,

$$\Xi_{ij} = \mathbf{a}_i \cdot \mathbf{a}_j, \quad (2.63)$$

and its inverse. Then, the first-order Hamiltonian of the uniform strain perturbation can be written as

$$\hat{H}_{\mathbf{k}}^{\eta_{\alpha\beta}} = \frac{\partial \hat{H}_{\mathbf{k}}}{\partial \Xi_{ij}} (a_{i\alpha} a_{j\beta} + a_{j\alpha} a_{i\beta}), \quad (2.64)$$

with $a_{i\alpha}$ the α Cartesian component of the unperturbed lattice vector \mathbf{a}_i and $\eta_{\alpha\beta}$ indicating the uniform strain tensor. Note that, at difference with other perturbations, the parametric derivative in Ξ_{ij} yields contributions from essentially all terms in the

Hamiltonian, including the kinetic energy operator. Otherwise, the strain perturbation is treated in the exact same way as (zone-center) phonons and electric fields. In combination with the latter, it completes the toolkit of standard DFPT with a whole new set of important properties, including elasticity and piezoelectricity.

This is the first time that we introduce the metric tensor in this thesis, and it won't be the last. The relevance of a reduced-coordinates representation in treating macroscopic deformations will become even clearer later on, when we move to the more challenging inhomogeneous case.

2.5 Long-wave DFPT

Spatial dispersion refers to the dependence of a material property on the wave vector \mathbf{q} at which it is probed, or equivalently, on the real-space gradients of the applied field. Capturing these effects goes beyond the scopes of the “traditional” DFPT techniques that we have presented so far, which ruled out the calculation of flexoelectricity until about ten years ago. In this Section, we shall review the recent developments that lifted this limitation and made such calculations possible.

The main idea revolves around incorporating the long-wavelength method into modern DFPT (hence the name “long-wave DFPT”), and making it work for the study of flexoelectricity. To that end, several challenges had to be addressed: on one hand, both the strain and electric field perturbation had to be generalized to the inhomogeneous (finite- \mathbf{q}) case; on the other hand, techniques to deal with the parametric expansion in the wave vector had to be developed.

2.5.1 Treatment of inhomogeneous strain

To make strain gradients tractable in the framework of DFPT, the strategy is similar as what was done many years ago for E-fields: the first goal consists in recasting the perturbation in a modulated form. This task can be carried out as follows. First, observe that an arbitrary strain pattern can be written as a 3D–3D mapping from a reference to a deformed configuration,

$$\mathbf{r}'(\mathbf{r}, t) = \mathbf{r} + \mathbf{u}(\mathbf{r}, t) \quad (2.65)$$

where \mathbf{u} is the deformation field. Now, the individual Fourier components of $\mathbf{u}(\mathbf{r})$ can be conveniently regarded as monochromatic *acoustic phonon* perturbations. In particular, by exploiting linearity, the corresponding first-order Hamiltonian can be written as sublattice sum of the individual phonon perturbations of Sec. 2.4.1,

$$\hat{H}_{\mathbf{k}, \mathbf{q}}^{u_\beta} = \sum_{\kappa} \hat{H}_{\mathbf{k}, \mathbf{q}}^{\lambda_{\kappa\beta}} \quad (2.66)$$

By studying the response to u_β at various \mathbf{q} vectors one could, in principle, access the physical consequences of an arbitrary deformation field, and hence determine the flexoelectric properties of the material.

For reasons that will become clearer shortly, however, it is extremely convenient to operate a simultaneous (i.e., in parallel with the aforementioned acoustic phonon perturbation) coordinate transformation to the curvilinear co-moving frame, where the atoms do not move at all, Fig. (2.1).

This procedure allows to write the first-order Hamiltonian as

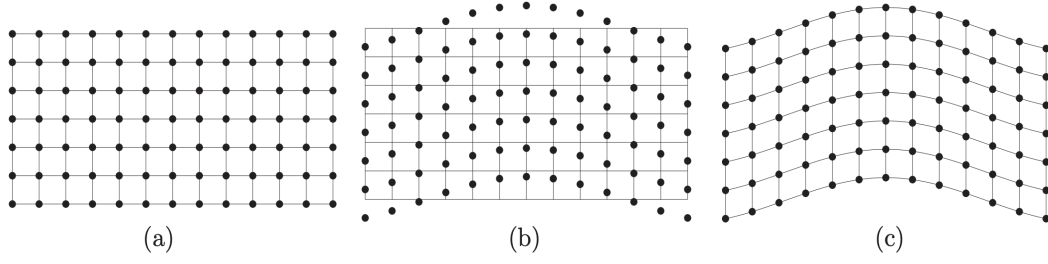


FIGURE 2.1: Illustration of the coordinate transformation to the co-moving frame. (a) Unperturbed crystal lattice; black circles represent the atomic sites, horizontal and vertical lines represent the coordinate system. (b) Transverse acoustic phonon in the laboratory frame. (c) The same phonon in the curvilinear frame; note that the atoms do not move in this coordinate system: the mechanical deformation is described via the metric.

$$\hat{\mathcal{H}}_{\mathbf{k},\mathbf{q}}^{u_\beta} = \hat{\mathcal{H}}_{\mathbf{k},\mathbf{q}}^{(\beta)} + i\hat{H}_{\mathbf{k}+\mathbf{q}}^{(0)} \left(\hat{p}_{\mathbf{k}\beta} + \frac{q_\beta}{2} \right) - i \left(\hat{p}_{\mathbf{k}\beta} + \frac{q_\beta}{2} \right) \hat{H}_{\mathbf{k}}^{(0)}, \quad (2.67)$$

where $\hat{p}_{\mathbf{k}\beta} = -i\hat{\nabla}_\beta + k_\beta$ is the canonical momentum operator and $\mathcal{H}^{(\beta)}$ is the so-called *metric-wave* Hamiltonian of Schiaffino et al. (25). The latter embodies the main physical effects of the deformation, including the self-consistent fields. The remainder has to do with the effective vector potential field (41) felt by the electron when evolving along the distortion path; we won't deal with it further here. (The interested reader can find an extensive discussion of its physical significance in Ref.(41))

The metric-wave formulation of the inhomogeneous strain problem has two key advantages: (i) $H^{(\beta)}$ vanishes at $\mathbf{q} = 0$, and (ii) it reduces to Hamann's uniform strain Hamiltonian at first order in \mathbf{q} ,

$$\hat{H}_{\mathbf{k},\mathbf{q}}^{(\beta)} \simeq iq_\gamma \hat{H}_{\mathbf{k}}^{\eta_{\beta\gamma}} + \mathcal{O}(q^2). \quad (2.68)$$

Thus, the metric-wave approach can be regarded as the sought-after generalization of the uniform strain perturbation of Hamann *et al.* (40) to the case of inhomogeneous deformations.

2.5.2 Treatment of inhomogeneous polarization from current-density

In addition to a finite- \mathbf{q} theory of strain, we also need a finite- \mathbf{q} (i.e., inhomogeneous) definition of the polarization response. The induced microscopic polarization response to an adiabatic transformation of the crystal can be defined as the current density divided by the rate of the transformation. In the limit of slow velocities we have, for an arbitrary perturbation λ modulated in space and time,

$$\frac{\partial P_\alpha(\mathbf{r})}{\partial \lambda_{\kappa\beta}^{\mathbf{q}}} = \frac{\partial j_\alpha(\mathbf{r})}{\partial \dot{\lambda}_{\kappa\beta}^{\mathbf{q}}}. \quad (2.69)$$

So the problem of defining the microscopic polarization response is that of appropriately defining the transient current density field in a DFT context. Naively, one

would be tempted to use the textbook expression for the probability current, which in absence of electromagnetic fields reads as (42)

$$\hat{j}_\alpha^{loc}(\mathbf{r}) = -\frac{\hat{p}_\alpha|\mathbf{r}\rangle\langle\mathbf{r}| + |\mathbf{r}\rangle\langle\mathbf{r}|\hat{p}_\alpha}{2}. \quad (2.70)$$

In reciprocal space, this leads to (24)

$$\hat{j}_{\alpha,\mathbf{k},\mathbf{q}}^{loc} = -\left(\hat{p}_{\mathbf{k}\alpha} + \frac{q_\alpha}{2}\right). \quad (2.71)$$

However, if a *non local* potential is present, as it is the case in the vast majority of first-principles calculations performed nowadays (see Sec. 2.2.3), the above definition is no longer valid, and an extra term must be added, (24)

$$\hat{j}_{\alpha\mathbf{k},\mathbf{q}} = \hat{j}_{\alpha\mathbf{k},\mathbf{q}}^{loc} + \hat{j}_{\alpha\mathbf{k},\mathbf{q}}^{NL}. \quad (2.72)$$

The nonlocal correction, \hat{j}^{NL} , must be chosen in such a way that the total current satisfies the following two basic criteria,

$$\nabla \cdot \mathbf{j} = -\dot{\rho} \quad \hat{j}_{\alpha\mathbf{k},\mathbf{q}=0} = -\frac{\partial \hat{H}_{\mathbf{k}}}{\partial k_\alpha}, \quad (2.73)$$

stating that: (i) \mathbf{j} is related to the variations of the charge density ρ in time by an exact conservation law (charge continuity), and (ii) at $\mathbf{q} = 0$ it reduces to (minus) the macroscopic velocity operator.

Both (i–ii) are automatically satisfied by defining the current-density operator as *minus* the derivative of the Hamiltonian with respect to a modulated vector potential field,

$$\hat{j}_{\alpha\mathbf{k},\mathbf{q}} = -\frac{\partial \hat{H}_{\mathbf{k}}}{\partial A_\alpha^{\mathbf{q}}}, \quad (2.74)$$

provided that \mathbf{A} enters the Hamiltonian in a way that respects electromagnetic gauge invariance. (Recipes to do so are discussed in Ref.(24).) Then, the cell average of the polarization response to a spatially inhomogeneous perturbation λ can be written as

$$\bar{P}_{\beta,\lambda}^{\mathbf{q}} = \int [d^3k] \sum_n \langle u_{n\mathbf{k},\mathbf{q}}^{A_\beta} | u_{n\mathbf{k},\mathbf{q}}^\lambda \rangle, \quad (2.75)$$

where we have introduced the first-order wave function response to a modulated vector potential field, $\mathbf{A}(\mathbf{r}) = \mathbf{A}^{\mathbf{q}}(\mathbf{r})e^{i\mathbf{q}\cdot\mathbf{r}}$, as the non-SCF solution of the Sternheimer equation, Eq.(2.36), with the external potential set to $\hat{H}_{\mathbf{k},\mathbf{q}}^{A_\alpha} = \frac{\partial \hat{H}_{\mathbf{k}}}{\partial A_\alpha^{\mathbf{q}}}$.

2.5.3 Spatial dispersion from analytical \mathbf{q} -expansion

The methods outlined in Sections 2.5.1 and 2.5.2 enable, in principle, the calculation of the polarization response (24) to an acoustic phonon at finite \mathbf{q} . Based on such information, one could access all components of the bulk flexoelectric tensor by performing a numerical differentiation in \mathbf{q} . While viable (a practical demonstration can be found in Ref.(25)), this strategy is far from optimal, for two main reasons. First, the necessity of repeating the calculation at several values of \mathbf{q} introduces a significant computational overhead. Second, the discrete sampling of the small- \mathbf{q} region is a potential source of numerical inaccuracies related to the fit. To correct these drawbacks, Royo and Stengel (27) developed a general method that allows to

take the derivatives in \mathbf{q} of an arbitrary response property analytically. The method is general and can then be used to calculate arbitrary spatial dispersion effects at negligible cost, even beyond the specifics of flexoelectricity; we shall review it in the following.

Consider two perturbations, λ_1 and λ_2 , which are modulated at a given wave vector \mathbf{q} . Based on the standard rules of DFPT (see Sec.2.3.3), the second-derivative of the electronic energy with respect to $\lambda_{1,2}$ can be written as a stationary functional of the first-order wave functions; the functional ought to be minimized in combination with the orthonormality constraints, Eq. (2.37). The first important result of Ref. (27) consists in reformulating the second-order energy in an *unconstrained* variational form,

$$\begin{aligned} E^{\lambda_1^* \lambda_2}(\mathbf{q}) = & \int_{\text{BZ}} [d^3k] \sum_m \langle u_{m\mathbf{k},\mathbf{q}}^{\lambda_1} | \left(\hat{H}_{\mathbf{k}+\mathbf{q}}^{(0)} + a\hat{P}_{\mathbf{k}+\mathbf{q}} - \varepsilon_{m\mathbf{k}} \right) | u_{m\mathbf{k},\mathbf{q}}^{\lambda_2} \rangle \\ & + \int_{\text{BZ}} [d^3k] \sum_m \langle u_{m\mathbf{k},\mathbf{q}}^{\lambda_1} | \hat{Q}_{\mathbf{k}+\mathbf{q}} \hat{H}_{\mathbf{k},\mathbf{q}}^{\lambda_2} | u_{m\mathbf{k}}^{(0)} \rangle \\ & + \int_{\text{BZ}} [d^3k] \sum_m \langle u_{m\mathbf{k}}^{(0)} | \left(\hat{H}_{\mathbf{k},\mathbf{q}}^{\lambda_1} \right)^\dagger \hat{Q}_{\mathbf{k}+\mathbf{q}} | u_{m\mathbf{k},\mathbf{q}}^{\lambda_2} \rangle \\ & + \frac{1}{2} \int_{\Omega} \int K_{\mathbf{q}}(\mathbf{r}, \mathbf{r}') \left(n_{\mathbf{q}}^{\lambda_1}(\mathbf{r}) \right)^* n_{\mathbf{q}}^{\lambda_2}(\mathbf{r}') d^3r d^3r' \\ & + E_{\text{nv}}^{\lambda_1^* \lambda_2}(\mathbf{q}). \end{aligned} \quad (2.76)$$

Here, as usual, \hat{H}^λ refers to the non self-consistent part of the first-order Hamiltonian. The first-order densities are defined, similarly to Eq.(2.49) while implicitly assuming time-reversal symmetry, as

$$n_{\mathbf{q}}^\lambda(\mathbf{r}) = 2s \int [d^3k] \sum_m \langle u_{m\mathbf{k}}^{(0)} | \mathbf{r} \rangle \langle \mathbf{r} | \hat{Q}_{\mathbf{k}+\mathbf{q}} | u_{m\mathbf{k},\mathbf{q}}^\lambda \rangle, \quad (2.77)$$

$K_{\mathbf{q}}(\mathbf{r}, \mathbf{r}') = K_{\text{Hxc}}(\mathbf{r}, \mathbf{r}') e^{i\mathbf{q} \cdot (\mathbf{r} - \mathbf{r}')}$ is the phase-corrected Coulomb and exchange-correlation kernel (27), and $E_{\text{nv}}^{\lambda_1^* \lambda_2}(\mathbf{q})$ stands for all nonvariational contributions that do not depend on the $|u_{m\mathbf{k},\mathbf{q}}^\lambda\rangle$'s. The main difference with respect to the established formulas (39) consists in the insertion of the band projectors \hat{P} and \hat{Q} in a few strategic places; their purpose is to guarantee that the variational solutions *automatically* comply with the parallel-transport gauge prescription, without the need for explicitly enforcing the constraints.

This key result enables treating \mathbf{q} as a standard perturbation parameter, and thereby applying the standard rules of DFPT to perform the analytic long-wavelength expansion of $E^{\lambda_1^* \lambda_2}(\mathbf{q})$. In particular, by using the well established $(2n+1)$ -theorem (see Sec.2.3.2), one can write

$$E_{\gamma}^{\lambda_1^* \lambda_2} = \left. \frac{dE^{\lambda_1^* \lambda_2}(\mathbf{q})}{dq_{\gamma}} \right|_{\mathbf{q}=0} = \left. \frac{\partial E^{\lambda_1^* \lambda_2}(\mathbf{q})}{\partial q_{\gamma}} \right|_{\mathbf{q}=0}, \quad (2.78)$$

where (in close analogy with the Hellmann-Feynman theorem, Eq.(2.43)) the partial derivative indicates that the first-order wave functions need not be differentiated in \mathbf{q} . In other words, spatial dispersion coefficients can be calculated with *the uniform* ($\mathbf{q} = 0$) *wave-function response*, $|u_{m\mathbf{k}}^{\lambda_{1,2}}\rangle$, *as the only input*. Apart from the application to flexoelectricity, which we shall discuss more extensively in the next Chapter, note

that this strategy was also applied successfully in other contexts, e.g., dynamical quadrupoles (27), natural optical activity (43) and rotational g-factors of molecules (44).

Before closing, a few important remarks are in order in relation to the analytical long-wave expansion of $E^{\lambda_1^* \lambda_2}(\mathbf{q})$ (further details can be found in Ref. (27)):

- The differentiation of the band projectors $\hat{Q}_{\mathbf{k}+\mathbf{q}}$ yields the “ d/dk ” wave functions, which we have already encountered earlier (Sec.2.4.2). These auxiliary quantities always need to be computed in the context of spatial dispersion, even if neither λ_1 nor λ_2 is an electric field.
- If either λ_1 or λ_2 (or both) is an electric field, also second derivatives in \mathbf{k} (and possibly the wavefunction response to an orbital magnetic field) need to be computed, as they appear when differentiating in \mathbf{q} the modulated \mathbf{A} -field wave functions of Eq. (2.76).
- A crucial prerequisite for the long-wavelength expansion outlined above is that $E^{\lambda_1^* \lambda_2}(\mathbf{q})$ must be an analytic (i.e., continuous and differentiable) function of \mathbf{q} . This is hardly the case in insulators, where the screened Coulomb kernel diverges at $\mathbf{q} = 0$: this implies a nonanalytic behavior of $E^{\lambda_1^* \lambda_2}(\mathbf{q})$ therein. Prior to differentiating in \mathbf{q} one must suppress these macroscopic electric fields somehow, and the way to do so is nonunique. This implies that spatial dispersion coefficients in general are affected by a certain degree of arbitrariness, which can be regarded as a *reference potential ambiguity*. (28) We shall come back to this important point in Sec.3.2.3.

Chapter 3

First-principles theory of flexoelectricity

In this chapter, we will present the state of the art regarding the first-principles theory of flexoelectricity at the moment when this doctoral project began.

From a purely theoretical point of view flexoelectricity remained poorly understood until the seminal work of Tagantsev (45), developed by building on the reference work of Born and Huang (46). Tagantsev described the flexoelectric effect by using of a point-charge model within a microscopic classical theory. Such a method has been the basis for more recent developements of the theory of flexoelectricity. A further step towards a full understanding of flexoelectricity from a first-principles point of view and within an exact microscopic framework was done by Resta (47) who, inspired by Martin's milestone work on the theory of piezoelectricity (48), based his analysis on the response of the charge density to atomic displacements in elemental crystals at the clamped-ion level. This idea was then generalized by Hong and Vanderbilt (49) to generic insulating crystals and employed to calculate some components of the flexoelectric tensor of several materials within the framework of DFT.

However, it was soon realized that the microscopic charge density response was not enough, at the bulk level, to obtain the whole flexoelectric response. Indeed the induced microscopic charge density is defined as the divergence of the induced microscopic polarization field, and only the longitudinal component of the latter can be accessed from the former. In addition, only bulk 3D crystals were considered in the mentioned works and no information about the surface effects in real finite samples was provided.

A way to solve both issues was proposed by Stengel (22; 23; 26). In his work, the author proposed a first-principles quantum theory based on the long-wave analysis of the adiabatic quantum current density induced by a long-wavelength acoustic phonon. Such a method is capable to provide, by construction, the all-components flexoelectric tensor. Remarkably, the latter can be fully calculated by performing a Taylor expansion in \mathbf{q} (around Γ) of cell-periodic response functions that can be implemented in standard DFPT (22). Moreover, by mixing this method with a co-variant formulation of the electrostatic quantities in the coordinate system of the deformed sample, one can also describe the behaviour of a finite sample and obtain a fundamental picture to characterize the surface contributions participating in the flexoelectric response of e.g. a finite slab (23). It was numerically proved that, even in the limit of large thickness, the sign of the flexoelectric response induced by a bending can be even reversed depending on how the slab is terminated (26), thus illustrating the pivotal role of the surfaces on the flexoelectric response, as was later on experimentally corroborated. (50)

In the following, after providing the basic definitions of strain and strain-gradient and the related definitions of piezoelectric and flexoelectric coefficients, we illustrate

the first-principle method that constituted the ground to build the formalism we used to define and calculate the flexoelectric response of a quasi-2D material.

3.1 General definitions: deformations, strain and strain gradients

The deformed configuration \mathbf{r}' of the material points within a generic (continuum) medium, whose unperturbed configuration is identified by the reference state \mathbf{r} , can be written as

$$\mathbf{r}'(\mathbf{r}, t) = \mathbf{r} + \mathbf{u}(\mathbf{r}, t), \quad (3.1)$$

where $\mathbf{u}(\mathbf{r}, t)$ is the so called deformation field. The latter is a function of the reference configuration \mathbf{r} and it can possibly depend parametrically on time. From 3.1 one can define, in full generality, a *deformation gradient* (strain) field as

$$u_{\alpha,\beta}(\mathbf{r}) = \frac{\partial u_{\alpha}(\mathbf{r})}{\partial r_{\beta}}. \quad (3.2)$$

Greek letters here label Cartesian components (henceforth we shall omit the time-dependence, as it does not affect the following definitions). The deformation gradient can be recast into the sum of a symmetric and an antisymmetric parts. Its symmetric part is defined as

$$\varepsilon_{\alpha\beta}(\mathbf{r}) = \frac{1}{2} (u_{\alpha,\beta}(\mathbf{r}) + u_{\beta,\alpha}(\mathbf{r})). \quad (3.3)$$

Similarly to the deformation gradient, we can then define a strain-gradient field. Based on the definitions provided above, two types of *strain-gradient* fields can be defined. One is the gradient of the unsymmetrized (type-I) strain (Eq.(3.2))

$$u_{\alpha,\beta\gamma}(\mathbf{r}) = \frac{\partial u_{\alpha,\beta}(\mathbf{r})}{\partial r_{\gamma}} = \frac{\partial^2 u_{\alpha}(\mathbf{r})}{\partial r_{\beta} \partial r_{\gamma}}, \quad (3.4)$$

and manifestly invariant under $\beta \longleftrightarrow \gamma$ exchange. The second one is defined as the gradient of the symmetrized (type-II) strain defined in Eq.(3.3)

$$\varepsilon_{\alpha\beta,\gamma}(\mathbf{r}) = \frac{\partial \varepsilon_{\alpha\beta}(\mathbf{r})}{\partial r_{\gamma}} = \frac{1}{2} \left(\frac{\partial^2 u_{\alpha}(\mathbf{r})}{\partial r_{\beta} \partial r_{\gamma}} + \frac{\partial^2 u_{\beta}(\mathbf{r})}{\partial r_{\alpha} \partial r_{\gamma}} \right), \quad (3.5)$$

and symmetric under exchange of labels $\alpha \longleftrightarrow \beta$. Both type-I and type-II strain-gradients have the same number of independent entries; their converse relationship is

$$u_{\alpha,\beta\gamma}(\mathbf{r}) = \varepsilon_{\alpha\beta,\gamma}(\mathbf{r}) + \varepsilon_{\gamma\alpha,\beta}(\mathbf{r}) - \varepsilon_{\beta\gamma,\alpha}(\mathbf{r}). \quad (3.6)$$

3.2 Macroscopic flexoelectric coefficients in 3D crystals

The generation of polarization in response to a uniform strain is referred as piezoelectricity, and the so called *piezoelectric coefficients* are then defined as

$$e_{\alpha,\beta\gamma} = \frac{\partial P_{\alpha}}{\partial \varepsilon_{\beta\gamma}}, \quad (3.7)$$

where the third-rank nature of the piezoelectric tensor requires a broken spatial inversion symmetry to be different from zero. Flexoelectricity, instead, describes the generation of macroscopic polarization (or voltage difference) within a material due to the application of a uniform strain-gradient. Based on the definition of the two types of strain-gradient provided in the previous section, we can define two different sets of *flexoelectric coefficients*,

$$\mu_{\alpha\beta,\gamma\lambda}^{\text{I}} = \frac{\partial P_{\alpha}}{\partial u_{\beta,\gamma\lambda}}, \quad (3.8)$$

$$\mu_{\alpha\lambda,\beta\gamma}^{\text{II}} = \frac{\partial P_{\alpha}}{\partial \varepsilon_{\beta\gamma,\lambda}}. \quad (3.9)$$

They obviously retain the symmetries of the strain-gradients they are related with and they are therefore both symmetric under exchange of the third and fourth labels. From the fact that type-I and type-II strain-gradients have the same number of independent entries, it follows that $\mu_{\alpha\beta,\gamma\lambda}^{\text{I}}$ and $\mu_{\alpha\lambda,\beta\gamma}^{\text{II}}$ have the same number of independent entries as well and, through expressions (3.5) and (3.6), one finds that they are related to each other as

$$\mu_{\alpha\lambda,\beta\gamma}^{\text{II}} = \mu_{\alpha\beta,\gamma\lambda}^{\text{I}} + \mu_{\alpha\gamma,\lambda\beta}^{\text{I}} - \mu_{\alpha\lambda,\beta\gamma}^{\text{I}}, \quad (3.10)$$

$$\mu_{\alpha\beta,\gamma\lambda}^{\text{I}} = \frac{1}{2} \left(\mu_{\alpha\lambda,\beta\gamma}^{\text{II}} + \mu_{\alpha\beta,\lambda\gamma}^{\text{II}} \right). \quad (3.11)$$

The fact that the flexoelectric tensor is fourth rank ensures the existence of, at least, one linearly-independent component. This is why flexoelectricity, in contrast to piezoelectricity, is a universal property of all materials, no matter their internal symmetries.

3.2.1 Bulk flexoelectric tensor from long-wave acoustic phonons

The main difficulty that one has to face when treating a strain gradient from a first-principles perspective, is the fact that the application of the latter generally breaks the translation symmetry of the unperturbed crystal, preventing the use of the standard methods developed in DFT. However, this problem can be overcome by considering a monochromatic long-wavelength acoustic phonon whose spatial modulation is described by a wave vector \mathbf{q} . Indeed, while such a perturbation can be generally incommensurate with the lattice of the unperturbed crystal, the first-order variation of the physical quantities in response to such a perturbation can be calculated by using cell-periodic functions (22), as illustrated in section 2.3. The interesting fact is that the atomic displacements induced by such an acoustic mode in the long-wave limit reproduce, at the first and second orders in the wave vector, the lattice distortion due to, respectively, a uniform strain and a strain-gradient deformation (22). One can then consider a *long-wavelength* acoustic phonon and derive (22) the flexoelectric response of a 3D bulk crystal through a long-wave expansion up to the second order in \mathbf{q} around Γ ($\mathbf{q} = 0$) of the polarization response to such a perturbation (22). A phonon perturbation can be written as

$$u_{\kappa\alpha}^{\text{I}}(t) = u_{\kappa\alpha}^{\mathbf{q}} e^{i\mathbf{q}\cdot\mathbf{R}_{I\kappa} - i\omega t}, \quad (3.12)$$

where $\mathbf{R}_{I\kappa}$, as usual, labels the atomic locations in the unperturbed crystal configuration and $u_{\kappa\alpha}^{\mathbf{q}}$ is a \mathbf{q} -dependent cell-periodic function that is solution of the eigenvalue

problem (46)

$$\Phi_{\kappa\alpha,\kappa'\beta}^{(\mathbf{q})} u_{\kappa'\beta}^{\mathbf{q}} = m_{\kappa} \omega^2(\mathbf{q}) u_{\kappa\alpha}^{\mathbf{q}}. \quad (3.13)$$

Considering only acoustic modes near $\mathbf{q} = 0$, for which $\mathbf{u}_{\kappa}^{\mathbf{q}=0} = \mathbf{u}$, a long-wave analysis of the above equation up to the second order in \mathbf{q} provides the following solution

$$u_{\kappa\alpha}^{\mathbf{q}} = \left(\delta_{\alpha\beta} + iq_{\gamma} \Gamma_{\alpha,\beta\gamma}^{\kappa} - q_{\gamma} q_{\lambda} N_{\alpha\beta,\gamma\lambda}^{\kappa} \right) u_{\beta} + \mathcal{O}(q^3). \quad (3.14)$$

Here Γ and \mathbf{N} are the piezoelectric and type-I flexoelectric internal-strain tensors, respectively (22). They describe the internal relaxation of the atoms due to a uniform strain and strain-gradient, respectively.

As shown in the previous chapter, the exact microscopic (adiabatic) polarization response of a 3D bulk material due to an acoustic phonon propagating at finite \mathbf{q} can be written as a cell-periodic \mathbf{q} -dependent function times a pure phase factor $e^{i\mathbf{q}\cdot\mathbf{r}}$,

$$P_{\alpha}(\mathbf{r}, t) = P_{\alpha,\kappa\beta}^{\mathbf{q}}(\mathbf{r}) u_{\kappa\beta}^{\mathbf{q}} e^{i\mathbf{q}\cdot\mathbf{r} - i\omega t}, \quad (3.15)$$

where $u_{\kappa\beta}^{\mathbf{q}}$ is the phonon eigendisplacement as provided in Eq.(3.14) and sum over repeated indexes is assumed. The macroscopic polarization is obtained by removing, from the microscopic response, the oscillations that occur on the scale of inter-atomic spacings:

$$P_{\alpha}^{\text{macro}}(\mathbf{r}, t) = \bar{P}_{\alpha,\kappa\beta}^{\mathbf{q}} u_{\kappa\beta}^{\mathbf{q}} e^{i\mathbf{q}\cdot\mathbf{r} - i\omega t}, \quad (3.16)$$

where $\bar{P}_{\alpha,\kappa\beta}^{\mathbf{q}}$ indicates the (3D) unit-cell average of the \mathbf{q} -dependent cell-periodic part of the microscopic response $P_{\alpha,\kappa\beta}^{\mathbf{q}}(\mathbf{r})$, (recall that we are interested in the long wave limit; in such a regime the phase factor $e^{i\mathbf{q}\cdot\mathbf{r}}$ varies slowly with respect to the space variables). From Eq.s (3.14) and (3.16) and by performing a long-wave expansion of $\bar{P}_{\alpha,\kappa\beta}^{\mathbf{q}}$ we can write (22)

$$\bar{P}_{\alpha}(\mathbf{r}, t) = \left(iq_{\gamma} u_{\beta} e_{\alpha,\beta\gamma} - q_{\gamma} q_{\lambda} u_{\beta} \mu_{\alpha\beta,\gamma\lambda}^{\text{I}} \right) e^{i\mathbf{q}\cdot\mathbf{r} - i\omega t}, \quad (3.17)$$

where \mathbf{e} and $\boldsymbol{\mu}$ are the piezoelectric and type-I flexoelectric tensors respectively, as defined above. Indeed, notice that the first and second terms at the right hand side of the above equation can be identified as the response to a uniform strain and a type-I strain-gradient, respectively, via the moments of the atomic displacements of Eq.(3.12), after specifying that $\mathbf{u}_{\kappa}^{\mathbf{q}=0} = \mathbf{u}$: $u_{\beta,\gamma} = iq_{\gamma} u_{\beta}$ and $-q_{\gamma} q_{\lambda} u_{\beta} = u_{\beta,\gamma\lambda}$. More explicitly, the piezoelectric and flexoelectric coefficients are formed from the following contributions (22)

$$e_{\alpha,\beta\gamma} = - \sum_{\kappa} \bar{P}_{\alpha,\kappa\beta}^{(1,\gamma)} + Z_{\kappa\rho}^{(\alpha)} \Gamma_{\rho,\beta\gamma}^{\kappa}, \quad (3.18)$$

$$\mu_{\alpha\beta,\gamma\lambda}^{\text{I}} = \frac{1}{2} \sum_{\kappa} \bar{P}_{\alpha,\kappa\beta}^{(2,\gamma\lambda)} - \frac{1}{2} \left(\bar{P}_{\alpha,\kappa\rho}^{(1,\lambda)} \Gamma_{\rho,\beta\gamma}^{\kappa} + \bar{P}_{\alpha,\kappa\rho}^{(1,\gamma)} \Gamma_{\rho,\beta\lambda}^{\kappa} \right) + \frac{1}{\Omega} Z_{\kappa,\rho}^{(\alpha)} N_{\rho\beta,\gamma\lambda}^{\kappa}, \quad (3.19)$$

where, again, summation over repeated indexes is assumed and the internal-strain fields of the eigendisplacements are included. Superscripts $(n, \gamma_1 \dots \gamma_n)$ indicate the n -order derivation in \mathbf{q} , while $Z_{\kappa,\rho}^{(\alpha)}$ are the dynamical Born charges. $\bar{P}_{\alpha,\kappa\beta}^{(1,\gamma)}$ and $\bar{P}_{\alpha,\kappa\beta}^{(2,\gamma\lambda)}$ correspond to the first and second real-space moments of the macroscopic polarization produced by the displacement of an isolated atom, and their sum over the

sublattice provide the *clamped-ion* contributions to the piezoelectric and flexoelectric tensors, respectively. The terms containing the Born charges correspond to the *lattice-mediated* contributions, while the terms in the brackets of Eq.(3.19) provide the “mixed” contribution to the bulk flexoelectric tensor (22).

3.2.2 Dynamical nature of the effect

Even though the piezoelectric coefficients of Eq. (3.18) are well known to be static quantities (48), the likewise obtained flexoelectric coefficients turn out to include a dynamic, i.e. mass-dependent, contribution. In order to see it, let us rewrite the flexoelectric coefficients of Eq.(3.19) in its type-II form (22),

$$\mu_{\alpha\lambda,\beta\gamma}^{\text{II}} = \mu_{\alpha\lambda,\beta\gamma}^{\text{II,CI}} - \bar{P}_{\alpha,\kappa\rho}^{(1,\lambda)} \Gamma_{\rho,\beta\gamma}^{\kappa} + \frac{1}{\Omega} Z_{\kappa,\rho}^{(\alpha)} L_{\rho\lambda,\beta\gamma}^{\kappa}. \quad (3.20)$$

Where we have explicitly carried out the sublattice summation in the first term at the r.h.s. that yields the clamped-ion (CI) flexoelectric tensor. The flexoelectric internal-strain tensor \mathbf{L} is defined as (22)

$$L_{\rho\lambda,\beta\gamma}^{\kappa} = \tilde{\Phi}_{\kappa\alpha,\kappa'\rho}^{(0)} \hat{C}_{\rho\lambda,\beta\gamma}^{\kappa'} \quad (3.21)$$

where $\tilde{\Phi}_{\kappa\alpha,\kappa'\rho}^{(0)}$ is the pseudoinverse of the zone-center force-constant matrix, $\Phi_{\kappa\alpha,\kappa'\beta}^{(0)}$ while $\hat{C}_{\rho\lambda,\beta\gamma}^{\kappa'}$ is the type-II *mass-compensated* flexoelectric force-response tensor as provided in Ref.(22). The latter is related to the elastic tensor $C_{\alpha\lambda,\beta\gamma}^{\kappa}$ of the crystal through (29; 22)

$$\hat{C}_{\alpha\lambda,\beta\gamma}^{\kappa} = C_{\alpha\lambda,\beta\gamma}^{\kappa} - \frac{m_{\kappa}}{M} \Omega C_{\alpha\lambda,\beta\gamma}, \quad (3.22)$$

with $C_{\alpha\lambda,\beta\gamma}^{\kappa}$ defined as in Ref. (22), m_{κ} being the mass of the κ sublattice and $M = \sum_{\kappa} m_{\kappa}$ the total mass of the sublattices within the unit cell, whose volume is indicated by Ω . Then the second term in the r.h.s. of Eq.(3.22) contains an explicit dependence on the sublattice mass and it is therefore a manifestation of the dynamic nature of the eigendisplacements, and therefore of the flexoelectric response.

The dynamic nature of the flexoelectric effect is actually not surprising and it can be rationalized as follows. A uniform strain can always be induced and sustained by applying a proper distribution of external loads to the surface of the sample. This is not valid for a strain-gradient. The latter is generally not a static configuration of the crystal interior that can be stabilized via boundary forces, and a uniform force field applied to each material point of the sample is needed to induce a given component of $\varepsilon_{\beta\gamma,\lambda}$. Such a uniform force can be, e.g., generated by a gravitational field(51) or, as in the above example, by the acceleration of each material point during its periodic oscillation provided by the sound wave (22). In either case, the result directly depends on the atomic masses. This implies that the flexoelectric coefficients are inherently dynamical in nature.

The dynamical nature of the flexoelectric effect might seem alarming if we want to use this theory to rationalize datas from experimental measurements, the latter being typically performed within a static regime. However, this is not a problem in real cases. Indeed in static equilibrium there can be several nonvanishing stress fields, and the condition that the force field must vanishing everywhere translates into (29; 22)

$$\sum_{\beta\gamma\lambda} \mathcal{C}_{\alpha\lambda,\beta\gamma} \varepsilon_{\beta\gamma,\lambda}(\mathbf{r}) = 0. \quad (3.23)$$

The total flexoelectric response of the material may then be expressed as a combination of the flexoelectric coefficients referred to the different strain-gradients $\{\varepsilon_{\beta\gamma,\lambda}\}_{\beta\gamma\lambda}$ involved. From Eq.(3.23) it is straightforward to show that the dynamic mass-dependent contributions of the different flexoelectric tensor components cancel each other and then the resulting response is appropriate to describe real effects and rationalize experimental data obtained in a static regime.

3.2.3 Treatment of the macroscopic electric field

A generic phonon propagating along \mathbf{q} in an insulator generally induces a microscopic electric field of the form $\mathbf{E}^{\mathbf{q}}(\mathbf{r})e^{i\mathbf{q}\cdot\mathbf{r}}$; with $\mathbf{E}^{\mathbf{q}}(\mathbf{r})$ being, as usual, a cell-periodic function. From Maxwell equations one can show that the macroscopic contribution to the cell-periodic part, corresponding to the $\mathbf{E}^{\mathbf{q}}(\mathbf{G} = 0)$ Fourier component, is a longitudinal vector (directed along \mathbf{q}) whose amplitude is equal to

$$\hat{\mathbf{q}} \cdot \mathbf{E}^{\mathbf{q}}(\mathbf{G} = 0) = -\frac{1}{\varepsilon_0} \frac{\hat{\mathbf{q}} \cdot \mathbf{P}^{\mathbf{q},\text{SC}}(\mathbf{G} = 0)}{\hat{\mathbf{q}} \cdot \boldsymbol{\epsilon} \cdot \hat{\mathbf{q}}}, \quad (3.24)$$

where $\hat{\mathbf{q}} = \mathbf{q}/q$ indicates the propagation direction of the phonon, ε_0 the vacuum permittivity, $\boldsymbol{\epsilon}$ the electronic macroscopic dielectric tensor of the material considered and $\mathbf{P}^{\mathbf{q},\text{SC}}(\mathbf{G} = 0)$ the macroscopic short-circuit (SC) polarization induced by the phonon perturbation. From Eq.(3.24) one realizes that the projection of the electric field along $\hat{\mathbf{q}}$ has a *non-analytic* behaviour in $\mathbf{q} = 0$ that depends on the direction with respect to which Γ is approached and that is fully contained in its longitudinal (macroscopic) component. Such a non-analytic behaviour propagates to any response function that is in relation with the electric field and it prevents to perform a proper Taylor expansion of the considered response function around $\Gamma(\mathbf{q}=0)$. This issue can be overcome by setting the macroscopic component of $\mathbf{E}^{\mathbf{q}}$ equal to zero, so that the non-analyticity is removed. From a physical point of view, this corresponds to enforce the so-called short-circuit electrical boundary conditions.

However, the notion of a macroscopic electric field is ambiguous in presence of strain gradients (22). This is because such type of deformations, contrary to what occurs for a uniform strain, does not affect (tilt) the quantum energy levels of the system in the same way (52). By this reason, the resulting macroscopic electric field will depend on which one of these energy levels we choose as our reference energy to define, and remove, the macroscopic field. This is usually referred to as “*reference potential ambiguity*” of the bulk flexoelectric tensor. The latter is indeed only defined modulo a constant term given by (22)

$$\Delta\mu_{\alpha\lambda,\beta\gamma} = \chi_{\alpha\lambda} \frac{\partial \mathcal{V}}{\partial \varepsilon_{\beta\gamma}}, \quad (3.25)$$

where $\chi_{\alpha\lambda}$ is the dielectric susceptibility, $\varepsilon_{\beta\gamma}$ the uniform strain, and \mathcal{V} an arbitrary (but compatible with the symmetries of the crystal) scalar function with the dimension of a potential. \mathcal{V} corresponds to the reference potential used to define the single-particle (Bloch) energy levels, and the presence of its derivative with respect to a uniform strain is directly related with the theory of *absolute deformation potentials* (52). However, we shall see soon that such an ambiguity is cancelled by the surface contributions occurring in a finite sample.

3.3 Treatment of finite samples in curvilinear coordinates

So far we have considered 3D bulk materials, defined as infinitely extended systems described by a 3D Bravais lattice. However, real materials are finite, and understanding how the details of the surfaces might influence the full flexoelectric response is of pivotal interest for a meaningful physical description of real samples and their possible employment in real devices.

Tagantsev and Yurkov (53), within a phenomenological theory, showed that the piezoelectric response of the surfaces contributes to the full flexoelectric response of a bent finite sample. Indeed, at surfaces space inversion symmetry is always broken, enabling a local piezoelectric response whose amplitude depends on the details of the termination. If we bend a slab, the strain at the outer and inner surfaces is opposite in sign, and it grows linearly with the slab thickness (for a given radius of curvature). This implies that the respective surface piezoelectric responses point towards the same direction, thus generating a total nonzero surface response that likewise grows linearly with the thickness of the slab. The latter is therefore comparable, at any size, to the bulk flexoelectricity, and the two effects need to be necessarily taken together for a fair representation of a typical bending experiment.

The inherent anisotropy of a finite slab introduces several difficulties that prevent the immediate use of the already defined 3D electromechanical response functions as derived in the previous sections. Indeed, in order to properly describe a slab, different Electrical Boundary Conditions (EBCs) must be imposed along different directions. The application of the required EBCs is further complicated by the fact that defining the in-plane and out-of-plane directions within a deformed configuration of the extended slab is not trivial. Following Ref.(23), the aforementioned issues can be overcome by employing a covariant reformulation of the microscopic fundamental electrostatic quantities within the curvilinear coordinate system of the comoving frame of the deformed slab. In the following we shall briefly summarize the basics of such a formulation.

3.3.1 General principles

Let us consider a generic deformation of the lattice described by a deformation field \mathbf{u} , $\mathbf{R}'_{I\kappa} = \mathbf{R}_{I\kappa} + \mathbf{u}(\mathbf{R}_{I\kappa})$. The curvilinear coordinate system \mathbf{r} associated to the comoving frame of the deformed sample, where the ions do not move from their reference locations, is then related to its Cartesian counterpart \mathbf{r}' through the mapping described by Eq.(3.1). Henceforth we will distinguish the Cartesian response functions from their curvilinear counterparts by indicating the latter with a hat symbol. Charge density, polarization and electric field are related to their Cartesian counterparts via the usual transformation rules for scalar density, contravariant vector density and covariant vector fields, respectively (23),

$$\hat{\rho}(\mathbf{r}) = h(\mathbf{r})\rho(\mathbf{r}'(\mathbf{r})), \quad (3.26)$$

$$\hat{P}_\alpha(\mathbf{r}) = h(\mathbf{r})(h^{-1})_{\alpha\beta}(\mathbf{r})P_\beta(\mathbf{r}'(\mathbf{r})), \quad (3.27)$$

$$\hat{E}_\alpha(\mathbf{r}) = h_{\alpha\beta}(\mathbf{r})E_\beta(\mathbf{r}'(\mathbf{r})), \quad (3.28)$$

where $h_{\alpha\beta}(\mathbf{r})$ is the deformation gradient

$$h_{\alpha\beta}(\mathbf{r}) = \frac{\partial r'_\alpha}{\partial r_\beta} = \delta_{\alpha\beta} + u_{\alpha,\beta}(\mathbf{r}), \quad (3.29)$$

and $h(\mathbf{r}) = \det(\mathbf{h}(\mathbf{r}))$ its determinant. The metric tensor in curvilinear coordinates, describing the distances within the curvilinear frame, reads as

$$\hat{g}_{\alpha\beta}(\mathbf{r}) = \sum_i \frac{\partial r'_i}{\partial r_\alpha} \frac{\partial r'_i}{\partial r_\beta} = (\mathbf{h}^T \mathbf{h})_{\alpha\beta}. \quad (3.30)$$

3.3.2 Curvilinear electrostatics

Within the prescriptions provided above, the local Maxwell equations in curvilinear coordinates read in the same way as their Cartesian counterparts

$$\hat{\nabla} \cdot (\hat{\epsilon} \cdot \hat{\mathbf{E}}) = \hat{\rho} \quad - \hat{\nabla} \cdot \hat{\mathbf{P}} = \hat{\rho}, \quad (3.31)$$

with the modification that the vacuum permittivity ϵ_0 is actually a tensor density field that transforms under change of coordinates as (23)

$$\hat{\epsilon}_{\alpha\beta}(\mathbf{r}) = \epsilon_0 \sqrt{\hat{g}(\mathbf{r})} \left(\hat{\mathbf{g}}^{-1}(\mathbf{r}) \right)_{\alpha\beta}, \quad (3.32)$$

where $\hat{g}(\mathbf{r}) = h^2(\mathbf{r})$ is the determinant of the curvilinear metric tensor $\hat{\mathbf{g}}$ as defined in Eq.(3.30). Equations (3.31) allow one to express the (curvilinear) electric field in terms of either the polarization or the charge density field and, since the electric field is defined through the gradient of the electric potential via $\hat{\mathbf{E}}(\mathbf{r}) = -\nabla \hat{V}(\mathbf{r})$ (the latter is a scalar field, and it is therefore invariant under coordinates transformation), the first-order response of the electric potential field $\hat{V}^{(1)}(\mathbf{r})$ can be expressed in terms of $\hat{\mathbf{P}}^{(1)}(\mathbf{r})$ (or $\hat{\rho}^{(1)}(\mathbf{r})$). At first order in the deformation, one finds

$$\epsilon_0 \hat{\nabla} \cdot \hat{\mathbf{E}}^{(1)}(\mathbf{r}) = -\hat{\nabla} \cdot \left(\hat{\epsilon}^{(1)}(\mathbf{r}) \cdot \hat{\mathbf{E}}^{(0)}(\mathbf{r}) + \hat{\mathbf{P}}^{(1)}(\mathbf{r}) \right), \quad (3.33)$$

where the first term in the brackets of the r.h.s. of Eq.(3.33) comes from the linear (purely geometric) variation of the curvilinear vacuum permittivity tensor (Eq.(3.32)), and it can be expressed as follows,

$$\left(\hat{\epsilon}^{(1)}(\mathbf{r}) \cdot \hat{\mathbf{E}}^{(0)}(\mathbf{r}) \right)_\alpha = \epsilon_0 E_{\alpha,\beta\gamma}^{(\text{met})}(\mathbf{r}) u_{\beta,\gamma}(\mathbf{r}), \quad (3.34)$$

with

$$E_{\alpha,\beta\gamma}^{(\text{met})}(\mathbf{r}) = \left(\delta_{\beta\gamma} E_\alpha^{(0)}(\mathbf{r}) - \delta_{\alpha\beta} E_\gamma^{(0)}(\mathbf{r}) - \delta_{\alpha\gamma} E_\beta^{(0)}(\mathbf{r}) \right). \quad (3.35)$$

$\mathbf{E}^{(0)}(\mathbf{r})$ is the Cartesian representation of the microscopic electric field within the unperturbed configuration. Eq.(3.33) specifies $\hat{\mathbf{E}}^{(1)}(\mathbf{r})$ modulo a \mathbf{r} -independent constant, the latter fixed by the EBCs assumed. While the response functions are typically calculated within Short-Circuit (SC) conditions, any EBCs can be employed if the linear response of the relevant response functions to a macroscopic electric field is known (and this is the case for the polarization, for example). This means that Eq.(3.33) is always valid, as long as $\mathbf{P}^{(1)}$ is properly defined and calculated within the required EBCs.

3.3.3 Perturbative expansion

From Eqs (3.26)-(3.28), one finds that the response of the curvilinear coordinate representation of a microscopic field f (either the charge density, the polarization or the electric field) to a slowly varying (on the scale of the lattice spacings) inhomogeneous

strain field $u_{\alpha,\beta}(\mathbf{r})$ enjoys the following gradient expansion (29; 23),

$$\hat{f}^{(1)}(\mathbf{r}) = u_{\beta,\gamma}(\mathbf{r})f_{\beta\gamma}^U(\mathbf{r}) + \frac{\partial u_{\beta,\gamma}(\mathbf{r})}{\partial r_\lambda} f_{\beta,\gamma\lambda}^G(\mathbf{r}) + \dots \quad (3.36)$$

For a crystal, $f_{\beta\gamma}^U(\mathbf{r})$ and $f_{\beta,\gamma\lambda}^G(\mathbf{r})$ are cell-periodic functions describing the microscopic response to a uniform strain (U), and the additional contributions arising from the first gradient (G) of the strain. In particular, $f_{\beta\gamma}^{(U)}(\mathbf{r})u_{\beta,\gamma}(\mathbf{r})$ takes the meaning of a local piezoelectric response. Eq. (3.36) highlights the advantage of the coordinate transformations formalism, allowing to define the *microscopic* response of a finite sample to an arbitrary deformation.

In the following we shall base our description on the long-wave analysis of the response functions to an acoustic phonon within the lattice dynamic theory as provided in Sec. 3.2. To this end, we assume that the atoms of the crystal undergo a frozen-ion (the relaxed-ion case is uncomplicated and it will be considered shortly) displacement field of the form $u_{\kappa\alpha}^l = u_\alpha e^{i\mathbf{q}\cdot\mathbf{R}_{l\kappa}}$. Following the prescriptions given above, the curvilinear coordinates system \mathbf{r} associated to the comoving frame of the deformed sample is related to its Cartesian counterpart \mathbf{r}' through the mapping

$$r'_\beta = r_\beta + u_\beta e^{i\mathbf{q}\cdot\mathbf{r}}. \quad (3.37)$$

By performing a long-wave expansion of the Cartesian response functions involved in Eqs.(3.26)-(3.27) (22) and by applying the coordinate transformation rules as provided above to the case of the acoustic phonon deformation, one finds

$$\hat{\rho}^{(1),\text{CI}}(\mathbf{r}) = u_{\beta,\gamma}(\mathbf{r}) \underbrace{\left(\delta_{\beta\gamma} \rho^{(0)}(\mathbf{r}) - \rho_\beta^{(1,\gamma)}(\mathbf{r}) \right)}_{\rho_{\beta\gamma}^{(U),\text{CI}}(\mathbf{r})} + u_{\beta,\gamma\lambda}(\mathbf{r}) \underbrace{\frac{1}{2} \rho_\beta^{(2,\gamma\lambda)}(\mathbf{r})}_{\rho_{\beta,\gamma\lambda}^{(G),\text{CI}}(\mathbf{r})}, \quad (3.38)$$

$$\hat{P}_\alpha^{(1),\text{CI}}(\mathbf{r}) = -u_{\beta,\gamma}(\mathbf{r}) \underbrace{P_{\alpha\beta}^{(1,\gamma)}(\mathbf{r})}_{P_{\alpha,\beta\gamma}^{(U),\text{CI}}(\mathbf{r})} + u_{\beta,\gamma\lambda}(\mathbf{r}) \underbrace{\frac{1}{2} P_{\alpha\beta}^{(2,\gamma\lambda)}(\mathbf{r})}_{P_{\alpha,\beta,\gamma\lambda}^{(G),\text{CI}}(\mathbf{r})}. \quad (3.39)$$

Their Relaxed-Ion (RI) version is obtained by substituting the CI response functions $f_\beta^{(1,\gamma)}(\mathbf{r})$ and $f_\beta^{(2,\gamma\lambda)}(\mathbf{r})$ with their relaxed-ion counterparts (22)

$$\begin{aligned} -f_\beta^{(1,\gamma)}(\mathbf{r}) &\longrightarrow -f_\beta^{(1,\gamma)}(\mathbf{r}) + f_{\kappa\rho}^{(0)}(\mathbf{r})\Gamma_{\rho,\beta\gamma}^\kappa \\ \frac{1}{2}f_\beta^{(2,\gamma\lambda)}(\mathbf{r}) &\longrightarrow \frac{1}{2}f_\beta^{(2,\gamma\lambda)}(\mathbf{r}) - \frac{1}{2} \left[f_{\kappa\rho}^{(1,\lambda)}(\mathbf{r})\Gamma_{\rho,\beta\gamma}^\kappa + f_{\kappa\rho}^{(1,\gamma)}(\mathbf{r})\Gamma_{\rho,\beta\lambda}^\kappa \right] \\ &\quad + f_{\kappa\rho}^{(0)}(\mathbf{r})N_{\rho\beta,\gamma\lambda}^\kappa. \end{aligned} \quad (3.40)$$

In this way, one obtains a direct relation between the first-order response of the curvilinear representation of the relevant fields and their standard Cartesian response to a uniform strain and a uniform strain-gradient, respectively. One can also readily verify that the continuity equation $-\hat{\nabla} \cdot \hat{\mathbf{P}}^{(1)}(\mathbf{r}) = \hat{\rho}^{(1)}(\mathbf{r})$ is satisfied, as it should be. Similarly, by combining the expressions for $\hat{\rho}^{(1)}$ and $\hat{\mathbf{P}}^{(1)}$ with Eq.(3.33), it follows that the first-order response of the (curvilinear) electric field to an inhomogeneous strain field reads as

$$\hat{E}_\alpha^{(1)}(\mathbf{r}) = u_{\beta,\gamma}(\mathbf{r})E_{\alpha,\beta\gamma}^{(U)}(\mathbf{r}) + u_{\beta,\gamma\lambda}(\mathbf{r})E_{\alpha,\beta,\gamma\lambda}^{(G)}(\mathbf{r}), \quad (3.41)$$

with

$$E_{\alpha,\beta\gamma}^{(U)}(\mathbf{r}) = -\frac{1}{\epsilon_0}P_{\alpha,\beta\gamma}^{(U)}(\mathbf{r}) - E_{\alpha,\beta\gamma}^{(\text{met})}(\mathbf{r}), \quad (3.42)$$

$$E_{\alpha\beta,\gamma\lambda}^{(G)}(\mathbf{r}) = -\frac{1}{\epsilon_0}P_{\alpha\beta,\gamma\lambda}^{(G)}(\mathbf{r}). \quad (3.43)$$

and $E_{\alpha,\beta\gamma}^{(\text{met})}(\mathbf{r})$ defined as provided in Eq.(3.35). The type-II representation of the objects derived above is readily obtained by applying a permutation of indices analogous to that of Eq.(3.10).

3.3.4 3D flexovoltage

In order to further illustrate how the surfaces affect the flexoelectric response of a finite sample and why their contribution is important even in the case of a macroscopically thick sample, let us follow Ref. (26) and consider a symmetrically terminated slab of thickness t made of a centrosymmetric material. Then, let us study its out-of-plane response due to a bending deformation such as the one illustrated in Fig. 3.1. The latter is formally described by a strain field nonuniform along the out-of-plane direction (z) as $\varepsilon_{\beta\beta}(\mathbf{r}) = z\varepsilon_{\beta\beta,z}$, where $\varepsilon_{\beta\beta,z}$ is the effective strain gradient induced by the bending deformation. The out-of-plane electrical response of such a slab suspended in vacuum is conveniently described by the open-circuit voltage drop across the slab, ΔV^{OC} , induced by the deformation (26). Indeed the latter choice has two main advantages with respect to working with a short-circuit polarization: *i*) it is invariant under change of coordinates, since it is a scalar field, and therefore free of ambiguities (contrary to e.g. the dipolar moment); *ii*) it can be more easily measured in a typical experimental setup.

We therefore define the response of the macroscopic slab as the thermodynamic limit of the derivative of the voltage drop with respect to the applied uniform strain gradient $\varepsilon_{\beta\beta,z}$,

$$\varphi^{3\text{D}} = \lim_{t \rightarrow \infty} \frac{1}{t} \frac{\partial \Delta \hat{V}^{\text{OC}}}{\partial \varepsilon_{\beta\beta,z}}, \quad (3.44)$$

and refer to it as 3D flexovoltage. The corresponding out-of-plane component of the (curvilinear) electric field induced by the deformation can be written, following the prescriptions provided in the previous section, as follows

$$\frac{\partial \hat{E}_z(z)}{\partial \varepsilon_{\beta\beta,z}} = \hat{E}_{z,\beta\beta}^{(U)}(z)z + \hat{E}_{zz,\beta\beta}^{(G)}(z), \quad (3.45)$$

where we have considered the “planar and macroscopic averages” of the response functions involved (26), in order to appropriately filter out the oscillations occurring at the interatomic spacings.

In first place, notice that the unperturbed macroscopic potential associated to the reference configuration is a symmetric well with depth ϕ . As illustrated in Fig. 3.2(a), the electrical field induced by a uniform strain, $\hat{E}_{z,\beta\beta}^{(U)}(z)$, vanishes in the interior of the slab (recall that we are assuming a centrosymmetric crystal) but it is finite within a thin region surrounding the surfaces, where a piezoelectric response is allowed by the local inversion- symmetry breaking. However, the application of a uniform strain $\varepsilon_{\beta\beta}$ does not break the overall inversion symmetry of the system, thus the induced dipoles at opposite surfaces cancel out and the only resulting macroscopic

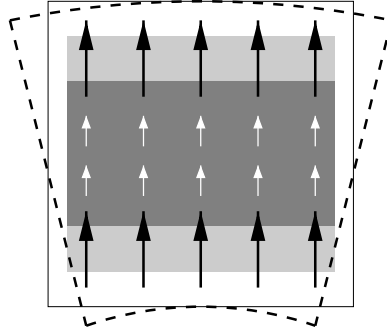


FIGURE 3.1: Bending of a finite slab. The electric field induced within the surface- and bulk-regions of the sample is schematically shown. The surface and bulk electric fields are discussed in more detail in Fig. 3.2.

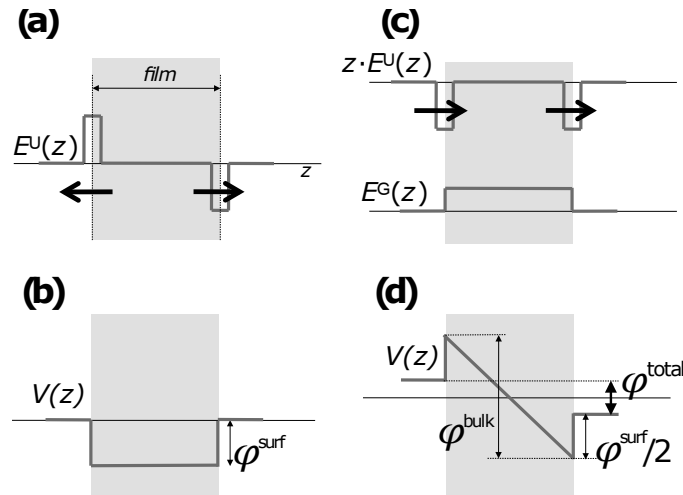


FIGURE 3.2: Macroscopic electric, (a)-(c), and potential, (b)-(d), fields induced in the slab by a uniform strain, (a)-(b), and a uniform strain-gradient, (c)-(d), respectively. In panel (c) the surface and bulk contributions to the induced electric field are separately shown.

effect is that of changing the depth of the symmetric well (Fig. 3.2(b)) but no voltage drop develops across the slab, as expected for a nonpiezoelectric one.

Conversely, a uniform strain-gradient of the form $\varepsilon_{\beta\beta,z}$ (with $\beta = x$ or y) provides opposite local strains on the two surfaces, with values $\varepsilon_{\beta\beta} = \pm\varepsilon_{\beta\beta,z}t/2$, respectively. Then the electric fields induced by means of the local piezoelectric effect at the boundaries of the slab have the same sign (top side of panel (c) in Fig. 3.2) and add to a surface flexovoltage given by

$$\varphi^{\text{surf}} = \lim_{t \rightarrow \infty} \frac{1}{t} \frac{\partial \phi}{\partial \varepsilon_{\beta\beta}} t = \frac{\partial \phi}{\partial \varepsilon_{\beta\beta}}. \quad (3.46)$$

Such a term depends on the details of the surfaces and survives in the large thickness limit, regardless the symmetries of the system. In turn, the contribution $E_{zz,\beta\beta}^{(G)}(z)$ turns out to be zero outside the sample (consistent with the open-circuit EBC used) and constant in the interior region (bottom side of panel (c) in Fig. 3.2), with a value that is independent of the surface terminations. The bulk electric field therefore displays a capacitor-like behavior, and the bulk contribution to the flexovoltage can be written as (29; 23)

$$\varphi^{\text{bulk}} = \frac{L}{\epsilon_0} \frac{\mu_{zz,\beta\beta}^{\text{II}}}{\epsilon_{zz}}, \quad (3.47)$$

with ϵ_{zz} the out-of-plane dielectric constant, $\mu_{zz,\beta\beta}^{\text{II}}$ the short-circuit flexoelectric coefficient referring to the the supercell where the slab is accommodated in and L the out-of-plane dimension of the latter. The total flexovoltage, $\varphi^{\text{tot}} = \varphi^{\text{surf}} + \varphi^{\text{bulk}}$, is shown in Fig. 3.2(d).

To conclude this chapter, it is important to notice that the quantity $\partial \phi / \partial \varepsilon_{\beta\beta}$ suffers from the same reference potential ambiguity discussed in Sec. 3.2.3 for the case of the bulk flexoelectric tensor. In fact, to define a surface potential offset one likewise needs to choose a reference energy inside the material. The interesting result is that both ambiguities cancel out when the two terms (φ^{bulk} and φ^{surf}) are summed up, yielding a well-defined total flexovoltage response of the slab as a whole.

Chapter 4

Out-of-plane response

Here, we define and calculate the out-of-plane flexoelectric response as the open-circuit voltage response to a flexural deformation (“flexovoltage”) of the 2D crystal in the linear regime. Building on the recently-developed implementation of bulk flexoelectricity in 3D, (27; 54) we show that the flexovoltage coefficient, φ , is a fundamental linear-response property of the crystal, and can be calculated by using the primitive 2D cell of the unperturbed flat layer. We find that the overall response consists in two well-defined contributions, a clamped-ion (CI) and a lattice-mediated (LM) term, in close analogy with the theory of the piezoelectric response. (48) At the CI level, our calculations show a remarkable cancellation between a dipolar linear-response term and a previously overlooked “metric” contribution, which we rationalize in terms of an intuitive toy model of noninteracting neutral spheres. (23; 29)

4.1 Flexural deformations in quasi-2D materials

Our goal is to describe the flexoelectric response of a quasi-2D material due to a *flexural deformation*. In this section we will properly define the latter from a geometrical point of view.

4.1.1 Nanotube geometry

For simplicity, we start defining some basic concepts in the special case of a cylindrical geometry, and move on to the study of general flexural deformations later

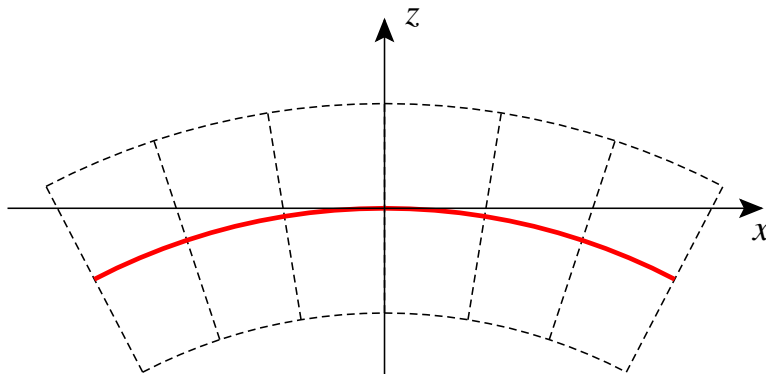


FIGURE 4.1: Illustration of the macroscopic deformation field in a vicinity of a bent layer; the two-dimensional crystal is indicated by a thicker red curve.

on. Let us consider the mechanical deformation illustrated in Fig. 4.1, which corresponds to folding a flat monolayer into a cylindrical nanotube geometry with radius R . The transformation of the crystal is conveniently described by a mapping between a curvilinear and Cartesian frame of the type

$$x = (\zeta_3 + R) \sin\left(\frac{\zeta_1}{R}\right), \quad (4.1a)$$

$$z = (\zeta_3 + R) \cos\left(\frac{\zeta_1}{R}\right) - R, \quad (4.1b)$$

where ζ_3 spans the radial direction, while ζ_1 runs over the tangential direction. In the limit of large R , in a neighborhood of the origin we have immediately

$$x \simeq \zeta_1 + \frac{\zeta_1 \zeta_3}{R}, \quad (4.2a)$$

$$z \simeq \zeta_3 - \frac{\zeta_1^2}{2R}, \quad (4.2b)$$

corresponding to a macroscopic transverse strain gradient that is proportional to $1/R$.

For a more rigorous derivation, one can define the deformation gradient as

$$h_{\alpha\beta} = \frac{\partial r_\alpha}{\partial \zeta_\beta}, \quad \mathbf{h} = \begin{vmatrix} \frac{\zeta_3+R}{R} \cos\left(\frac{\zeta_1}{R}\right) & \sin\left(\frac{\zeta_1}{R}\right) \\ -\frac{\zeta_3+R}{R} \sin\left(\frac{\zeta_1}{R}\right) & \cos\left(\frac{\zeta_1}{R}\right) \end{vmatrix} \quad (4.3)$$

The metric tensor of the deformation is then defined by

$$\mathbf{g} = \mathbf{h}^T \mathbf{h}, \quad \mathbf{g} = \begin{vmatrix} \frac{(\zeta_3+R)^2}{R^2} & 0 \\ 0 & 1 \end{vmatrix}. \quad (4.4)$$

The Lagrange strain tensor is defined in terms of the metric tensor as

$$\boldsymbol{\varepsilon} = \frac{1}{2}(\mathbf{g} - \mathbf{I}), \quad \boldsymbol{\varepsilon} \simeq \frac{1}{R} \begin{vmatrix} \zeta_3 & 0 \\ 0 & 0 \end{vmatrix}, \quad (4.5)$$

where in the second equality we have assumed that ζ_3/R is a small number, consistent with the large- R limit that is implicit in our theory. We obtain a linear variation of ε_{xx} along the out-of-plane coordinate, leading to inverse radius of curvature $1/R$ that is equivalently given by

$$\frac{1}{R} \simeq \frac{1}{2} \frac{\partial g_{11}}{\partial \zeta_3} = \varepsilon_{xx,z}. \quad (4.6)$$

In other words, in the limit of large radius, the nanotube geometry locally recovers a bending deformation described by a single strain-gradient component of the type $\varepsilon_{xx,z} = 1/R$.

4.1.2 Curvature tensor

In the following we will base our discussion on a more general ground. In the language of differential geometry, the geometric configuration of a deformed surface embedded in the 3D space is conveniently specified via a vector function of two

variables, $\mathbf{r} = \mathbf{r}(u, v)$, where \mathbf{r} is a point in three-dimensional (3D) space in the deformed configuration, and uv refers to a local parametrization of the (flat) reference state (55). The distances between the material points of the deformed configuration can be described by use of the so called *first fundamental form*. By indicating with $\xi_\alpha = u, v$ the reference coordinates (from now on, we shall use Greek indices for the in-plane uv directions), the latter reads as

$$g_{\alpha\beta}^{2D}(\xi) = \mathbf{r}_\alpha(\xi) \cdot \mathbf{r}_\beta(\xi), \quad (4.7)$$

where $\mathbf{r}_\alpha(\xi) = \partial \mathbf{r}(\xi) / \partial \xi_\alpha$ is a deformation gradient and $g_{\alpha\beta}^{2D}(\xi)$ is the (2D) metric tensor defined on the tangent space generated by $\mathbf{r}_u(\xi)$ and $\mathbf{r}_v(\xi)$ at $\mathbf{r}(\xi)$, hence the choice of the notation for the first fundamental form. The local curvature, in turn, is well described by the matrix elements of the *second fundamental form*, $b_{\alpha\beta} = \mathbf{r}_{\alpha\beta} \cdot \mathbf{n}$, where the subscripts $\alpha\beta$ stand for (second) differentiation with respect to u, v and $\mathbf{n}(u, v)$ is the normal to the oriented surface. (We choose it in such a way that \mathbf{r}_u , \mathbf{r}_v and \mathbf{n} form a right-handed set.) Notice that, whenever $g_{\alpha\beta}^{2D}(\xi) = \delta_{\alpha\beta}$ (i.e., the local basis of the tangent space is orthonormal), the tensor \mathbf{b} corresponds to the shape-operator (55). The eigenvalues and eigenvectors of the latter are the so-called *principal curvatures*, K_i , and *principal directions*, λ_i , respectively. One can write

$$b_{\alpha\beta} = - \sum_i K_i \lambda_i^\alpha \lambda_i^\beta, \quad (4.8)$$

with λ_i^α the projection of λ_i on \mathbf{r}_α ($\alpha = u, v$). In particular, when $g_{\alpha\beta}^{2D}(\xi) = \delta_{\alpha\beta}$, we locally recover the case of the cylindrical nanotube geometry described in Sec. 4.1.1 in the case of a purely 2D surface where the eigenvalues of the second fundamental form assume the intuitive geometrical meaning of an inverse radius of curvature (see Eq. 4.2b for $\xi_3 = 0$),

$$K_\alpha = \frac{1}{R_\alpha}; \quad (4.9)$$

hence the choice of the sign in Eq. (4.8).

Real materials, however, are “quasi-2D”, i.e., they are extended in plane but have a nonvanishing thickness along the surface normal (z). Consequently, in practical calculations one needs to assume a 3D-3D mapping $\mathbf{r}'(u, v, w)$, involving a region of space that is thin but finite along w . For a reasonably small value of w , we can consider a 3D-3D mapping of the form

$$\mathbf{r}' = \mathbf{r}(u, v) + w\mathbf{n}(u, v). \quad (4.10)$$

By assuming $\xi_1 = u$, $\xi_2 = v$ and $\xi_3 = w$, the distances between the points of the quasi-2D deformed configuration are described by the 3D metric tensor

$$g_{ij} = \frac{\partial r'_k}{\partial \xi_i} \frac{\partial r'_k}{\partial \xi_j}, \quad (4.11)$$

with latin indexes indicating the 3D coordinates and $\partial r'_k / \partial \xi_i$ indicating, again, a deformation gradient. It is readily shown that, within the choice assumed for the 3D-3D mapping (Eq. 4.10), for any u, v, w the 3D metric tensor reads as

$$\mathbf{g} = \begin{pmatrix} \mathbf{g}^{2D} & \mathbf{0} \\ \mathbf{0} & 1 \end{pmatrix}, \quad (4.12)$$

with

$$\tilde{g}_{\alpha\beta}^{2D}(u, v, w) = g_{\alpha\beta}^{2D}(u, v) - 2w (\mathbf{r}_{\alpha\beta}(u, v) \cdot \mathbf{n}) - 2w^2 (\mathbf{n}_{\alpha\beta}(u, v) \cdot \mathbf{n}). \quad (4.13)$$

and $\mathbf{n}_{\alpha\beta}$ indicating the second differentiation of the normal vector to the oriented surface, $\mathbf{n}(u, v)$, with respect to u, v . From Eq.(4.13), one can realize that the derivative of the 3D metric with respect to w , evaluated at $w = 0$, provides the second fundamental form as defined above for the strict 2D case,

$$-\frac{1}{2} \frac{\partial g_{\alpha\beta}}{\partial w} \Big|_{w=0} = \mathbf{r}_{\alpha\beta} \cdot \mathbf{n}. \quad (4.14)$$

At the linear order in the deformation (that is the regime we are interested in), one finds $\mathbf{n} \cdot \mathbf{r}_{\alpha\beta} = \hat{z} \cdot \mathbf{r}_{\alpha\beta}$ and the matrix elements of \mathbf{b} are then given by

$$b_{\alpha\beta} = -\frac{1}{2} \frac{\partial g_{\alpha\beta}}{\partial z}. \quad (4.15)$$

Recalling that in the linear regime the gradient of the metric relates to the “type-II” representation of the strain-gradient tensor through

$$\frac{1}{2} \frac{\partial g_{ij}}{\partial \tilde{\epsilon}_k} \simeq \frac{\partial \varepsilon_{ij}}{\partial \tilde{\epsilon}_k} = \varepsilon_{ij,k}, \quad (4.16)$$

where ε_{ij} is the symmetrized infinitesimal strain, we conclude that in the context of quasi-2D materials we have

$$b_{\alpha\beta}(u, v) = -\varepsilon_{\alpha\beta,z}(u, v). \quad (4.17)$$

This means that the type-II strain-gradient $\varepsilon_{\alpha\beta,z}$ equivalently describes the local curvature of the generic deformed configuration of a quasi-2D system.

4.2 Flexovoltage in 2D crystals

The fundamental quantity that we shall address here is the voltage drop across a thin layer due to a flexural deformation, where the latter is measured by the radius of curvature, R . At the leading order, the voltage drop is inversely proportional to R

$$\Delta V = \frac{\varphi}{R} + O(R^{-2}), \quad \varphi = \frac{\mu^{2D}}{\epsilon_0}, \quad (4.18)$$

where φ can also be expressed as a 2D flexoelectric coefficient (in units of charge, describing the *effective* dipole per unit area that is linearly induced by a flexural deformation) divided by the vacuum permittivity, ϵ_0 . Our goal is to calculate the constant of proportionality, φ , which we shall refer to as *2D flexovoltage coefficient*. Notice the difference with the 3D flexovoltage defined in section 3.3.4, where the thermodynamic limit was considered.

The underlying physical model is that of a nanotube of radius R (see section 4.1.1) constructed by bending a flat layer, as illustrated in Fig.4.2(a); the voltage drop between the interior and the exterior is then given by Eq. (4.18).

Another obvious example is that of a long-wavelength flexural phonon [see Fig. 4.2(b)]. Due to rotational invariance, the modulated strain field locally recovers the same pattern as in Fig.4.2(a). [See Ref. (23) and Sec. 2.8.2 of Ref. (29).] At the leading order

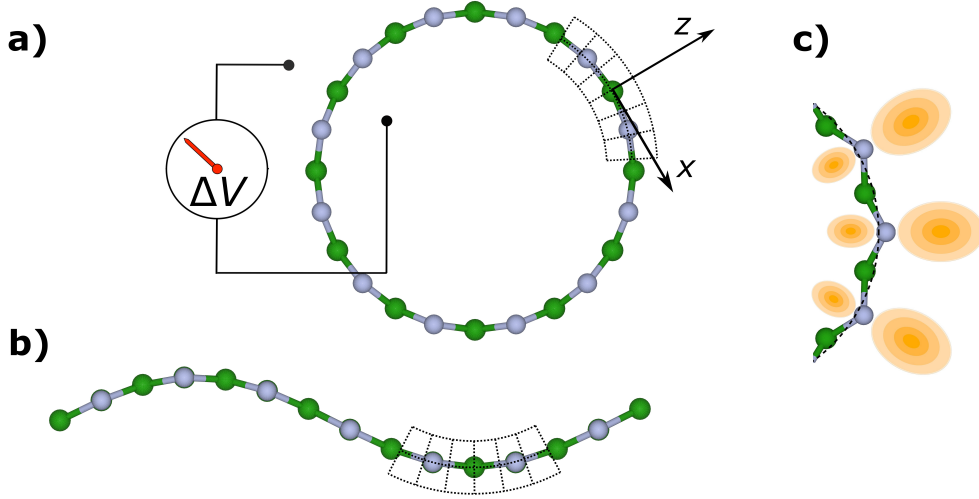


FIGURE 4.2: Schematic illustration of the flexoelectric response in BN. (a): Cross-section of a BN nanotube; the voltage drop between its inner and outer sides is highlighted. (b): Flexural phonon, corresponding to an in-plane modulation of the same strain field as in (a). (c): Lattice-mediated and purely electronic effects contributing to the dipole. Gray/green circles represent the B/N atoms. The deformed electronic orbitals are shown as yellow shaded ellipses.

in the wave vector, \mathbf{q} , this results in a local jump in the electrostatic potential across the layer of

$$\Delta V(x, y) = \varphi K(x, y), \quad (4.19)$$

where $K(x, y) = -\text{Tr}(\mathbf{b})(x, y) \simeq -\nabla^2 u_z(x, y)$, is given by the Laplacian of the vertical displacement field, u_z (see Supplemental Material of Ref. (56)). As we shall see shortly, the effect originates from the distortion of both the electronic cloud and the crystal structure [Fig.4.2(c)].

In the most general case, the φ coefficients of Eq.(4.18) and (4.19) depend on the direction along which the layer is bent. Then, the open-circuit voltage must be related to the local curvature tensor via

$$\Delta V(x, y) = \varphi_{zz, \beta\gamma} \varepsilon_{\beta\gamma, z}(x, y), \quad (4.20)$$

where φ is a 2x2 tensor. Most materials we consider, with the sole exception of black phosphorene, have a three-fold axis; in that case, $\varphi_{zz, \beta\gamma} = \varphi \delta_{\beta\gamma}$ and Eq.(4.20) reduces to (4.19).

4.3 Electric Boundary Conditions

Before presenting our formal results, we comment briefly on an important technical issue in the definition and calculation of the flexovoltage as a linear-response property. In the remainder of this Chapter, we shall be dealing with the long-wavelength limit of some specific phonon modes of a 2D layer. The appropriate electrical boundary conditions (EBCs) are those of a free-standing layer. This implies setting open-circuit EBC along the out-of-plane direction, z , and short-circuit EBC in plane; we shall indicate them as "*mixed EBCs*" or "*2D-EBCs*" henceforth.

These boundary conditions can be, in principle, reproduced by choosing an appropriate 2D Coulomb kernel (57) in the linear-response calculations of the intermediate quantities. This kernel, however, was not yet available in ABINIT at the time this work was carried out; so, in practice, we performed our calculations in a supercell with the standard 3D Coulomb kernel, and converted all the results into a 2D-EBCs form (see Appendix A.1 for details) before inserting them in the formulas of this Chapter. For simplicity, we will assume henceforth that all quantities in such formulas are already in 2D-EBCs; for this reason, they may differ in places from those presented in our Ref.(56), where a different convention was used.

4.4 First-principles theory and methods

Following the arguments of section 3.3.3, the relevant components of the flexovoltage are given by

$$\varphi_{zz,\alpha\alpha} = \frac{\partial V}{\partial \varepsilon_{\alpha\alpha,z}} = \frac{1}{S\epsilon_0} \int_{\Omega} d^3r \left[z \left(P_{z,\alpha\alpha}^U(\mathbf{r}) + E_z^{(0)}(\mathbf{r}) \right) + P_{zz,\alpha\alpha}^G(\mathbf{r}) \right]. \quad (4.21)$$

Here $E_z^{(0)}(\mathbf{r})$ is the electric field in the unperturbed configuration and it corresponds to the metric contribution $E_{z,\alpha\alpha}^{\text{met}}(\mathbf{r})$ (Eq.(3.35)) associated to a symmetrized strain field of the kind $\varepsilon_{\alpha\alpha}(\mathbf{r})$. S and Ω indicate the unit-cell surface of the unperturbed 2D crystal and the volume of the supercell where the layer is accommodated in, respectively. The integral of the second term in the square brackets can be worked out by noticing that the cell average of $P_{zz,\alpha\alpha}^G(\mathbf{r})$ over a supercell containing the layer corresponds to the (type-II) macroscopic 3D flexoelectric tensor, μ , of the slab/vacuum superlattice. We can then define

$$\varphi_{zz,\alpha\alpha}^G = L \frac{\mu_{zz,\alpha\alpha}^{\text{II}}}{\epsilon_0}, \quad (4.22)$$

where L is the out-of-plane parameter describing the supercell. Regarding the remainder contribution, it can be easily calculated by parts by exploiting the fact that the system is finite along direction z and by observing that $\rho_{\alpha\alpha}^{(U)}(\mathbf{r}) = -dP_{z,\alpha\alpha}^{(U)}(\mathbf{r})/dz$ and $\rho^{(0)}(\mathbf{r}) = \epsilon_0 dE_z^{(0)}(\mathbf{r})/dz$. One arrives to

$$\varphi_{zz,\alpha\alpha}^U = \frac{1}{2S\epsilon_0} \int_{\Omega} d^3r z^2 \rho_{\alpha\alpha}^U(\mathbf{r}), \quad (4.23)$$

$$\varphi_{zz,\alpha\alpha}^M = -\frac{1}{2S\epsilon_0} \int_{\Omega} d^3r z^2 \rho^{(0)}(\mathbf{r}), \quad (4.24)$$

where the superscripts indicate the uniform strain (U) and metric (M) contributions, respectively. $\rho^{(0)}(\mathbf{r})$ is the total ground-state charge density of the slab, including electrons and ions, while $\rho_{\alpha\alpha}^U(\mathbf{r})$ is the relaxed-ion charge-density response to a uniform strain $\varepsilon_{\alpha\alpha}$. We finally conclude that the *relaxed-ion* flexovoltage can be calculated as

$$\varphi_{zz,\alpha\alpha} = L \frac{\mu_{zz,\alpha\alpha}^{\text{II}}}{\epsilon_0} + \frac{1}{2S\epsilon_0} \mathcal{Q}[\rho_{\alpha\alpha}^{(U)}] - \frac{1}{2S\epsilon_0} \mathcal{Q}[\rho^{(0)}], \quad (4.25)$$

where we have indicated with $\mathcal{Q}[f]$ the quadrupolar moment of a generic function f along z . Eq. (4.25) is directly suitable for a numerical implementation, as it only requires response functions that are routinely calculated with the linear-response and long-wave (27; 54; 28) modules of ABINIT. We stress that the CI flexoelectric tensor,

and the intermediate quantities (Born charges, quadrupoles, pseudoinverse, force-response tensors) defining its relaxed counterpart, are typically calculated within SC conditions. However, their *mixed EBCs* version can be readily obtained from the SC ones as postprocessed quantities, as illustrated in Sec. A.1.

4.4.1 Clamped-Ion and Lattice-Mediated contributions

Eq. (4.25) can be recast in a more meaningful form, by seeking a separation between CI and LM effects. The total flexovoltage can be written as

$$\varphi_{zz,\alpha\alpha} = \varphi_{zz,\alpha\alpha}^{\text{CI}} + \Delta\varphi_{zz,\alpha\alpha}. \quad (4.26)$$

The *clamped-ion* flexovoltage is obtained by employing in Eq.(4.25) the CI counterpart of the involved response functions. One readily obtains

$$\varphi_{zz,\alpha\alpha}^{\text{CI}} = L \frac{\mu_{zz,\alpha\alpha}^{\text{CI,II}}}{\epsilon_0} + \frac{1}{2S\epsilon_0} \mathcal{Q}[\rho_{\alpha\alpha}^{(\text{U,CI})}] - \frac{1}{2S\epsilon_0} \mathcal{Q}[\rho^{(0)}]. \quad (4.27)$$

Notice that the sum of the first two terms in the r.h.s. of Eq.(4.27) is related to the dipolar moment of the CI first-order response of the charge-density, $\mathcal{D}[\hat{\rho}^{(1,\text{CI})}]$, the latter as seen in the comoving frame of the bent layer. By definition, in such a frame the ions are at rest and $\hat{\rho}^{(1,\text{CI})}$ corresponds to the deformation of the electronic cloud as seen in the curvilinear frame. Therefore we conclude that the *CI response is a purely electronic effect*.

Regarding the remaining contribution due to the internal relaxation, we have

$$\Delta\varphi_{zz,\alpha\alpha} = -L \frac{\bar{p}_{z,\kappa\rho}^{(1,z)}}{\epsilon_0} \Gamma_{\rho,\alpha\alpha}^{\kappa} + \frac{1}{S\epsilon_0} Z_{\kappa,\rho}^{(z)} L_{\rho z,\beta\beta}^{\kappa} + \frac{1}{2S\epsilon_0} \int_{\Omega} d^3r z^2 \rho_{\kappa\rho}(\mathbf{r}) \Gamma_{\rho,\alpha\alpha}^{\kappa}, \quad (4.28)$$

where the overbar indicates average over the supercell volume. The last integral in the r.h.s. of the above equation can be manipulated by exploiting the relation

$$z^2 = (z - \tau_{\kappa z})^2 + 2(z - \tau_{\kappa z})\tau_{\kappa z} + \tau_{\kappa z}^2, \quad (4.29)$$

with $\tau_{\kappa z}$ the out-of-plane component of the sublattice position, τ_{κ} . By inserting Eq.(4.29) into the integral, one arrives to

$$\begin{aligned} \frac{1}{2S\epsilon_0} \int_{\Omega} d^3r z^2 \rho_{\kappa\rho}(\mathbf{r}) \Gamma_{\rho,\alpha\alpha}^{\kappa} &= \frac{1}{S\epsilon_0} \left[\int_{\Omega} d^3r (z - \tau_{\kappa z}) \rho_{\kappa\rho}(\mathbf{r}) \right] \Gamma_{\rho,\alpha\alpha}^{\kappa} \tau_{\kappa z} \\ &+ \frac{1}{2S\epsilon_0} \Gamma_{\rho,\alpha\alpha}^{\kappa} \left[\int_{\Omega} d^3r (z - \tau_{\kappa z})^2 \rho_{\kappa\rho}(\mathbf{r}) + \tau_{\kappa z}^2 \int_{\Omega} d^3r \rho_{\kappa\rho}(\mathbf{r}) \right]. \end{aligned} \quad (4.30)$$

The last term in the r.h.s. of Eq.(4.30) is zero because of the charge neutrality of the system. The second integral in the r.h.s. corresponds to the centered-atom quadrupole, $Q_{\kappa\rho}^{(zz)}$ (22), and it can be related with the first-order spatial dispersion (along z) of the macroscopic polarization response to a displacement of the atom κ along the direction ρ . (22) The second term then reads as

$$\frac{Q_{\kappa\rho}^{(zz)}}{2S\epsilon_0} \Gamma_{\rho,\alpha\alpha}^{\kappa} = L \frac{\bar{p}_{z,\kappa\rho}^{(1,z)}}{\epsilon_0} \Gamma_{\rho,\alpha\alpha}^{\kappa}. \quad (4.31)$$

Remarkably, such a term exactly cancels out with the first term in the r.h.s. of Eq.(4.28). Finally, the first integral in the r.h.s. of Eq.(4.30) corresponds to the longitudinal Born-charges $Z_{\kappa\rho}^{(z)}$. The contribution due to the internal relaxation of the ions can be therefore recast into a purely *lattice-mediated* (LM) contribution of the form

$$\varphi_{zz,\alpha\alpha}^{\text{LM}} = \frac{1}{S\epsilon_0} Z_{\kappa\rho}^{(z)} \mathcal{L}_{\rho z,\alpha\alpha}^{\kappa}, \quad (4.32)$$

where $\mathcal{L}_{\rho z,\alpha\alpha}^{\kappa}$ is the flexoelectric internal-strain tensor describing the relaxation of the atoms within the isolated suspended slab that is given by (*no* summation over repeated indexes is assumed)

$$\mathcal{L}_{\rho z,\alpha\alpha}^{\kappa} = \Gamma_{\rho,\alpha\alpha}^{\kappa} \tau_{\kappa z} + L_{\rho z,\alpha\alpha}^{\kappa}. \quad (4.33)$$

We therefore conclude that, similarly to the theory of piezoelectricity, the out-of-plane flexoelectric response of a finite system can be split into a purely clamped-ion and lattice-mediated contributions. In chapter 5 we shall see that the same is valid for the in-plane response.

4.5 Computational parameters

Our calculations are performed in the framework of density-functional perturbation theory (38; 39) (DFPT) within the local-density approximation, as implemented in ABINIT (58; 54). Norm-conserving pseudopotentials are generated within Hamann’s approach, (35) by using the “stringent” parameters of PseudoDojo, (59) but neglecting non-linear core corrections. We set a supercell size of $L = 30$ bohr (15.875 Å) and a plane-wave cutoff of 80 Ha; the Brillouin zone is sampled by a Γ -centered $12 \times 12 \times 2$ mesh except for graphene and silicene (a grid of $13 \times 13 \times 2$ points is used in the latter two cases); with respect to these parameters, the calculated flexo-voltages are converged within a tolerance of 0.1% or better (see e.g. Fig. 4.4). Before performing the linear-response calculations, we optimize the atomic positions and cell parameters of the unperturbed systems to a stringent tolerance (10^{-7} and 10^{-5} atomic units for residual stress and forces, respectively); the resulting structures (detailed in Tab. 4.1 and Fig. 4.3) are in excellent agreement with existing literature data (see e.g. Ref. (60) and references therein).

	a (Å)	b (Å)	h (Å)
C	2.443	2.443	0.0000
Si	3.814	3.814	0.215
P	3.267	4.363	1.055
BN	2.473	2.473	0.0000
MoS ₂	3.121	3.121	1.553
WSe ₂	3.246	3.246	1.664
SnS ₂	3.618	3.618	1.468

TABLE 4.1: Equilibrium structural parameters for the unperturbed flat configuration of the materials considered in this work. h corresponds to the thickness of the buckled materials.

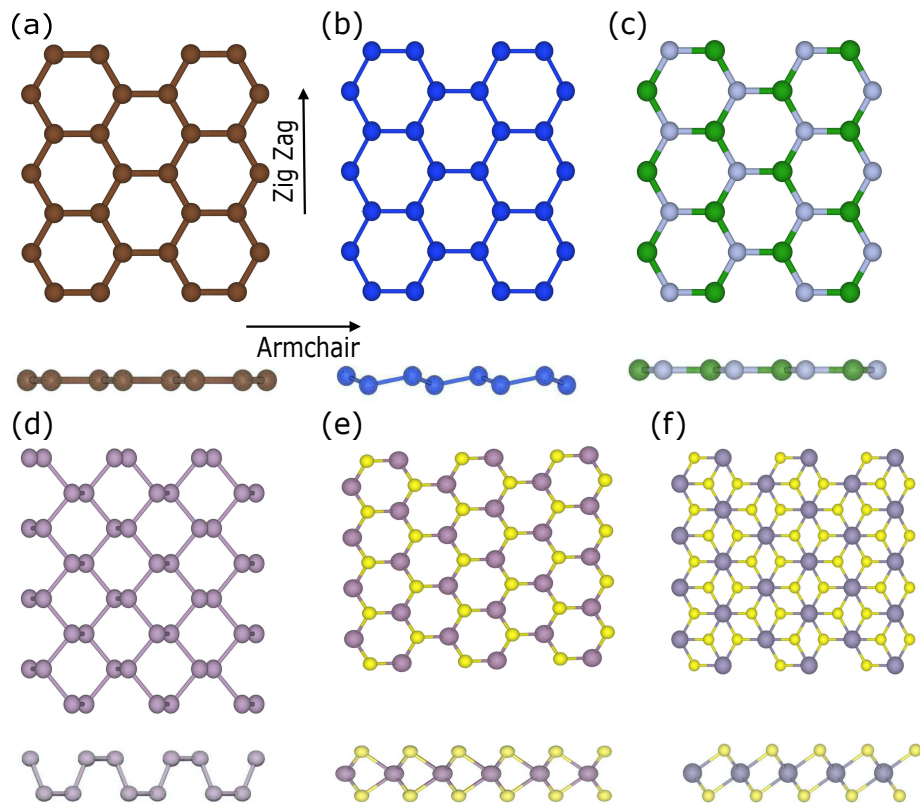


FIGURE 4.3: Top and side view of the crystal structures used in the calculations. (a) graphene, (b) silicene, (c) BN, (d) phosphorene, (e) MoS₂ and (f) SnS₂

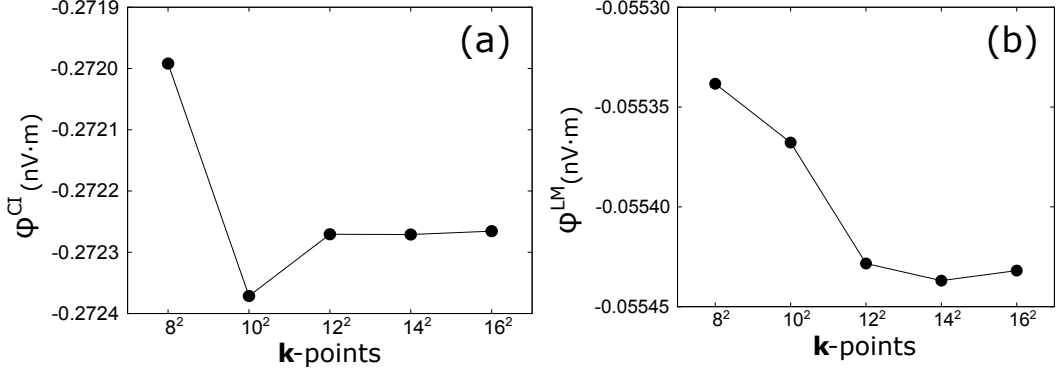


FIGURE 4.4: Convergence of clamped-ion (a) and lattice-mediated (b) MoS₂ flexovoltages as a function of the in-plane \mathbf{k} -points mesh resolution. A plane-wave cutoff of 80 Hartree was employed in the calculations.

4.6 Results

In Table 4.2 we report the calculated bending flexovoltages for several monolayer crystals. The only independent component of the kind $\varphi = \varphi_{xx} = \varphi_{yy}$ is reported, except for phosphorene where two independent components φ_{xx} and φ_{yy} are allowed. Both the CI and LM contributions show a considerable variety in magnitude and sign: while the former dominates in the TMDs, the reverse is true for BN, and SnS₂ seems to lie right in the middle. The case of phosphorene is interesting: its lower symmetry allows for a nonzero φ^{LM} in spite of it being an elemental crystal like C and Si; it also allows for a substantial anisotropy of the response. Within the clamped-ion contribution, our calculations show a nearly complete cancellation between the dipolar and metric contributions to φ , across the whole materials set. In Sec. A.2 we provide the decomposition of the clamped-ion flexovoltage coefficient,

	φ^{CI}	φ^{LM}	φ
C	-0.1134	0.0000	-0.1134
Si	0.0585	0.0000	0.0585
P (zigzag)	0.2320	-0.0151	0.2170
P (armchair)	-0.0130	-0.0461	-0.0591
BN	-0.0381	-0.1628	-0.2009
MoS ₂	-0.2704	-0.0565	-0.3269
WSe ₂	-0.3158	-0.0742	-0.3899
SnS ₂	0.1864	0.1728	0.3592

TABLE 4.2: Clamped-ion (CI), lattice-mediated (LM) and total flexovoltages (nV.m) of the 2D crystals studied in this work. Due to its lower symmetry, for phosphorene two independent bending directions (armchair and zigzag) exist.

cient, φ^{CI} , into the three contributions of Eq.(4.27). This result shows the necessity of considering the metric contribution in order to obtain a proper description of the effect. In Sec. A.2 we also provide further details regarding the analysis of the lattice-mediated contribution.

	t (Å)	φ (nV·m)	μ (pC/m)
Si	3.18	0.0585	1.6273 (7.28 ^a)
C	3.34	−0.1134	−3.0062 (2.86 ^a , 0.4 ^d)
BN	3.85	−0.2009	−4.6202 (0.26 ^a)
P (zigzag)	5.61	0.2170	3.4245 (46 ^b)
P (armchair)	5.61	−0.0591	−0.9327 (84 ^b)
SnS ₂	6.98	0.3592	4.5577
MoS ₂	7.44	−0.3269	−3.8906 (31.94 ^a , −1.82 ^c)
WSe ₂	7.53	−0.3899	−4.5819 (−0.78 ^c)

TABLE 4.3: Interlayer spacing in the bulk (extracted from Ref. (1)), total flexovoltage and volume-averaged flexoelectric coefficient of the 2D crystals studied in this work. Data between round brackets in the third column has been extracted from the literature: ^a Ref. (2),^b Ref. (3), ^c Ref. (4), ^d Ref. (5)

If we assume a physical thickness t corresponding to the bulk interlayer spacing, we obtain an estimate (see Table 4.3) for the volume-averaged flexoelectric coefficients, of $|\mu| = |\mu^{2D}|/t \sim 1 - 5$ pC/m. (μ , unlike μ^{2D} , is inappropriate (61) for 2D layers given the ill-defined nature of the parameter t ; we use it here for comparison purposes only.) This value is in the same ballpark as earlier predictions, (4; 2; 5; 3) although there is a considerable scatter in the latter. For example, the value quoted by Ref. (2) for graphene is very close to ours (in amplitude), but their results for other materials are either much larger (TMD's, silicene) or much smaller (BN); other works tend to disagree both with our results and among themselves. These large discrepancies are likely due to the specific computational methods that were adopted in each case (often the total dipole moment of a bent nanoribbon including the boundaries was calculated, rather than the intrinsic response of the extended layer), or to the aforementioned difficulties (61) with the definition of the dipole of a curved surface.

Very recently Ref. (61) reported first-principles calculations of some of the materials presented here by using methods that bear some similarities to ours, which allows for a more meaningful comparison. By converting our results for Si and C to the units of Ref. (61) via Eq. (4.18), we obtain $\mu_C = -0.0063e$ and $\mu_{Si} = +0.0032e$; these, however, are almost two orders of magnitude smaller, and with inconsistent signs, with respect to the corresponding results of Ref. (61). We ascribe the source of disagreement to the neglect in Ref. (61) of the metric term in Eq. (4.27). Indeed, for the dipolar linear-response contribution [first two terms in Eq. (4.27)] we obtain $\mu_C^{\text{dip}} = -0.22e$ and $\mu_{Si}^{\text{dip}} = -0.19e$, now in excellent agreement (except for the sign) with the results of Codony *et al.*. This observation points to a nearly complete cancellation between the dipolar and metric contribution to φ , which is systematic across the whole materials set (see Table 3 in Supplemental Material of Ref. (56)).

To clarify this point, we consider (Sec. 4.8) a toy model of noninteracting spheres, which illustrates the necessity of including the metric contribution in order to obtain a qualitatively correct physical picture.

4.6.1 Generalized-gradient approximation

In order to check whether the treatment of the exchange and correlation energy has a strong impact on our results, we have recalculated the flexovoltages of Table 4.2 by

	φ^{CI}	φ^{LM}	φ^{tot}
C	-0.1245	0.0000	-0.1245
Si	0.0297	0.0000	0.0297
P (zigzag)	0.2495	-0.0105	0.2390
P (armchair)	0.0372	-0.0311	0.0062
BN	-0.0502	-0.1760	-0.2262
MoS ₂	-0.3301	-0.0395	-0.3696
WSe ₂	-0.3739	-0.0531	-0.4269
SnS ₂	0.1763	0.1467	0.3229

TABLE 4.4: GGA values of the clamped-ion (CI), lattice-mediated (LM) and total flexovoltage (nV·m) coefficients of the 2D crystals studied in this work.

using the PBE (62) formulation of the generalized-gradient approximation (GGA). To perform these calculations, we had to extend our computational methodologies to allow for the treatment of generalized-gradient (GGA) functionals first. In this regard, a flavor of the technical challenges that GGA presents in linear-response problems involving strain can be found in Ref. (63). Our results, reported in Table 4.4, indicate that the deviations from the LDA values are relatively minor, and amount to about 10 % in most cases. Larger relative changes only occur in coefficients that were already small in the first place; examples are silicene, P (armchair), and the CI coefficient of BN.

4.7 Consistency checks

4.7.1 The longitudinal case

As a first consistency check of the formalism presented, it is very useful to consider the longitudinal case, where the results are already known analytically. We have, for the purely electronic response,

$$\varphi^{\text{CI}} = \frac{1}{2\epsilon_0 S} \sum_{\kappa} \tau_{\kappa z}^2 Z_{\kappa\beta}^{(z)}. \quad (4.34)$$

That is, the clamped-ion coefficient corresponds to the second moment of the longitudinal (OC) Born charges. Regarding lattice relaxation, the (OC) piezo internal-strain tensor is trivially written as

$$\Gamma_{\beta,zz}^{\kappa} = -\tau_{\kappa z} \delta_{\beta z}. \quad (4.35)$$

Next, the open-circuit flexoelectric internal-strain tensor is given by

$$L_{\beta z,zz}^{\kappa} = \left(\frac{1}{2} \tau_{\kappa z}^2 + K \right) \delta_{\beta z}, \quad (4.36)$$

where K is an arbitrary constant independent of κ that depends on the specific procedure that was used to construct the pseudoinverse – recall that the latter is not uniquely defined. K in any case has no impact on the induced polarization because of the acoustic sum rule, so we can set it to zero. Finally, we have the corrected

internal-strain tensor of the suspended slab

$$\mathcal{L}_{\beta z, zz}^{\kappa} = -\frac{1}{2}\tau_{\kappa z}^2 \delta_{\beta z}. \quad (4.37)$$

By putting all these results together, we find out that the purely electronic and the lattice-mediated part exactly cancel out, and the result vanishes as it should. Within our formalism, the relaxed-ion longitudinal response is given by (see Ref. (29))

$$\varphi = \underbrace{\frac{L}{\epsilon_0 \epsilon_{zz}} \mu_{zz, zz}^{\Pi}}_{\varphi^G} + \underbrace{\frac{\mathcal{Q}[\rho_{zz}^U]}{2\epsilon_0}}_{\varphi^U} + \underbrace{\frac{\mathcal{Q}[\rho^{(0)}]}{2\epsilon_0}}_{\varphi^M}. \quad (4.38)$$

Notice the different indexes labelling the involved response functions and opposite sign of the geometric term, with respect to Eq.(4.25). We then calculate the longitudinal flexovoltage coefficients by use of this formula. Our numerical results (Table 4.5) are in excellent agreement with the expected results, confirming the consistency of our implementation.

	φ^G	φ^M	φ^U	φ
C	-3.8456	-3.8456	7.6911	0.0000
Si	-3.5106	-3.5106	7.0213	0.0000
P	-6.4059	-6.4059	12.8118	0.0000
BN	-3.5764	-3.5744	7.1484	-0.0024
MoS ₂	-10.2987	-10.2987	20.5975	0.0000
WSe ₂	-12.0632	-12.0630	24.1261	-0.0001
SnS ₂	-8.3634	-8.3647	16.7271	-0.0011

TABLE 4.5: Decomposition of the longitudinal (zz, zz) flexovoltage coefficients, Eq.(4.38).

4.7.2 Nanotube calculations

As a second consistency check, we have performed explicit calculations of BN nanotubes of increasing radius R , and extracted the voltage drop between their interior and exterior, ΔV , at the clamped-ion level. In Figure 4.5 we plot the estimated flexovoltage, given by $R \Delta V$, as a function of R . The asymptotic convergence to the linear-response value of φ^{CI} is clear, consistent with Eq. (4.18). The convergence rate, however, appears rather slow: at the largest value of R , corresponding to a nanotube primitive cell of 128 atoms, the deviation from φ^{CI} is still of about 10%. This result highlights the difficulties at calculating flexovoltages in 2D systems by using the direct approach; conversely, our method provides an optimally converged solution within few minutes on a modern workstation, and is ideally suited, e.g. for high-throughput screening applications.

BN nanotubes are constructed by folding a flat BN sheet via the transformation described in Sec. 4.1.1, with the tube axis oriented along the armchair direction. (These are known in the literature as “zigzag” BN nanotubes.) The resulting structures are then centered in an orthorhombic simulation cell of dimensions $L_y = \sqrt{3}a_0$ and $L_{x,z} = 4R$, with R being the nanotube radius and a_0 the equilibrium lattice constant of the flat monolayer (see Table 4.1). We use the same pseudopotentials as in the linear-response calculations, a plane-wave cutoff of 60 Ha and a $1 \times 4 \times 1$ k -point

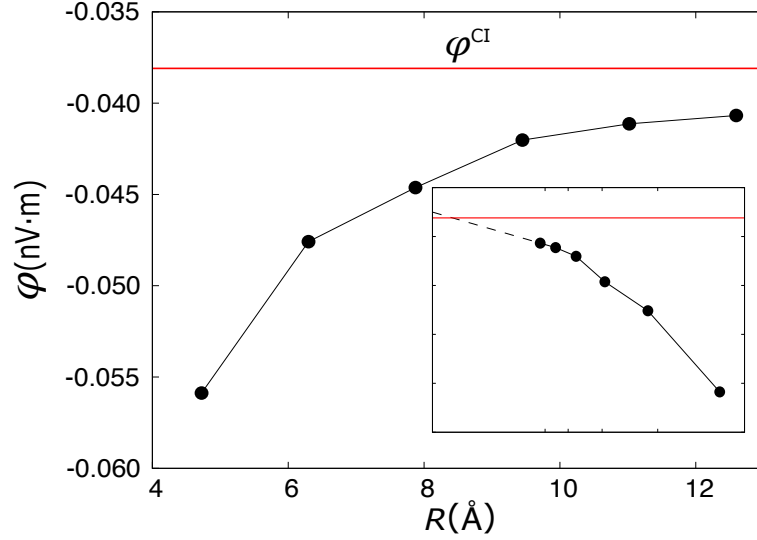


FIGURE 4.5: Clamped-ion flexovoltage coefficient calculated as $\phi = \Delta V R$, plotted as a function of the nanotube radius R . Our linear-response result [Eq. (4.27)] is shown as a red line. The inset shows ϕ as a function of $1/R$, the dashed line being a linear extrapolation from the last two calculated points to $R \rightarrow \infty$.

mesh to sample the Brillouin zone. The flexovoltage is estimated as the voltage drop between the interior and exterior of the tube. In practice, after relaxing the electronic ground state at fixed atomic positions, we average the microscopic electrostatic potential along the tube axis, and extract the values at the center of the nanotube and at the fourfold-coordinated interstitial (equidistant point between four adjacent images).

4.8 An illustrative toy model: Xe monolayer

As a further consistency check, we have considered a toy model, consisting of a hexagonal layer of rare-gas atoms.

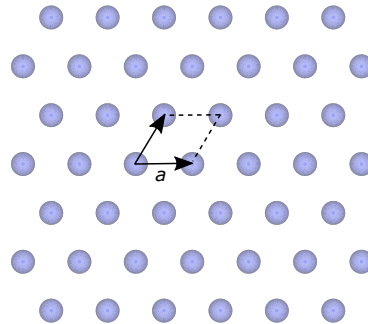


FIGURE 4.6: Crystal structure of the hexagonal Xe monolayer discussed in the text.

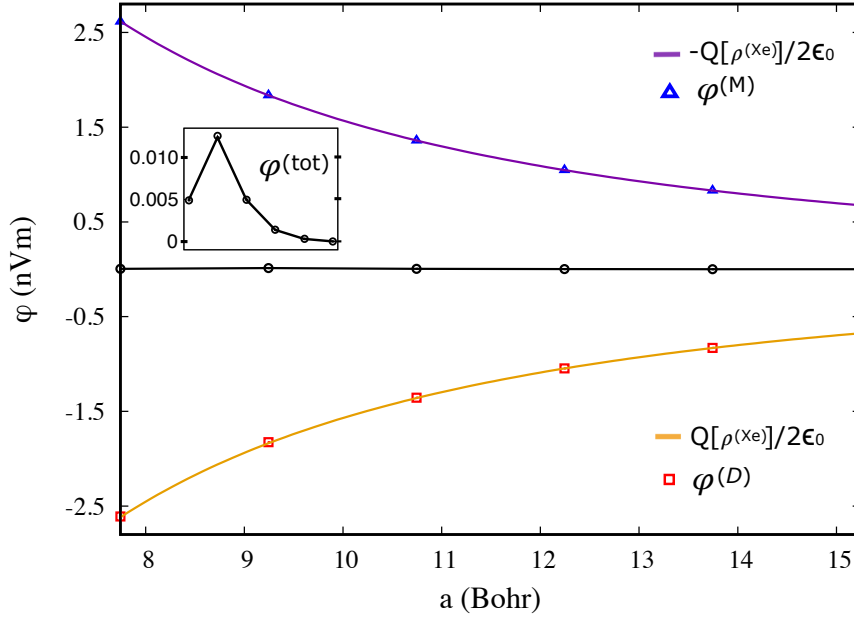


FIGURE 4.7: Computed values for $\varphi^{(M)}$, $\varphi^{(D)}$, $\varphi^{(\text{tot})}$ (nVm) and the analytical curves given by $(\mp Q[\rho^{(\text{Xe})}]/2\epsilon_0)$, as a function of the increasing in-plane lattice constant. $Q[\rho^{(\text{Xe})}]$ is the quadrupolar moment of the isolated atom divided by the unit cell surface $S \propto a^2$. The inset shows the computed values of the “total” flexovoltage, otherwise indistinguishable from zero, being three orders of magnitude smaller than the dipolar and metric terms reported in the figure.

This system is only weakly bonded, and becomes a trivial 2D lattice of noninteracting spherical atoms in the limit of a large lattice parameter. In such a limit, the flexoelectric response must vanish, following the arguments of Ref. (23) and Ref. (29), as the “mechanical deformation” consists in the trivial displacement of noninteracting (and spherically symmetric) neutral atoms. Thus, it provides a test-case where we can benchmark our computational method against an analytically known exact result.

In particular, we shall demonstrate the essential role of the metric term to extract sensible physical conclusions. Fig. 4.7 summarizes the results for φ^{dip} , φ^M and $\varphi^{\text{tot}} = \varphi^{\text{dip}} + \varphi^M$, as a function of the in-plane lattice parameter; note that φ^{dip} consists in the dipole moment of the first-order charge density, and thus coincides with “radial polarization” as defined in Ref. (61).

Clearly, φ^{dip} and φ^M are large in absolute value and opposite in sign. As a result, the “total” flexovoltage $\varphi^{(\text{tot})}$ is always negligibly small, and vanishes exponentially (inset of fig. 4.7) in the limit of large a_0 , consistent with the expectations. (23)

Upon closer inspection, we find that the large absolute values of $\varphi^{\text{dip},M}$ essentially coincide with the quadrupolar moment of $\phi^{\text{Xe}}(\mathbf{r})$, i.e., the spherical charge density of an isolated Xe atom, divided by the cell surface (S),

$$\varphi^{\text{dip},M} \simeq \pm \frac{Q}{2S\epsilon_0}, \quad Q = \int d^3r x^2 \phi^{\text{Xe}}(\mathbf{r}). \quad (4.39)$$

To show this, we calculate Q once and for all as the large- a_0 limit of $-2S\epsilon_0\varphi^M$, and we plot $\pm Q/2S\epsilon_0$ as continuous curves in Fig. 4.7; the matching with the first-principles

data is excellent.

To rationalize this result, it is useful to work out the analytical solution to this problem in the noninteracting (large a_0) limit. The fact that the atoms “do not see each other” implies that the total (electronic and ionic) charge density of the system in both the unperturbed and perturbed configurations is simply a superposition of the spherical atomic densities. This observation explains why the flexovoltage vanishes: each atom remains perfectly spherical, and hence cannot generate a long-range potential no matter how much the “layer” is deformed (i.e., how far the constituent atoms are moved around).

To understand the result of Fig. 4.7 for the individual (dipolar and metric) contributions to the total flexovoltage, we need to solve the same problem in the curvilinear coordinate system that corresponds to the nanotube geometry described in Sec. 4.1.1. The charge density, $\rho(\mathbf{r})$, transforms as a scalar density, which yields the following relation between its curvilinear and Cartesian representation, (29)

$$\rho^{\text{Cart}}(\mathbf{r}') = h^{-1}\hat{\rho}(\mathbf{r}), \quad (4.40)$$

where h is the Jacobian determinant of the coordinate transformation. This is very convenient, as in the curvilinear frame the atoms do not move from their original location, and the charge density $\hat{\rho}(\mathbf{r})$ retains the full translational periodicity of the undeformed 2D crystal. This, however, also implies that an atom that is spherically symmetric in the Cartesian frame is generally no longer spherical in the curvilinear system. In other words, for the noninteracting atoms to retain their spherical ground state in the deformed configuration, *the curvilinear charge density must respond to the deformation in order to compensate for the consequences of the coordinate transformation.* (See Fig. 4.8) This results in an apparent transfer of charge, $\Delta\hat{\rho}$, that does not originate from the local chemistry (and indeed no chemistry is going on in this system), but is simply a mathematical by-product of the coordinate transformation: it can be calculated analytically by inverting Eq. (4.40).

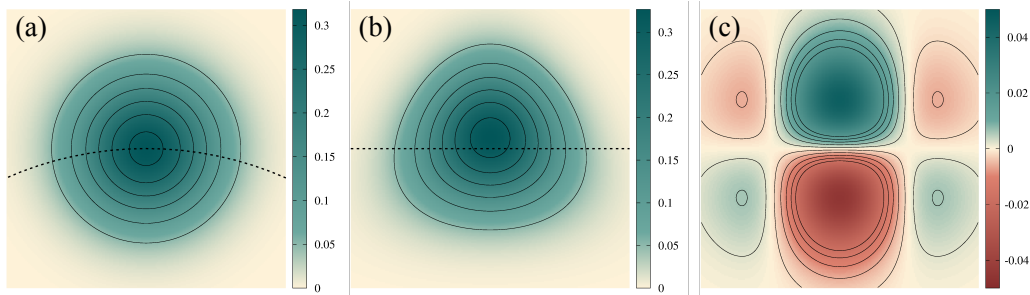


FIGURE 4.8: Impact of curvature on the charge density of a rigid spherical object. For illustration purposes, we use a Gaussian function centered in the origin of the type $\phi(\mathbf{r}) = \frac{1}{\pi\sigma^2}e^{-r^2/\sigma^2}$. (a): Cartesian representation; the dashed curve indicates the curved layer plane. (b): curvilinear $\hat{\rho}(\mathbf{r})$ as defined in Eq. (4.40); the deformation of the original Gaussian is clear. (c): first-order variation of $\hat{\rho}(\mathbf{r})$.

In A.2.3 we provide analytical derivations for $\hat{\rho}$ and its dipolar moment, $\mathcal{D}[\Delta\hat{\rho}]$. We find that $\mathcal{D}[\Delta\hat{\rho}]$ relates to the quadrupolar moment of $\phi^{\text{Xe}}(\mathbf{r})$,

$$\mathcal{D}[\Delta\hat{\rho}] = \frac{Q}{2\epsilon_0 S}, \quad (4.41)$$

thus proving our point.

This result clearly illustrates that φ^{dip} does not correspond to a meaningful physical property of the system: it contains spurious contributions that are mathematical artefacts of the coordinate transformation, and the “metric” term is essential to remove such unphysical terms from φ^{tot} .

4.9 Coupling between out-of-plane electric fields and flexural phonons

The implications of our findings for the interpretation of the experiments are best discussed in terms of the interaction between the flexural modes of a flat layer and an external, generally inhomogeneous, out-of-plane electric field, $\mathcal{E}_z(x, y)$. In full generality, Eq. (4.19) leads to the following coupling (energy per unit area),

$$E_{\text{flexo}}(u_z, \mathcal{E}_z) = \mu^{2\text{D}} \mathcal{E}_z \nabla^2 u_z, \quad (4.42)$$

which reduces to $E_{\text{flexo}} = -q^2 \mu^{2\text{D}} \mathcal{E}_z u_z$ for monochromatic fields of the type $A(x, y) = A \cos(\mathbf{q} \cdot \mathbf{r})$ [$A = (u_z, \mathcal{E}_z)$]. By deriving E_{flexo} with respect to the displacement u_z we obtain the *converse* flexoelectric effect, in the form of a vertical force per unit area, $\mathcal{F}_z = q^2 \mu^{2\text{D}} \mathcal{E}_z$, in response to the field. As shown in the following (section 4.9.3), explicit first-principles calculations of a BN layer under an applied \mathcal{E}_z nicely confirm this prediction: Eq. (4.42) is the main source of out-of-plane electromechanical response in this class of materials. Note that the *longitudinal* out-of-plane flexoelectric coefficient of a free-standing layer, which we extract as a by-product of our main calculations, always vanishes (see section 4.7.1) due to translational invariance and thus cannot contribute to the coupling, contrary to the common belief. (15; 16).

This allows us to generalize the existing models (64) of supported 2D layers by incorporating flexoelectricity, and thereby extract two important messages (that we demonstrate in the following sections). First, the amplitude of the response is highly sensitive to the substrate interaction strength, g , consistent with the results of recent measurements performed on suspended layers. (65) Second, the response displays a strong dispersion in q , indicating a marked sensitivity on the length scale of the inhomogeneities in the applied field. Both outcomes call for a reinterpretation of the existing PFM measurements of flexoelectricity: (15) information about g and the tip geometry appears essential for a quantitative estimation of $\mu^{2\text{D}}$.

4.9.1 Macroscopic electric fields in 2D

So far we have based our formalism on a cylindrical nanotube geometry, with the electrostatics described by the curvilinear-coordinate Poisson equation. While, based on the considerations of Sec. 4.1.2, it is natural to expect that these results are also immediately relevant to flexural deformations of a flat layer, it is not obvious that the long-range electrostatics behaves in the exact same way as in a cylinder. In particular, for a nanotube we only have to worry about the offset between the inner and outer electrostatic potentials, which are both uniform. In a rippled layer, the situation appears much more complex: the “stray” fields generated by the flexoelectric polarization of the layer are strongly nonuniform as they are modulated in plane, and decay exponentially out of plane, generally with a mixed transverse/longitudinal character. Fortunately, Ref. (57) (published at the exact same time as our Ref. (56)) addresses precisely this kind of problems. As we shall see in the following, the same flexovoltage that we derived for the nanotube case has a clear physical significance

also in the flat-flexural case. In particular, it allows to predict/model the stray fields emanating from the layer exactly for an arbitrary ripple pattern, at leading order in the deformation amplitude.

A flexural phonon produces an external charge perturbation of the form

$$\rho^{\text{ext}}(\mathbf{r}) = e^{i\mathbf{q}\cdot\mathbf{r}}\rho^{\mathbf{q}}(z), \quad (4.43)$$

where $\rho^{\mathbf{q}}(z)$ is the planar average of the cell-periodic part. We shall calculate the electrostatic potential at some far-away point from the layer. We shall use the Coulomb kernel as defined in Ref. (57),

$$v(\mathbf{q}, z - z') = \frac{2\pi}{q} e^{-q|z-z'|}, \quad (4.44)$$

The potential can then be written as a convolution in real space,

$$V^{\mathbf{q}}(z) = \int dz' v(\mathbf{q}, z - z') \rho^{\mathbf{q}}(z'). \quad (4.45)$$

If we consider a point in the $z > 0$ plane that is located far enough from the layer that the perturbed density vanishes, the potential is simply given by

$$V^{\mathbf{q}}(z) = \frac{2\pi}{q} \int dz' e^{-q(z-z')} \rho^{\mathbf{q}}(z') = \frac{2\pi}{q} e^{-qz} \int dz' e^{qz'} \rho^{\mathbf{q}}(z'). \quad (4.46)$$

For the $z < 0$ plane we have, similarly,

$$V^{\mathbf{q}}(z) = \frac{2\pi}{q} \int dz' e^{q(z-z')} \rho^{\mathbf{q}}(z') = \frac{2\pi}{q} e^{qz} \int dz' e^{-qz'} \rho^{\mathbf{q}}(z'). \quad (4.47)$$

Now observe that

$$e^{qz} = \cosh(qz) + \sinh(qz), \quad e^{-qz} = \cosh(qz) - \sinh(qz). \quad (4.48)$$

It is then convenient to introduce the following two integrals,

$$\rho^{\parallel}(\mathbf{q}) = \int dz \rho^{\mathbf{q}}(z) \cosh(qz), \quad (4.49)$$

$$\rho^{\perp}(\mathbf{q}) = \int dz \rho^{\mathbf{q}}(z) \sinh(qz). \quad (4.50)$$

Then, we obtain

$$V^{\mathbf{q}}(z > 0) = \frac{2\pi}{q} e^{-q|z|} [\rho^{\parallel}(\mathbf{q}) + \rho^{\perp}(\mathbf{q})], \quad (4.51)$$

$$V^{\mathbf{q}}(z < 0) = \frac{2\pi}{q} e^{-q|z|} [\rho^{\parallel}(\mathbf{q}) - \rho^{\perp}(\mathbf{q})]. \quad (4.52)$$

This provides the formal link between the stray fields in the vacuum region and an arbitrary external charge that is modulated within the layer plane at some wave vector \mathbf{q} . Consistent with the arguments of Ref. (57), the information about the macroscopic electrostatic potentials (i.e. the fields in the vacuum region where the charge density perturbation vanishes) is exactly contained in the two hyperbolic integrals $\rho^{\parallel}(\mathbf{q})$ and $\rho^{\perp}(\mathbf{q})$.

4.9.2 Flexovoltage

To connect with the theory developed above, we need to extract the potential discontinuity near $z = 0$ for the mirror-odd (\sinh) component of the field,

$$V^\perp(\mathbf{q}) = V^q(+\epsilon) - V^q(-\epsilon) = \frac{4\pi}{q}\rho^\perp(\mathbf{q}). \quad (4.53)$$

Based on the arguments of our Ref.(56) (see Supplemental Material, Sec.2.2), at the leading order in q (zero-th and first order terms are zero because of translation and rotational invariance, respectively) we must have $V^\perp(\mathbf{q}) = 4\pi q^2 \mu^{2D} = q^2 \varphi$; this implies

$$\rho^\perp(\mathbf{q})/q = q^2 \mu^{2D} + \dots \quad (4.54)$$

This formula is important, because it expresses the out-of-plane flexoelectric coefficient of the layer as a second derivative of the total energy with respect to two well-defined perturbations: (i) a flexural phonon distortion at some wavevector \mathbf{q} , and (ii) a modulated electric field, described by an externally applied scalar potential of the type

$$V^{\text{ext}}(\mathbf{r}) = -\mathcal{E}_z \frac{\sinh(qz)}{q} \cos(\mathbf{q} \cdot \mathbf{r}). \quad (4.55)$$

This observation guarantees the thermodynamic equivalence between the direct and converse flexoelectric effect, as we shall see in the following subsection. Right on the $z = 0$ plane (i.e., in the strict 2D limit), Eq. (4.55) corresponds to a pure transverse field, modulated by a complex phase. In a neighborhood of the layer, the hyperbolic sine function constitutes the correct (57) generalization of the latter to the quasi-2D case. As a matter of fact, one can show that *any* statically applied potential with mirror-odd symmetry can be expanded on a basis of $\sinh(qz)$ functions times an in-plane phase. This implies that our considerations hold, in full generality, for an arbitrary inhomogeneous field applied out-of-plane.

4.9.3 Converse flexoelectric effect in 2D

As a numerical demonstration of the above results, we have performed an explicit numerical test by applying the external potential of Eq. (4.55) to a suspended monolayer of BN within free electrical boundary conditions. [We have used a $24\sqrt{3} \times 1$ supercell, with similar computational parameters to those that we reported in Sec. 4.5; we have tested two values of $q = 2\pi/(N\sqrt{3}a_0)$, with $N = 12, 24$.] After relaxing the electronic ground state in the external field at fixed atomic positions, we have extracted the out-of-plane atomic forces; their values divided by the field amplitude (we use $\mathcal{E}_z = 10^{-4}$ atomic units) are shown in Fig. 4.9.

The forces display an essentially perfect match with a cosine function, whose amplitude is close to the out-of-plane Born charge of the sublattice,

$$f_\kappa^l = Z_\kappa(\mathbf{q}) \cos(\mathbf{q} \cdot \mathbf{R}_{l\kappa}). \quad (4.56)$$

The values of the fit, reported in Table 4.6, show that the forces on the two sublattices do not cancel exactly; their sum, according to the above arguments, are related to the clamped-ion flexoelectric coefficient, $\bar{\mu}^{2D}$ by

$$\frac{1}{q^2 S} \sum_\kappa f_\kappa \simeq \bar{\mu}^{2D}. \quad (4.57)$$

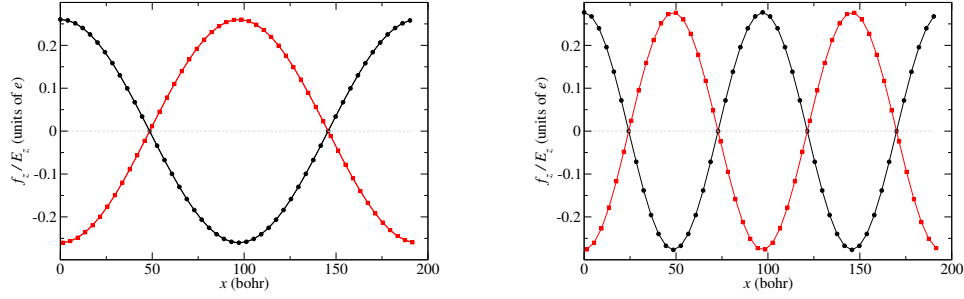


FIGURE 4.9: Atomic forces induced by a spatially modulated transverse electric field on a BN monolayer in its unperturbed equilibrium structure. Modulation periods of 24 (left) and 12 (right) cells are shown. Black circles and red squares refer to B and N atoms, respectively. Solid curves are fits to the data (see text).

The resulting values are in excellent agreement with the direct coupling coefficient calculated via linear-response (see Table 4.2), $\bar{\mu}^{2D} = -0.002105e$, demonstrating the internal consistency of our arguments. Note the relative smallness of the flexoelectric coupling [an $O(q^2)$ effect] compared to the force on the optical “ZO” phonon of the monolayer (given by the difference $Z_B - Z_N$). The restoring force of the flexural phonon, however, goes like $O(q^4)$, which means that the resulting distortions can be very large in the long-wavelength limit, as we shall see in the next subsection.

Period (cells)	Z_B	Z_N	$\sum_{\kappa} Z_{\kappa}$	$\bar{\mu}^{2D}$
12	0.276832	-0.277014	-0.000182	-0.00230
24	0.260273	-0.260315	-0.000042	-0.00212

TABLE 4.6: Explicit calculation of the converse flexoelectric effect. Z_{κ} are the fitted atomic forces in response to the modulated field; $\bar{\mu}^{2D}$ is the estimated clamped-ion flexoelectric coefficient calculated according to Eq. (4.57). All values are in units of electron charge.

4.9.4 Continuum modeling of PFM experiments

The implications of our findings for the interpretation of the experiments are best discussed in terms of the model of Ref. (64), describing the dynamics of the flexural mode of a 2D layer on a substrate. In particular, we propose the following continuum energy functional of the vertical displacement of the layer, $u(x, y)$, and the out-of-plane field, $\mathcal{E}(x, y)$,

$$E(u, \mathcal{E}) = \frac{g}{2} u^2 + \frac{B}{2} (\nabla^2 u)^2 + \mu^{2D} \mathcal{E} \nabla^2 u. \quad (4.58)$$

Here ∇^2 is the in-plane Laplacian operator, g describes the coupling to the substrate (the latter is assumed to be clamped for simplicity), and B is the bending modulus. Of the three parameters appearing in Eq. (4.58), B and μ^{2D} are well-defined *intrinsic* properties of the crystal; g obviously depends on the specifics of the experimental setup.

As an example, in Fig. 4.10 we show a reciprocal-space analysis of the vertical displacement amplitude, which we performed by assuming a cosine-like form for

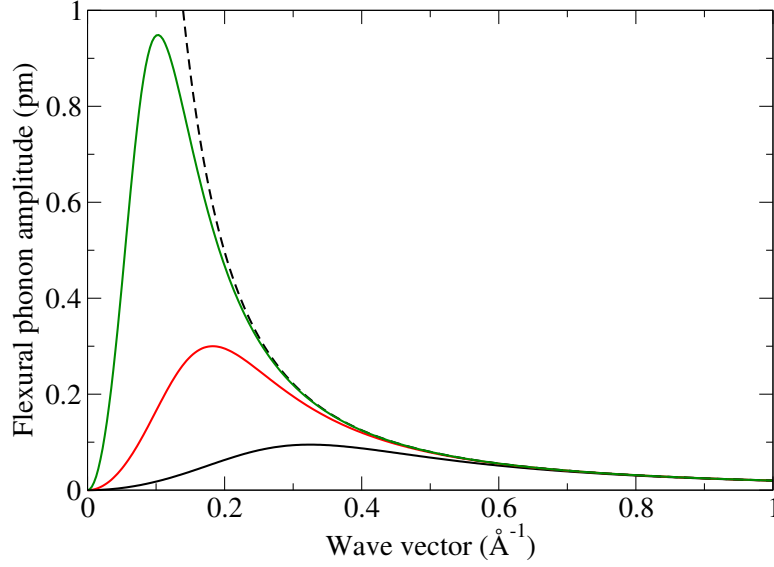


FIGURE 4.10: Amplitude of the flexural phonon response to an externally applied transverse electric field of 1 GV/m, modulated at a given in-plane wavevector q . Results for $g = 10^{-1}$ eV/Å⁴ (black), $g = 10^{-2}$ eV/Å⁴ (red), $g = 10^{-3}$ eV/Å⁴ (green) and the free-standing layer (dashed) are shown.

both functions \mathcal{E} and u . After substituting $f(x) = f \cos(\mathbf{q} \cdot \mathbf{r})$ [$f = \mathcal{E}, u$] in Eq. (4.58) we obtain

$$E(u, \mathcal{E}) = \frac{g + Bq^4}{2} u^2 - \mu^{2D} \mathcal{E} q^2 u, \quad \rightarrow \quad u = \frac{\mu^{2D} \mathcal{E} q^2}{g + Bq^4}, \quad (4.59)$$

where the second equality stems from the stationary condition on E . By using the physical parameters of MoS₂, $\mu^{2D} = -0.018e$ and $B = 9$ eV (66), and four different choices for the substrate interaction parameter, g . (The largest value of $g=0.1$ eV/Å⁴ roughly corresponds to the interlayer coupling in bulk MoS₂; depending on the substrate and deposition technique, the interaction may be one or two orders of magnitude weaker.) The free-standing solution diverges as q^{-2} (a uniform field induces a curvature of $K = \mu^{2D} \mathcal{E} / B$ in such a limit), while in presence of interaction the response peaks at some wavevector q and vanishes in the limit of a uniform field (the vertical force on a layer cell is proportional to $\mu^{2D} \mathcal{E} q^2$). For $g=1$ meV/Å⁴ the peak response of 1 pm/V at a length scale of about 5 nm appears consistent with the measurements of Ref. (15); an experimental estimate of g , together with the Fourier components of the tip potential would be necessary for a more quantitative comparison.

Note that we have neglected dielectric screening effects in our model. This is an excellent approximation for unsupported 2D layers, since the dielectric function tends to unity (57) in the long-wavelength limit that is relevant to our theory. In the supported case, screening by the substrate may be important, but this effect can be easily incorporated in the definition of the external electric field, $\mathcal{E}(x, y)$.

Chapter 5

In-plane response

While the aforementioned out-of-plane response is universal, it turns out to be small in many materials. In the present chapter, we investigate the *in-plane* polarization response to a flexural deformation instead, which we indicate as “unconventional” as it is typically ruled out in 3D crystals of sufficiently high symmetry. The effect, illustrated in Figs. 5.1(a) and 5.1(b), is *linear* in the layer curvature, and therefore differs from the nonlinear one predicted in monolayer h-BN (18) some time ago. It is active in a surprisingly broad class of 2D systems, including many of the best studied materials. Interestingly, for materials with D_{3d} point symmetry (space groups $P\bar{3}m1$ and $P\bar{3}1m$), the amplitude of the polarization response is insensitive to the bending direction, while its orientation continuously rotates in plane, with an angular periodicity that matches the three-fold axis of the flat configuration. [Figs. 5.1(b) and 5.1(c)] Apart from the obvious practical interest for energy-harvesting applications (21), such an effect is important for fundamental reasons as well. Most notably, it leads to a broad range of topologically nontrivial polarization textures in rippled and bent geometries, including vortices/antivortices and spontaneously polarized tubes.

5.1 2D in-plane polarization field

Our goal is to express the flexoelectric coefficients in terms of a “strict-2D” model of the layer, as a *surface polarization* (67) response to curvature. In the truly strict-2D case, the Cartesian components of the surface polarization can be expressed as $\mathbf{P} = (\hat{P}_u \mathbf{r}_u + \hat{P}_v \mathbf{r}_v) / \sqrt{g^{2D}}$, with \mathbf{r}_u , \mathbf{r}_v and g^{2D} defined as provided in 4.1.2, and \hat{P}_α indicating the α component of the *curvilinear* surface polarization. (Similarly to Sec.4.1.2, here we shall use Greek indices for the in-plane uv directions.) The local curvature, in turn, is well described by the matrix elements of the second fundamental form, $b_{\alpha\beta} = \mathbf{r}_{\alpha\beta} \cdot \mathbf{n}$. This, in principle, allows us to write the flexoelectric coefficient in the reference configuration as derivatives of P_α with respect to $b_{\beta\gamma}$.

In the quasi-2D case, as shown in Sec.4.1.2, the matrix elements of \mathbf{b} can be written as follows,

$$b_{\beta\gamma} = -\varepsilon_{\beta\gamma,z}, \quad (5.1)$$

with $\varepsilon_{\beta\gamma,z}$ the symmetrized (type-II) strain-gradient tensor. The latter quantity is uniform along z and is therefore the appropriate macroscopic variable to describe curvature in a quasi-2D context. The strict-2D limit is eventually recovered by integrating along z the microscopic polarization response. Thus, we define the relevant flexoelectric coefficients as first derivatives of the *curvilinear* surface polarization, \hat{P} , with respect to $\varepsilon_{\beta\gamma,z}$,

$$\hat{P}_\alpha = \mu_{\alpha z, \beta\gamma}^{2D} \varepsilon_{\beta\gamma,z}, \quad (5.2)$$

The derivative is intended to be taken within the mixed EBCs, as defined in Sec.4.3. Our choice of notation is motivated by the obvious analogy with the definition of the type-II flexoelectric coefficients in 3D; (22) one should keep in mind, however, that here $\hat{\mathbf{P}}$ is defined as a charge per unit length; consequently, the flexoelectric coefficients $\mu_{\alpha z, \beta \gamma}^{2D}$ have the dimension of a charge.

5.2 Symmetry requirements and D_{3d} crystals

A necessary condition for any of these coefficients to be nonzero is the lack of a z -oriented mirror plane; similarly, xy inversion cannot be a symmetry, as the tensorial dependence on the in-plane indices is odd. While our theory is valid in the most general case, in the following we focus on a subset of these materials that have the highest symmetry compatible with the above criteria. More specifically, we consider crystals with a z -oriented three-fold axis, space inversion symmetry and a vertical mirror plane (space groups $P\bar{3}m1$ and $P\bar{3}1m$, D_{3d} point group). Within this set, there are only three non-zero in-plane components of the type $\mu_{\alpha z, \beta \gamma}^{2D}$. Assuming a zy mirror-plane (x is the armchair direction in $P\bar{3}1m$ crystals, and zigzag in $P\bar{3}m1$), they are related to each other as

$$\mu_{yz,yy}^{2D} = -\mu, \quad \mu_{yz,xx}^{2D} = \mu_{xz,xy}^{2D} = \mu, \quad (5.3)$$

where μ is the only independent component. This choice leaves the freedom for two nonequivalent configurations, related by a $z \rightarrow -z$ mirror operation or, equivalently, by a rotation of $(2n+1)\pi/3$ about the threefold axis. The two structural variants have opposite μ coefficient, which results in a sign ambiguity unless the

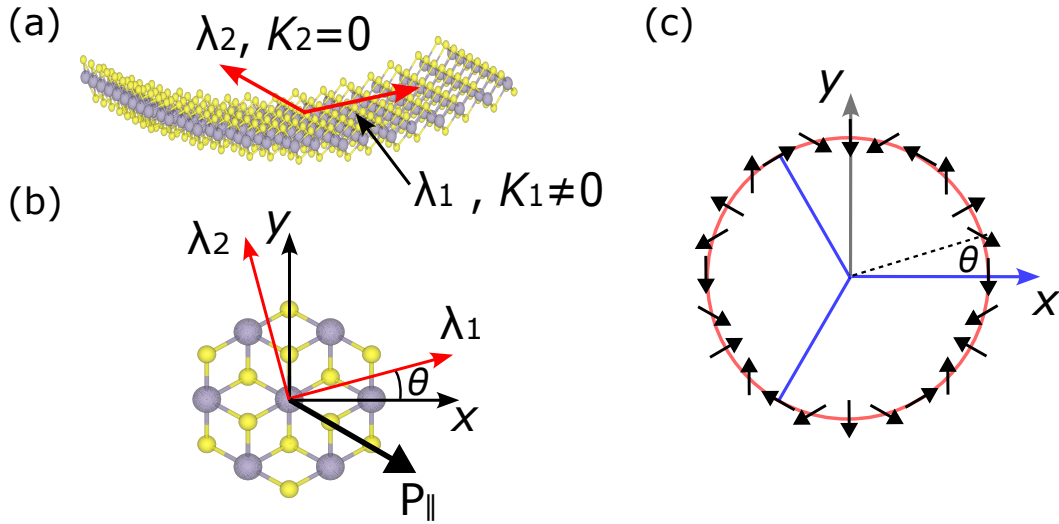


FIGURE 5.1: (a) Schematic illustration of a slab bent along the (principal) direction λ_1 with a (principal) curvature K_1 . Red arrows indicate the principal bending directions. (b) 2D geometry for SnS_2 . θ indicates the angle between the axis x and the principal direction λ_1 . The induced in-plane polarization $P_{||}$ is indicated for an angle $\theta = 15^\circ$. (c) Orientation evolution of the induced in-plane polarization with respect to the bending direction (θ). Threefold symmetry is highlighted by use of blue lines.

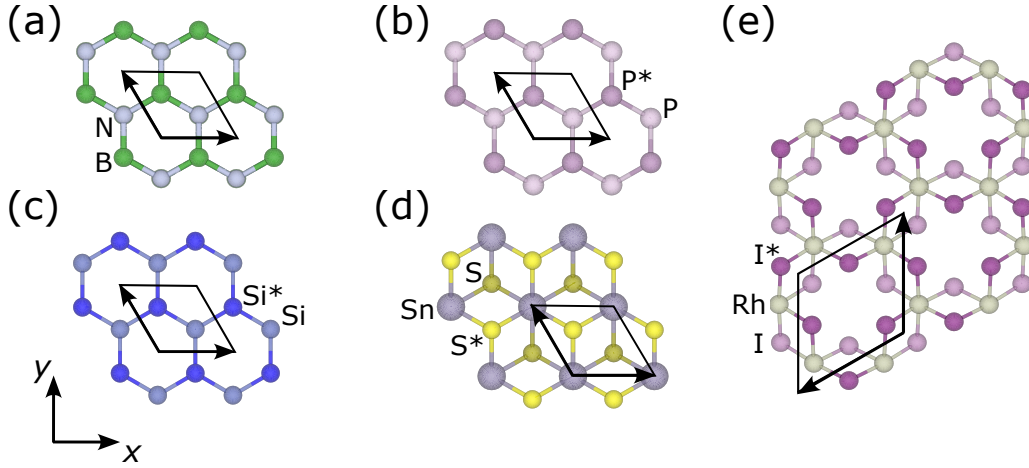


FIGURE 5.2: Top view of the crystal structures employed in the linear-response calculations for the materials considered. The primitive cell is highlighted. Upper and lower atoms of the same type are indicated with the same color but different shade. Upper atoms are explicitly indicated with an asterisk.

atomic positions are fully specified; our data refer to the structures shown in Fig. 5.2 and reported in Table 5.1.

To see the practical implications of Eq. (5.3), it is convenient to represent the strain-gradient components in terms of principal curvatures (K_i) and directions (λ_i) as $\varepsilon_{\beta\gamma,z} = \sum_i K_i \lambda_i^\beta \lambda_i^\gamma$. Then, by writing $\lambda_1 = [\cos(\theta), \sin(\theta)]$ and $\lambda_2 = [-\sin(\theta), \cos(\theta)]$ in terms of the angle θ [Fig. 5.1(b)], we find

$$\hat{P}_{\parallel}(\theta) = \mu (\sin(3\theta)\lambda_1 - \cos(3\theta)\lambda_2) (K_1 - K_2). \quad (5.4)$$

Remarkably, the modulus of the linearly induced polarization is θ -independent, $\hat{P}_{\parallel}(\theta) = |\mu(K_1 - K_2)|$ and only depends on the difference between the principal curvatures. (The case $K_1 = K_2$ corresponds to a deformation with spherical symmetry, which locally preserves the threefold axis of the structure and therefore cannot produce an in-plane \hat{P} .) On the other hand, the polarization direction continuously rotates in plane with an angular periodicity that is three times that of the principal axes. This means that the induced polarization is manifestly invariant with respect to $\theta \rightarrow \theta \pm m2\pi/3$ [Fig. 5.1(c)] with integer m , again consistent with the D_{3d} symmetry of the crystal.

Such a peculiar angular dependence of the polarization response is common to many electromechanical properties of hexagonal layers. For example, an analogous behavior was found in Naumov *et al.* (18) for the polarization induced at the second-order in the curvature in a monolayer of h-BN. Most importantly, Eq. (5.3) matches the internal symmetries of the *piezoelectric* tensor, $e_{\alpha,\beta\gamma}$, in BN and other isostructural materials (e.g., MoS_2) with a z -mirror plane but no space inversion. Indeed for these materials we have

$$e_{y,yy} = -E, \quad e_{y,xx} = e_{x,xy} = E, \quad (5.5)$$

and the induced (piezoelectric) polarization can be written exactly as in Eq. (5.4), provided that we replace the principal curvatures K_i with the principal stretches ε_i and the flexoelectric constant μ with E . This analogy suggests that a flexoelectric effect with the characteristics of Eq. (5.4) should be present in a bilayer of h-BN and

	τ_1	τ_2	τ_3
Si ₁	1/3	2/3	$+h_{\text{Si}}/L$
Si ₂	2/3	1/3	$-h_{\text{Si}}/L$
P ₁	1/3	2/3	$+h_{\text{P}}/L$
P ₂	2/3	1/3	$-h_{\text{P}}/L$
B ₁	1/3	2/3	$+h_{\text{B}}/L$
B ₂	2/3	1/3	$-h_{\text{B}}/L$
N ₁	2/3	1/3	$+h_{\text{N}}/L$
N ₂	1/3	2/3	$-h_{\text{N}}/L$
Sn	0	0	0
S ₁	1/3	2/3	$+h_{\text{SnS}_2}/L$
S ₂	2/3	1/3	$-h_{\text{SnS}_2}/L$
Rh ₁	1/6	5/6	0
Rh ₂	5/6	1/6	0
I ₁	0.148	0.5	$-h_{\text{RhI}_3}/L$
I ₂	0.5	0.852	$+h_{\text{RhI}_3}/L$
I ₃	0.852	0.852	$-h_{\text{RhI}_3}/L$
I ₄	0.148	0.148	$+h_{\text{RhI}_3}/L$
I ₅	0.5	0.148	$-h_{\text{RhI}_3}/L$
I ₆	0.852	0.5	$+h_{\text{RhI}_3}/L$

TABLE 5.1: Primitive-cell atomic structures, expressed in reduced coordinates, for the materials considered in this work. h refers to the parameter reported in Table.5.2, except for BN-bilayer where B and N occupy sublattices positions described by slightly different z-components ($h_{\text{B}} = 3.0661$ Bohr and $h_{\text{N}} = 3.0703$ Bohr for B and N respectively).

related compounds, provided that they are appropriately stacked (AA' or AB') in order to recover D_{3d} symmetry. In this case, within the assumption that the layers do not interact significantly, one expects

$$\mu \simeq Eh, \quad (5.6)$$

where h is the interlayer distance. Eq. (5.6) generalizes the results of Ref. (21) to a generic flexural deformation; here, we shall use it as a validation of our computational method by including the h-BN bilayer in our materials test set.

5.3 First-principles theory

We shall focus now on the first-principles calculation of $\mu_{\alpha z, \beta \gamma}^{2D}$. The microscopic *curvilinear* polarization linear-response along an in-plane (curvilinear) direction ($\alpha = x$ or y) due to a symmetrized uniform strain-gradient of the type $\varepsilon_{\beta \gamma, \lambda}$ is obtained from equations (3.39)-(3.40) and Eq.(3.10). The total (relaxed-ion) 2D longitudinal flexoelectric coefficient is finally obtained as

$$\mu_{\alpha z, \beta \gamma}^{2D} = \frac{1}{S} \int_{\Omega} d^3 r \frac{\partial \hat{P}_{\alpha}(\mathbf{r})}{\partial \varepsilon_{\beta \gamma, z}} = \frac{1}{S} \int_{\Omega} d^3 r P_{\alpha, \beta \gamma}^{(U)}(\mathbf{r}) z + L \mu_{\alpha z, \beta \gamma}^{\Pi} \quad (5.7)$$

where S is the unit-cell surface, L the out-of-plane dimension of the supercell where the layer is accommodated in, and the relation $\mu_{\alpha z, \beta \gamma}^{\Pi} = \frac{1}{\Omega} \int_{\Omega} d^3 r P_{\alpha z, \beta \gamma}^{(G)}(\mathbf{r})$ (22; 29) has been used.

In the following sections we shall recast Eq. (5.7) in a form that is suitable for direct implementation and that, similarly to the out-of-plane response, provides an exact separation between clamped-ion (CI) and lattice-mediated (LM) contributions in the form

$$\mu_{\alpha z, \beta \gamma}^{2D} = \mu_{\alpha z, \beta \gamma}^{2D, CI} + \mu_{\alpha z, \beta \gamma}^{2D, LM} \quad (5.8)$$

5.3.1 Clamped-ion 2D flexocoefficient

The clamped-ion contribution to $\mu_{\alpha z, \beta \gamma}^{2D}$ is formally written as

$$\mu_{\alpha z, \beta \gamma}^{2D, CI} = -\frac{1}{2S} \sum_{\kappa} \int_{\Omega} d^3 r \left(P_{\alpha, \kappa \beta}^{(1, \gamma)}(\mathbf{r}) z + P_{\alpha, \kappa \gamma}^{(1, \beta)}(\mathbf{r}) z \right) + L \mu_{\alpha z, \beta \gamma}^{\Pi, CI}. \quad (5.9)$$

Using the fact that the system is finite along the out-of-plane z -direction, we can write

$$\begin{aligned} -\frac{1}{S} \sum_{\kappa} \int_{\Omega} d^3 r z P_{\alpha, \kappa \beta}^{(1, \gamma)}(\mathbf{r}) &= -\frac{1}{S} \sum_{\kappa} \int_{\Omega} d^3 r (z - \tau_{\kappa z}) P_{\alpha, \kappa \beta}^{(1, \gamma)}(\mathbf{r}) - \frac{1}{S} \sum_{\kappa} \tau_{\kappa z} \int_{\Omega} d^3 r P_{\alpha, \kappa \beta}^{(1, \gamma)}(\mathbf{r}) \\ &= -\frac{1}{S} \sum_{\kappa} \int_{\Omega} d^3 r P_{\alpha, \kappa \beta}^{(2, \gamma z)}(\mathbf{r}) - \frac{1}{S} \sum_{\kappa} \tau_{\kappa z} \int_{\Omega} d^3 r P_{\alpha, \kappa \beta}^{(1, \gamma)}(\mathbf{r}) \\ &= -2L \mu_{\alpha \beta, \gamma z}^{\Pi, CI} - L \sum_{\kappa} \tau_{\kappa z} \bar{P}_{\alpha, \kappa \beta}^{(1, \gamma)}. \end{aligned} \quad (5.10)$$

Here, the overbar indicates average over the supercell volume and we have used the relationship (22) between the type-I CI flexocoefficients and the sublattice summation of $\bar{P}_{\alpha,\kappa\beta}^{(2,\gamma z)}$. Finally, using the relationship $\mu_{\alpha\beta,\gamma z}^I = (1/2) (\mu_{\alpha z,\beta\gamma}^{\text{II}} + \mu_{\alpha\gamma,\beta z}^{\text{II}})$ (29; 22) and gathering all the terms together, Eq.(5.9) can be rewritten as

$$\mu_{\alpha z,\beta\gamma}^{2\text{D,CI}} = -\frac{L}{2} \left[\left(\mu_{\alpha\gamma,z\beta}^{\text{II,CI}} + \mu_{\alpha\beta,z\gamma}^{\text{II,CI}} \right) + \left(\bar{P}_{\alpha,\kappa\gamma}^{(1,\beta)} + \bar{P}_{\alpha,\kappa\beta}^{(1,\gamma)} \right) \tau_{\kappa z} \right]. \quad (5.11)$$

5.3.2 Lattice-mediated 2D flexocoefficient

The remaining non-clamped-ion contributions to the 2D flexocoefficient of Eq. (5.7) are

$$\frac{1}{S} \int_{\Omega} d^3r z P_{\alpha,\kappa\rho}^{(0)}(\mathbf{r}) \Gamma_{\rho,\beta\gamma}^{\kappa} - L \bar{P}_{\alpha,\kappa\rho}^{(1,z)} \Gamma_{\rho,\beta\gamma}^{\kappa} + \frac{1}{S} Z_{\kappa\rho}^{(\alpha)} L_{\rho z,\beta\gamma}^{\kappa}. \quad (5.12)$$

The first term in the above equation can be manipulated, likewise its CI counterpart, as follows

$$\begin{aligned} \frac{1}{S} \int_{\Omega} d^3r z P_{\alpha,\kappa\rho}^{(0)}(\mathbf{r}) \Gamma_{\rho,\beta\gamma}^{\kappa} &= \frac{1}{S} \int_{\Omega} d^3r (z - \tau_{\kappa z}) P_{\alpha,\kappa\rho}^{(0)}(\mathbf{r}) \Gamma_{\rho,\beta\gamma}^{\kappa} + \frac{1}{S} \tau_{\kappa z} \int_{\Omega} d^3r P_{\alpha,\kappa\rho}^{(0)}(\mathbf{r}) \Gamma_{\rho,\beta\gamma}^{\kappa} \\ &= \frac{1}{S} \int_{\Omega} d^3r P_{\alpha,\kappa\rho}^{(1,z)}(\mathbf{r}) \Gamma_{\rho,\beta\gamma}^{\kappa} + \tau_{\kappa z} \frac{1}{S} \int_{\Omega} d^3r P_{\alpha,\kappa\rho}^{(0)}(\mathbf{r}) \Gamma_{\rho,\beta\gamma}^{\kappa} \\ &= L \bar{P}_{\alpha,\kappa\rho}^{(1,z)} \Gamma_{\rho,\beta\gamma}^{\kappa} + \frac{1}{S} Z_{\kappa\rho}^{(\alpha)} \tau_{\kappa z} \Gamma_{\rho,\beta\gamma}^{\kappa}. \end{aligned} \quad (5.13)$$

Now, after observing that the first term at the r.h.s. exactly cancels the mixed one [second term in Eq. (5.12)], we are left with a purely lattice-mediated contribution written, in perfect analogy with the out-of-plane response, as

$$\mu_{\alpha z,\beta\gamma}^{2\text{D,LM}} = \frac{1}{S} Z_{\kappa\rho}^{(\alpha)} \mathcal{L}_{\rho z,\beta\gamma}^{\kappa} \quad (5.14)$$

where $\mathcal{L}_{\rho z,\beta\gamma}^{\kappa}$ is the internal relaxation of the κ -atom in the isolated slab due to the flexural deformation and defined as in Eq.(4.33). Similarly to the out-of-plane response, all ingredients in Eqs. (5.11) and (5.14) can be readily calculated with the linear-response and long-wave (27; 54; 28) modules of ABINIT.

In Sec. B.1 we also prove that the type-II 2D coefficients described here directly relate to the macroscopic 3D coefficients of the supercell in type-I form via $\mu_{\alpha z,\beta\gamma}^{2\text{D}} = -L \mu_{\alpha z,\beta\gamma}^I$, consistent with the known fact (56; 23) that a 2D flexural phonon propagating in a free-standing slab is characterized by the same atomic displacement pattern as a transverse strain gradient.

5.4 Computational results

Our calculations are performed within the local-density approximation as implemented in the ABINIT package (58; 54). Norm-conserving pseudopotentials are generated with Hamann's approach (35), by using the "stringent" parameters of PseudoDojo (59), but neglecting non-linear core corrections. We set a supercell size of $L = 30$ bohr (15.875 Å) and a plane-wave cutoff of 80 Ha; the Brillouin zone is sampled by a Γ -centered $12 \times 12 \times 2$ mesh except for silicene (a grid of $13 \times 13 \times 2$ points is used); with respect to these parameters, the calculated flexocoefficients are converged within a tolerance of 0.1 % or better (see e.g. Fig. 5.3). Before performing

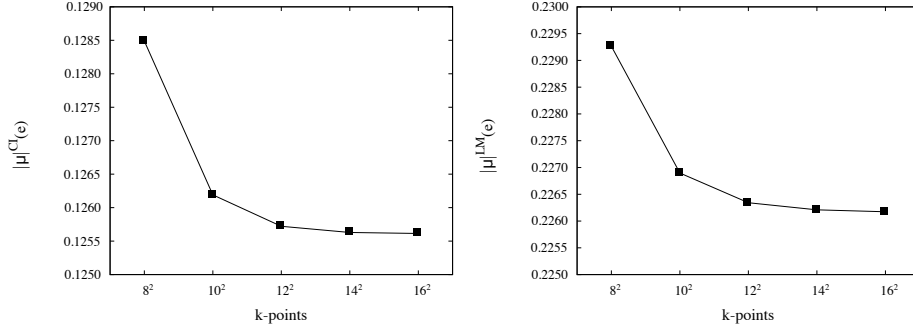


FIGURE 5.3: Convergence of the CI (a) and LM (b) independent component $|\mu|$ as a function of the in-plane \mathbf{k} -points mesh resolution, for SnS_2 .

the linear-response calculations, we optimize the atomic positions and cell parameters of the unperturbed systems to a stringent tolerance (10^{-7} and 10^{-5} atomic units for residual stress and forces, respectively); the resulting structures (detailed in Tab. 5.2) are in excellent agreement with existing literature data (see e.g. Ref. (60) and references therein). In particular, for all the materials considered we used an hexagonal unit-cell described by primitive vectors of the form

$$\begin{aligned} \mathbf{a}_1 &= a \begin{pmatrix} 1.0 & 0.0 & 0.0 \end{pmatrix} \\ \mathbf{a}_2 &= b \begin{pmatrix} -0.5 & \sqrt{3}/2 & 0.0 \end{pmatrix} \\ \mathbf{a}_3 &= c \begin{pmatrix} 0.0 & 0.0 & 1.0 \end{pmatrix} \end{aligned} \quad (5.15)$$

with $a = b$ (see Table 5.2) and $c = L$. The atomic structures of the materials studied in this work are provided in Table 5.1. (In the case of RhI_3 , after having performed the computation with the structure described in Table 5.1, we applied a counter-clockwise rotation of $\pi/2$ to the calculated flexoelectric tensor, in order to recover the geometry shown in Fig. 5.2(e).)

	a (Å)	b (Å)	h (Å)
Si	3.814	3.814	0.215
(blue) P	3.212	3.212	0.619
BN	2.474	2.474	1.625
SnS_2	3.618	3.618	1.468
RhI_3	6.671	6.671	1.488

TABLE 5.2: Equilibrium structural parameters for the unperturbed flat configuration of the materials considered in this work. h corresponds to half the thickness of the buckled materials.

The calculated 2D in-plane flexocoefficients ($\mu_{\alpha z, \beta \gamma}^{2D}$) of silicene, blue phosphorene, SnS_2 and RhI_3 monolayers, as well as of the h-BN bilayer with AA' stacking, are shown in Table 5.3 along with the corresponding out-of-plane ones. [The latter calculated as $\mu_{zz, \beta \beta}^{2D} = \epsilon_0 \varphi_{z, \beta \beta}$, from the flexovoltage φ as defined in chapter 4.] Interestingly, our results indicate that the in-plane flexoelectric response is much larger than the out-of-plane one, in several cases about one order of magnitude larger. This trend is common to all the studied materials in spite of the systematic sign reversal

observed for the CI and LM contributions; both are generally comparable in module, except for RhI_3 where the LM term is one order of magnitude smaller.

	$\mu_{yz,xx}^{2D}$			$\mu_{zz,xx}^{2D}$
	CI	LM	RI	RI
Si	0.0299	0.0000	0.0299	0.0032
BN(bilayer)	0.7569	-0.4947	0.2622	-0.0304
(blue)P	0.0721	0.0000	0.0721	0.0212
SnS_2	0.1257	-0.2263	-0.1006	0.0198
RhI_3	-0.1766	0.0102	-0.1664	-0.0062

TABLE 5.3: Characteristic 2D flexocoefficients due to a flexural deformation. Three left-most columns show the Clamped-Ion(CI), Lattice-Mediated(LM), and Relaxed-Ion(RI) contributions to the in-plane response $\mu_{yz,xx}^{2D}$. Fourth column shows the out-of-plane RI response, $\mu_{zz,xx}^{2D}$. Results are provided in units of electronic charge.

5.4.1 Generalized-gradient and Van der Waals XC functionals

To verify the impact of the exchange-correlation functional, we recalculated the flexoelectric coefficient μ^{2D} defined by using the PBE functional in place of LDA; the results are presented in Table 5.4. The LDA and PBE results show reasonable agreement in most cases, with typical deviations that are in line with the expectations (e.g., similar deviations were pointed out for the out-of-plane response). The largest disagreement occurs in the case of the BN bilayer, with a PBE flexoelectric coefficient that is 35% larger than the LDA value. Interestingly, a closer look at the relaxed PBE structure reveals that the equilibrium interlayer distance, $h_{\text{PBE}} = 8.29$ bohr, displays a comparable (35%) overestimation respect to the LDA result ($h_{\text{LDA}} = 6.14$ bohr). Given that the noninteracting-layer formula, $\mu = Eh$, accurately holds in both cases (compare the “direct” and “model” row in Table 5.4), the large disagreement in the interlayer distance h is almost entirely responsible for the discrepancy in the calculated μ . (The piezoelectric coefficient of monolayer BN, E , has similar values in LDA and PBE.)

Such a discrepancy in the value of h is not surprising, and arises from the fact that a bilayer system is a van der Waals bonded compound, i.e., a classic situation where local and semilocal approximations to DFT fail. PBE, in particular, does not seem to bind the two BN layers at all, which explains the unusually large value of h . This structural parameter has been calculated by taking van der Waals corrections into account, at various levels of theory, in (68). The most reliable values quoted therein, of $h = 3.34 - 3.51$ Å, are similar (3–9% larger) to our LDA value, and 20% smaller than the PBE one. All in all, this analysis indicates that whenever the vdW corrections are needed, the flexoelectric response of the system is trivially given as a weighted sum of the piezoelectric response of the constituents, in agreement with the conclusions of (21).

	$\mu_{yz,xx}^{2D}$			$\mu_{zz,xx}^{2D}$
	CI	LM	RI	RI
Si	0.0239	0.0000	0.0239	0.0016
P	0.0669	0.0000	0.0669	0.0206
SnS ₂	0.1369	-0.2016	-0.0646	0.0178
RhI ₃	-0.1733	0.0202	-0.1530	-0.0080
2-BN (direct)	1.0013	-0.6215	0.3797	-0.0254
2-BN (model)	0.9986	-0.6213	0.3773	

TABLE 5.4: Calculated 2D flexoelectric coefficients within PBE. Left columns show the Clamped-Ion(CI), Lattice-Mediated(LM), and Relaxed-Ion(RI) contributions to the in-plane response $\mu_{yz,xx}^{2D}$. The right column shows the out-of-plane RI response, $\mu_{zz,xx}^{2D}$. Results are provided in units of electronic charge. 2-BN corresponds to the BN bilayer, which we calculated either directly or by means of the piezoelectric model ($\mu^{2D} = Eh$) within PBE. The values of the CI and LM longitudinal piezoelectric constant are $E^{CI} = 0.1208$ e/bohr and $E^{LM} = -0.0749$ e/bohr, respectively, in good agreement with the LDA values reported in the main text. The calculated PBE interlayer distance is $h = 8.29$ bohr.

5.5 Consistency check and comparison with second-order effect

As a first consistency check of our method, we shall prove that we recover Eq. (5.6) and, therefore, the results of Ref. (21) in the case of the h-BN bilayer. To perform this test, we first calculate the value of the piezoelectric constant for an isolated h-BN monolayer, obtaining $E^{CI} = 0.1230$ e/bohr and $E^{LM} = -0.0810$ e/bohr for the CI and LM part, respectively, yielding a total $E = 0.0420$ e/bohr. Then, we relax the geometry of an AA'-stacked bilayer, consistent with the geometry used in Ref. (21), obtaining an interlayer distance of $h = 6.14$ bohr [the experimental bulk spacing is 6.2928 bohr (69)]. By plugging these values into Eq. (5.6) we obtain $\mu^{CI} = 0.7548$ e, $\mu^{LM} = -0.4970$ e and $\mu = 0.2577$ e, in excellent agreement with the results reported in Table 5.3.

To get a flavor of how large the predicted effect is, we can compare it to the nonlinear one described by Naumov *et al.* (18), which involves the in-plane polarization response to the square of the local curvature. Of course, the coefficients are not directly comparable as they occur at different orders in the deformation amplitude; however, we can estimate a critical radius of curvature (R^*) at which the respective magnitudes of the induced polarization become similar. Extracting a second-order coefficient from the numbers provided in Ref. (18) and employing the linear-order coefficient for the h-BN bilayer, we obtain an unrealistically small value of $R^* \sim 0.75$ bohr, with the linear effect prevailing at any $R > R^*$. For instance, Naumov *et al.* obtain induced polarizations $P \sim 0.013$ e/bohr for an h-BN monolayer corrugated along a zigzag direction with an average radius $R \sim 6.7$ bohr and at a CI level. Instead, taking our CI coefficient for the h-BN bilayer [Table 5.3], the present linear effect reaches the same magnitude at curvature radii $R \sim 60$ bohr. At deformation regimes that are currently attainable in a laboratory (70) ($R \sim 10$ μ m), the linear response of the bilayer is stronger than the nonlinear one of the monolayer by five orders of magnitude.

5.6 Topological in-plane polarization in rippled D_{3d} crystals

A direct outcome of the predicted flexoelectric coupling is the emergence of topologically nontrivial in-plane polarization textures in arbitrary rippled states. Let us consider an arbitrary ripple of the form $u_z(x, y)$, that leads to an arbitrary local curvature operator $b_{\beta\gamma}(x, y) = \frac{\partial^2 u_z(x, y)}{\partial r_\beta \partial r_\gamma}$. Following the results of the previous sections, the *macroscopic in-plane* polarization field induced by a generic arbitrary ripple $u_z(x, y)$ of a quasi-2D material can be written as

$$P_\alpha(x, y) = \mu_{\alpha z, \beta\gamma}^{2D} b_{\beta\gamma}(x, y), \quad (5.16)$$

with $\alpha, \beta, \gamma = x$ or y . Remarkably, we find that two-dimensional D_{3d} crystals, when rippled, are endowed with a characteristic nontrivial topological in-plane polarization field (e.g. Fig. 5.4). Indeed, exploiting the symmetries of the 2D flexoelectric

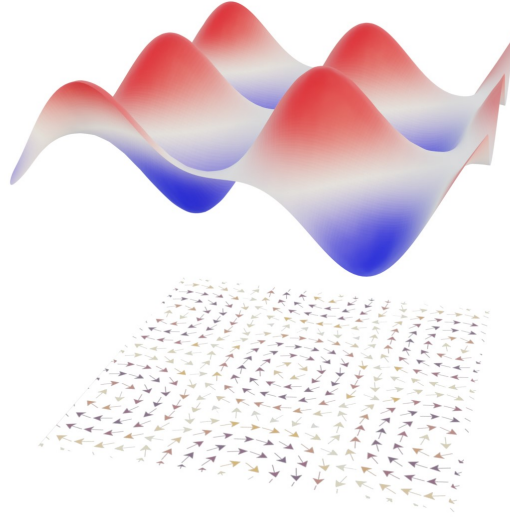


FIGURE 5.4: Rippled surface and the related in-plane polarization induced within the material. The reported ripple corresponds to a superposition of three sinusoidal deformations, as described in the upper side of figure 5.6 (refer to the same figure for color scale details). The induced in-plane polarization field corresponds to an hexagonal lattice of clockwise vortices, each described by a winding number $Q = 1$ and centered in correspondence of the 1D nodes of the ripple (see Fig. 5.6).

coefficients (Eq. 5.3), one finds

$$P_x^{2D}(x, y) = 2\mu^{2D} b_{xy}(x, y), \quad (5.17)$$

$$P_y^{2D}(x, y) = \mu^{2D} (b_{xx}(x, y) - b_{yy}(x, y)), \quad (5.18)$$

with μ^{2D} the only independent entry for the components of the kind $\mu_{\alpha z, \beta\gamma}^{2D}$ (in type-II representation and $\alpha, \beta, \gamma = x$ or y) defined in Eq. (5.3).

The topological state of a two-dimensional order parameter field (in this case the in-plane polarization field) can be described by use of the so-called *winding number* (71), defined as the integer corresponding to the number of turns that the vector field does when moving along a close path defined within the domain the considered field is defined on (the real (x, y) -plane, in this case) and as seen by an observer in

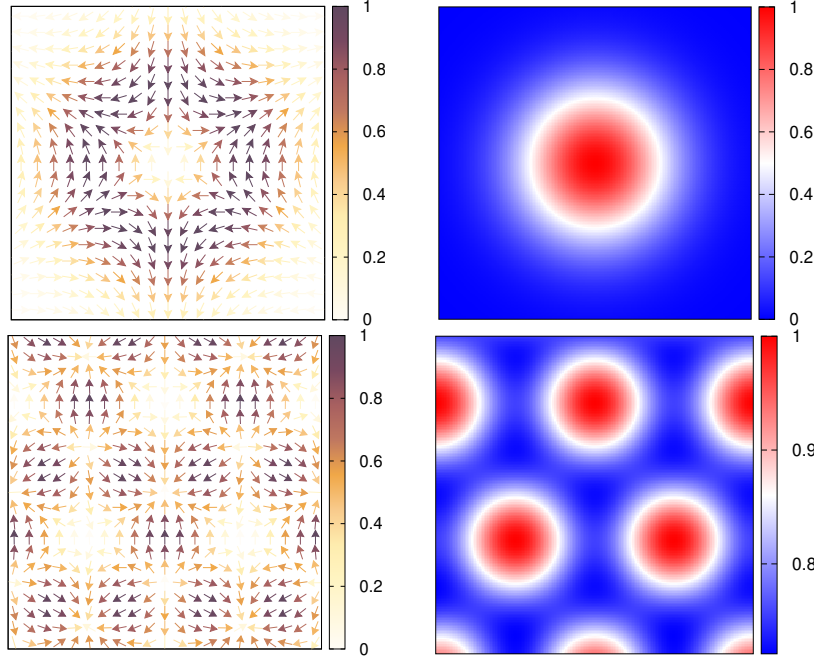


FIGURE 5.5: Top and bottom left panels: Polarization texture associated with a single Gaussian bump of the type $z = Ae^{-(x^2+y^2)/\sigma^2}$ and an hexagonal lattice of Gaussian bumps of the same type. The arrows indicate the polarization direction, its amplitude (in units of $|P_{\parallel}|^{\max} \simeq 1.48 \frac{A\mu}{\sigma^2}$ and $|P_{\parallel}|^{\max} \simeq 6.94 \frac{A\mu}{\sigma^2}$ respectively) is defined by the color scale. Top and bottom right panels: Contour plot for the considered deformation. Their amplitudes (in units of $u_z^{\max} = A$ and $u_z^{\max} \simeq 1.11A$ respectively) are defined by the color scale.

the reference frame. The winding number can be mathematically defined as (71)

$$Q = \frac{1}{2\pi} \oint_{\mathcal{C}} d\mathbf{l} \cdot \frac{d}{d\mathbf{l}} \left(\arctan \left(\frac{P_y^{2D}}{P_x^{2D}} \right) \right). \quad (5.19)$$

where $d\mathbf{l}$ is an infinitesimal line element and \mathcal{C} is the close path defining the line integral.

We consider four different kinds of ripples and show the associated induced in-plane polarization fields, the latter calculated by employing Eq.s (5.17) and (5.18) (see B.2 for mathematical details). In Fig.5.5 we report the in-plane polarization fields that result from an isolated Gaussian-shaped bump and an hexagonal array of Gaussian-shaped bumps respectively. In both cases the resulting polarization field corresponds to a topological figure consisting in a textbook antivortex structure with a topological charge (winding number) $Q = -2$. In Fig.5.6 we consider two periodic deformation patterns with threefold symmetry, both consisting of three superimposed sinusoidal ripples. The two ripples differ by the set of wave-vectors used to describe the three sinusoids. The resulting polarization field is a hexagonal lattice of clockwise and center-divergent vortices ($Q = 1$) respectively. By playing with these two examples we could obtain a whole range of patterns, including an array of monopoles, and in-plane textures that closely resemble those of Ref. (72).

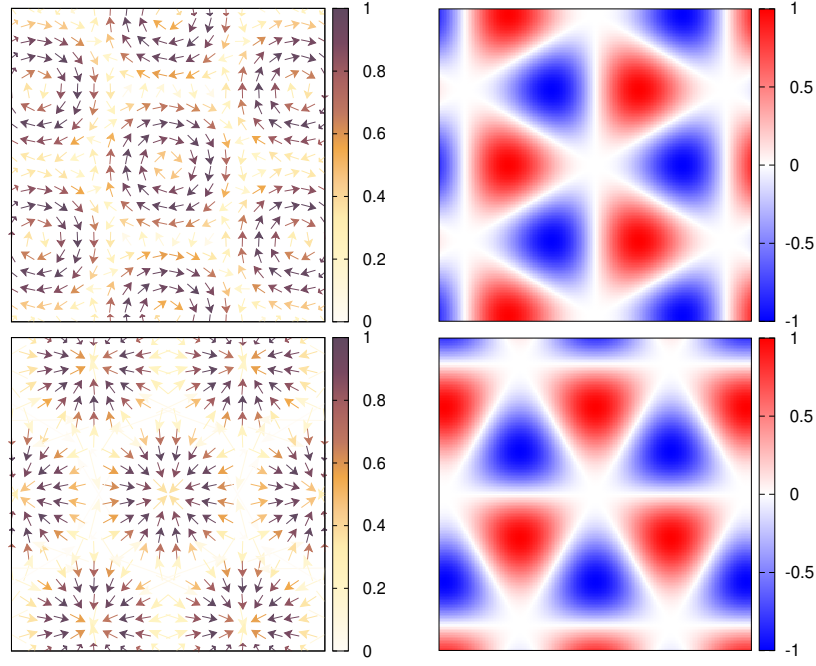


FIGURE 5.6: Top and bottom left panels: Polarization texture associated with two periodic patterns of the type $z = A \sum_{i=1}^3 \sin(\mathbf{q}_i \cdot \mathbf{r})$, with $\mathbf{q}_1 = q(1, 0, 0)$, $\mathbf{q}_2 = q(-1/2, \sqrt{3}/2, 0)$, $\mathbf{q}_3 = q(-1/2, -\sqrt{3}/2, 0)$, and $\mathbf{q}_1 = q(\sqrt{3}/2, 1/2, 0)$, $\mathbf{q}_2 = q(-\sqrt{3}/2, 1/2, 0)$, $\mathbf{q}_3 = q(0, -1, 0)$ respectively. $q = 2\pi/L$. The arrows indicate the polarization direction, its amplitude (in units of $|P_{\parallel}|^{\max} = 1.75A\mu q^2$) is defined by the color scale. Top and bottom right panels: Contour plot of the periodic deformations considered. Their amplitudes (in units of $u_z^{\max} \simeq 2.6A$) are defined by the color scale.

5.7 Spontaneous polarization in D_{3d} crystal nanotubes

As a corollary of the above, our theory predicts an *axial* spontaneous polarization in nanotubes made of 2D trigonal crystals (Fig. 5.7). In particular, a nanotube constructed by folding a layer along λ_1 acquires a linear axial polarization in the form

$$P^{1D} = -2\pi\mu \cos(3\theta), \quad (5.20)$$

independent of its radius, R . Note that, for angles θ that are not an integer multiple of $\pi/6$, a circulating (azimuthal) component of the polarization of amplitude $\mu/R \sin(3\theta)$ coexists with the axial one; the polarization field then becomes chiral.

To test the validity of Eq.(5.20), we performed direct ground-state DFT calculations of zigzag SnS_2 nanotubes and extract the atomic forces, together with the macroscopic electronic polarization along the axial direction via the Berry phase implementation of VASP.5.4 (73; 74; 75; 76). We also performed a full structural relaxation of the nanotube structures to assess the LM contribution to μ , and hence to Eq.(5.20).

Each SnS_2 nanotube is placed in a simulation supercell that is hexagonal over the radial plane, with sufficient outer vacuum regions for the periodic replicas to be mechanically decoupled, and the tube axis is oriented along the z Cartesian direction (with a lattice parameter $c = 11.84$ bohr). We used the projector-augmented wave (PAW) approach with an energy cutoff of 520 eV, the local-density approximation (LDA) to the exchange and correlation potential, and we sampled the first Brillouin

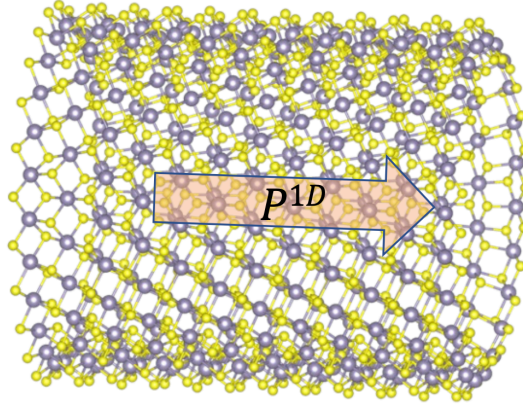


FIGURE 5.7: Nanotube constructed by folding a SnS_2 layer along its zigzag direction. The fully axial spontaneous polarization is schematically sketched.

zone with a grid of $1 \times 1 \times 10$ \mathbf{k} points centered at Γ . The atomic positions are relaxed until all the forces are smaller in magnitude than 2×10^{-4} eV/Å.

In table 5.5 we show the results obtained for two nanotubes generated by folding stripes of 24 and 36 SnS_2 6-atom unit cells. The CI electronic polarization and the atomic forces are in essentially perfect agreement with the linear-response values shown in the bottom row of the table. Such a match is remarkable given the substantial differences in methods and codes between the two calculations. The atomic relaxations show a slightly slower degree of convergence, which we ascribe to the frequency hardening of the contributing polar phonon with curvature (and therefore a physical effect, not a limitation of our method). Note the two orders of magnitude difference between the axial polarization of our SnS_2 nanotubes and the values reported for a bundle of very thin (< 7.5 bohr radius) h-BN nanotubes. (77)

R	$R \cdot F_z^{\text{Sn}}$	$R \cdot F_z^{\text{S}}$	$p^{\text{1D,CI}}$	$p^{\text{1D,LM}}$
26.122	-0.135	0.066	-0.800	1.106
39.183	-0.130	0.066	-0.789	1.304
l.r.	-0.132	0.065	-0.790	1.422

TABLE 5.5: Results from direct calculations for nanotubes of two different radii R [in bohr] (two top rows) and from the linear-response calculation (bottom row). The two left-most columns show the average axial forces [times R and in hartree units] on the Sn and S atoms. The two right-most columns show the clamped-ion and lattice-mediated 1D axial nanotube polarizations [in e]. Direct 1D polarizations are calculated as $\Omega P_z / c$, with Ω , c and P_z being, respectively, the volume, dimension and 3D polarization component along the axial direction of the simulation supercell. In turn, linear response ones are calculated with Eq.(5.20) of the main text.

Chapter 6

Conclusions

An important conceptual breakthrough of this thesis consists in defining flexoelectricity (more specifically, the out-of-plane response) in 2D-materials in terms of the open-circuit voltage in response to curvature. This is a crucial advance in this research area, as it allowed us to overcome once and for all the former difficulties, e.g. with the definition of the dipole moment of a curved slab. The issue, in fact, does not reside that much in the definition of the dipole moment itself (a sound prescription that works in the cylindrical coordinate system of a bent layer was proposed in Ref.(61)), but rather in its physical significance for representing a meaningful physical property of the system. Indeed, curvature modifies the Poisson equation in a non trivial way, which implies that the “radial dipole moment” alone no longer describes the coupling with external potentials: The *quadrupolar* moment of the charge distribution must be accounted for as well. This observation leads to one of our key findings of this thesis: in the linear regime, the radial dipole moment of the induced charge density must be corrected with a *metric* term, consisting in the quadrupolar moment of the unperturbed charge. This way, we obtain a physically sound description of the out-of-plane flexoelectric response, which correctly describes the (both direct and converse) interaction between an arbitrary flexural deformation and the electrostatic potentials outside the layer. Our definition is benchmarked in terms of an intuitive toy model, where we demonstrate the necessity of using our prescriptions to avoid running into an absurdum: if we neglect the metric term, dipole moments would be generated by rigidly displacing neutral spheres in space.

From the point of view of the computational approach, the first-principles methods developed in this thesis constitute a drastic advance compared to the preexisting state of the art. The out-of-plane flexoelectric coefficients have been implemented and calculated as linear-response properties of the material: this has obvious advantages, both in terms of efficiency and accuracy. First, within our strategy the flexoelectric response is calculated on the primitive 2D cell of the flat layer: This completely removes the need for large bent structures (e.g., nanotube geometries) that can be computationally very demanding, and avoids potential contributions from poorly controlled boundary effects, which were an issue in the past. Second, the use of a linear-response approach enables a straightforward control on the numerical quality of the results and their convergence with respect to the standard computational parameters (e.g., Brillouin-zone sampling, and plane-wave cutoff): the same criteria apply as in other linear-response properties (e.g., dielectric constant or elastic tensor), which have been available for decades in the framework of density-functional perturbation theory. (38; 39) Last but not least, the computational tools developed in this thesis have been implemented in the open-source simulation package ABINIT, (54; 78) which is distributed free of charge to the scientific community within the GNU public license; this means that the contributions of this thesis

are immediately (and freely) available to any interested scientist. Note that our computational strategy can be easily adapted to other microscopic models (force fields, etc.): we are confident that our definitions will allow in the future a much easier (and fair) comparison between different levels of description of the material.

The aforementioned conceptual and technical advances are not only academic, but have direct practical implications as well. Indeed, our findings provide an exact representation of the curvature-induced dipole in a form that is ready to be incorporated in a strict-2D model of the real “quasi-2D” material. This is invaluable in the perspective of incorporating our calculated coefficients in macroscopic models of real-life systems, e.g., the typical experimental setups that are used to probe the flexoelectric effect in 2D. Most reported attempts so far are based on the piezoresponse force microscopy (PFM) analysis of supported layers; in this thesis we have outlined a strategy to model precisely this kind of situations. Of special note, we find that knowing both the strength of the coupling to the substrate and the details of the tip geometry are essential for a meaningful estimation of μ^{2D} via PFM techniques. These findings, in combination with the database of reference values for the flexoelectric coefficient of 2D-materials that we provide, establish (for the first time) clear guidelines for the quantitative interpretation of the measurements.

In the second part of this thesis, we have studied the in-plane electrical response to a flexural deformation, which (with some notable exceptions, e.g., Ref.(21) and Ref. (18)) has seldom been considered in the literature. Many of the conceptual and technical issues we had to face in dealing with the out-of-plane response were also present here; and, similarly to that case, we have managed to express the in-plane flexoelectric coefficients as fundamental linear-response properties of the flat layer, represented by its primitive 2D cell. Moreover, the tensorial representation of the effect that naturally emerges from our linear-response formulation allowed us to identify the symmetry requirements for the effect to be present; thereby, we could target a much broader class of materials in our study. (The only known realization was bilayer BN (21) prior to this thesis.) We find that 2D crystals with D_{3d} symmetry are an especially interesting case, in that the in-plane flexoelectric response is described by a single independent coefficient and acquires a topological character.

To illustrate the implications of such finding, we used the calculated coefficients to model the polarization texture of D_{3d} crystals in a variety of rippled configurations. Even the most basic structures, e.g., isolated Gaussian bumps or periodically repeated arrangements thereof, lead to a remarkable variety of topologically non-trivial textures, including vortices and antivortices. These findings establish rippled D_{3d} layers as a promising (and largely unexplored) platform to study topological physics in real materials, paralleling (and possibly complementing) the case of twisted bilayers that was considered earlier in the literature (72). Since ripples and flexural modes are ubiquitous in 2D crystals, we conjecture that these textures may be a rather common occurrence in nature; we hope that our findings will stimulate the experimental efforts at detecting them.

In summary, this thesis provides a complete solution to a well-defined physical problem: defining and calculating the electromechanical response of realistic 2D crystals to an arbitrary flexural deformation. While this is certainly a success, it's far from being the last word on this topic, as there are many avenues left open to exploration. The most obvious limitation of this thesis is the lack of reliable experimental data to compare our predictions with: as we said, we are confident that the theoretical advances achieved here will result in renewed experimental efforts aimed at filling this gap.

From the point of view of the theory, we were unable to establish a general definition of a “2D in-plane polarization”, e.g., in a way that parallels the definition of “2D charge density” that was proposed in Ref.(57). This limitation has prevented us from writing down the *full* 2D flexoelectric tensor in a tensorial form, and we had to deal with different components of the response on a case-by-case basis. Preliminary work towards removing this limitation (and thereby addressing the flexoelectric response to in-plane strain gradients) was initiated in the course of this thesis, but not completed, and hence not included in this document.

Beyond flexoelectricity, note that curvature plays an important role in other contexts as well. An example is flexomagnetism, i.e., the interaction between flexural deformations and the spin degrees of freedom in magnetically ordered crystals. While a pioneering first-principles theory of these effects has appeared recently, (79) it had to rely on large-scale nanotube structures to extract the relevant physical parameters. We speculate that the expertise gained in this thesis may help one recast the latter as linear-response properties of the flat layer, and thereby bring flexomagnetism to the same level of methodological maturity as flexoelectricity; this is yet another promising avenue for future work.

Appendix A

Out-of-plane response

A.1 Clamped-ion and lattice-mediated coefficients

In this Section we shall see how to convert the SC response functions provided by ABINIT into the mixed EBCs ones, the latter defined as provided in Sec. 4.3. Prior to that, we shall briefly recap the definition of the bulk flexoelectric tensor in the framework of linear-response theory. (22)

A.1.1 Bulk flexoelectric tensor in 3D

The bulk flexoelectric tensor can be written as a sum of electronic and lattice-mediated (LM) effects

$$\mu_{\alpha\lambda,\beta\gamma} = \underbrace{\mu_{\alpha\lambda,\beta\gamma}^{\text{el}}}_{\text{electronic}} + \underbrace{\frac{1}{\Omega} Z_{\kappa\rho}^{(\alpha)} \left(\frac{\partial^2 E}{\partial u_{\kappa\rho} \partial u_{\kappa'\sigma}} \right)^{-1} C_{\sigma\lambda,\beta\gamma}^{\kappa'}}_{\text{lattice-mediated}}. \quad (\text{A.1})$$

(κ, κ' run over atomic sublattices, other indices refer to Cartesian directions; summation over repeated indices is implied.) The second term is given by the product of the Born effective charge tensor, $Z_{\kappa\rho}^{(\alpha)}$, the *pseudoinverse* of the zone-center force-constant matrix (the latter is the second derivative of the total energy E with respect to atomic displacements $u_{\kappa\sigma}$), and the flexoelectric force-response tensor, $C_{\sigma\lambda,\beta\gamma}^{\kappa'}$ (atomic forces induced by a strain gradient); Ω is the cell volume. Eq. (A.1) is in all respects analogous to the well-known formula for the static dielectric tensor, (39)

$$\epsilon_{\alpha\lambda} = \underbrace{\epsilon_{\alpha\lambda}^{\text{el}}}_{\text{electronic}} + \underbrace{\frac{1}{\Omega} Z_{\kappa\rho}^{(\alpha)} \left(\frac{\partial^2 E}{\partial u_{\kappa\rho} \partial u_{\kappa'\sigma}} \right)^{-1} Z_{\kappa'\sigma}^{(\lambda)}}_{\text{lattice-mediated}}. \quad (\text{A.2})$$

The electronic and force-response tensors of Eq. (A.1) can be further decomposed into a clamped-ion (indicated by a bar, it must not be confused with a cell average) and a remainder contribution,

$$\mu_{\alpha\lambda,\beta\gamma}^{\text{el}} = \bar{\mu}_{\alpha\lambda,\beta\gamma} - P_{\alpha,\kappa'\rho}^{(1,\lambda)} \Gamma_{\rho\beta\gamma}^{\kappa'} \quad (\text{A.3a})$$

$$C_{\alpha\lambda,\beta\gamma}^{\kappa} = \bar{C}_{\alpha\lambda,\beta\gamma}^{\kappa} + \Phi_{\kappa\alpha,\kappa'\rho}^{(1,\lambda)} \Gamma_{\rho\beta\gamma}^{\kappa'}. \quad (\text{A.3b})$$

Here $\Gamma_{\rho\beta\gamma}^{\kappa'}$ is the piezoelectric internal-strain tensor, describing the atomic displacements induced by a uniform strain; $P_{\alpha,\kappa'\rho}^{(1,\lambda)}$ and $\Phi_{\kappa\alpha,\kappa'\rho}^{(1,\lambda)}$ refer, respectively, to the electronic polarization and atomic forces induced by a gradient of the mode $u_{\kappa'\rho}$ along the Cartesian direction r_λ . The clamped-ion terms in Eq. (A.3) describe the direct effect of a strain gradient on the electronic polarization (A.3a) and atomic forces (A.3b).

The second terms in Eq. (A.3), mediated by the piezoelectric internal strain Γ , reflect the indirect contribution of nonpolar lattice modes that couple linearly to a uniform strain.

The code implementation of the four “new” tensors in Eq. (A.3) relies on an analytic long-wave expansion (27) of the equations governing the linear response of the crystal to a phonon, electric field or “metric-wave” (25) perturbation. As of early 2020, a complete calculation of the bulk flexoelectric tensor including electronic and lattice-mediated effects can be carried out with the latest release of the ABINIT (58) package. The calculation is inexpensive on a modern workstation: It requires significantly less computational resources than a calculation of the phonon band structure.

A.1.2 From SC to mixed-EBCs

In the following we will distinguish the mixed EBCs response functions from their SC counterparts by indicating the former with a tilde. The mixed EBCs version of the relaxed-ion flexoelectric tensor entering in Eq. (4.22) can be obtained as

$$\begin{aligned}\tilde{\mu}_{\beta z, \alpha\alpha} &= \frac{\mu_{\beta z, \alpha\alpha}}{\epsilon_{zz}} \quad \text{if } \beta = z, \\ \tilde{\mu}_{\beta z, \alpha\alpha} &= \mu_{\beta z, \alpha\alpha} \quad \text{if } \beta = x, y.\end{aligned}\tag{A.4}$$

In particular, the relaxed-ion out-of-plane component $\tilde{\mu}_{zz, \alpha\alpha}$ reads as

$$\tilde{\mu}_{zz, \alpha\alpha} = \frac{\mu_{zz, \alpha\alpha}^{\text{el}} + \mu_{zz, \alpha\alpha}^{\text{LM}}}{\epsilon_{zz}^{\text{el}} + \epsilon_{zz}^{\text{LM}}}\tag{A.5}$$

where the macroscopic flexoelectric coefficient and the static dielectric constant of the supercell are defined as in Eq. (A.1) and Eq. (A.2). It is not immediately clear how to recast the fraction as a sum of well-defined electronic and lattice-mediated terms. We shall proceed by constructing $\tilde{\mu}_{zz, \alpha\alpha}$ by imposing the mixed EBCs since the very beginning. More explicitly, one has the same formula Eq. (A.1)

$$\tilde{\mu}_{zz, \alpha\alpha} = \underbrace{\tilde{\mu}_{zz, \alpha\alpha}^{\text{el}}}_{\text{elec.}} + \underbrace{\frac{1}{\Omega} \tilde{Z}_{\kappa\beta}^{(z)} \tilde{\Phi}_{\kappa\beta\kappa'\gamma}^{-1} \tilde{C}_{\gamma z, \alpha\alpha}^{\kappa'}}_{\text{latt.}}\tag{A.6}$$

in terms of the the electronic and lattice-mediated contributions (Φ^{-1} stands for the pseudoinverse), with the only difference that the symbols with a tilde are defined here in mixed EBCs.

To simplify the notation, from now on we shall adopt a bra/ket notation for the components of a given vector v or operator O over the atomic index and displacement direction,

$$\langle \kappa\alpha | v \rangle = v_{\kappa\alpha}, \quad \langle \kappa\alpha | O | \kappa'\beta \rangle = O_{\kappa\alpha, \kappa'\beta}.\tag{A.7}$$

With this convention, Eq. (A.6) reads as

$$\tilde{\mu}_{zz, \alpha\alpha} = \underbrace{\tilde{\mu}_{zz, \alpha\alpha}^{\text{el}}}_{\text{elec.}} + \underbrace{\frac{1}{\Omega} \langle \tilde{Z}^{(z)} | \tilde{\Phi}^{-1} | \tilde{C}_{z, \alpha\alpha} \rangle}_{\text{latt.}}.\tag{A.8}$$

The electronic contribution and the force-response tensor, in turn, are defined analogously to Eq. (A.3) as

$$\tilde{\mu}_{zz,\alpha\alpha}^{\text{el}} = \tilde{\mu}_{zz,\alpha\alpha} - \frac{1}{2} \langle \tilde{Q}^{(zz)} | \Gamma_{\alpha\alpha} \rangle, \quad (\text{A.9a})$$

$$|\tilde{C}_{z,\alpha\alpha}\rangle = |\tilde{\tilde{C}}_{z,\alpha\alpha}\rangle + \tilde{\Phi}^{(1,z)} |\Gamma_{\alpha\alpha}\rangle. \quad (\text{A.9b})$$

Note that the symmetric part of the $P_{\alpha,\kappa\rho}^{(1,\lambda)}$ tensor has the physical meaning of a quadrupolar response to an atomic displacement,

$$Q_{\kappa\rho}^{(\alpha\lambda)} = P_{\alpha,\kappa\rho}^{(1,\lambda)} + P_{\lambda,\kappa\rho}^{(1,\alpha)}, \quad (\text{A.10})$$

where \mathbf{Q} is the dynamical quadrupole tensor (27). Note also the absence of the hat on $\Gamma_{\beta\alpha\alpha}^{\kappa} - \Gamma$ is insensitive to the electrical boundary conditions since we have assumed inversion symmetry with respect to the $z = 0$ plane.

The conversion to mixed EBCs of the purely electronic response functions is trivial, as it only entails a division by the out-of-plane component of the clamped-ion dielectric tensor,

$$\tilde{\mu}_{zz,\alpha\alpha} = \frac{\bar{\mu}_{zz,\alpha\alpha}}{\bar{\epsilon}_{zz}}, \quad (\text{A.11})$$

$$|\tilde{Z}^{(z)}\rangle = \frac{1}{\bar{\epsilon}_{zz}} |Z^{(z)}\rangle, \quad (\text{A.12})$$

$$|\tilde{Q}^{(zz)}\rangle = \frac{1}{\bar{\epsilon}_{zz}} |Q^{(zz)}\rangle. \quad (\text{A.13})$$

The lattice-mediated response relies on several intermediate quantities. First, the pseudoinverse of the zone-center force-constant matrix is given by the Sherman-Morrison formula,

$$\tilde{\Phi}^{-1} = \Phi^{-1} - \frac{4\pi}{\Omega} \frac{\Phi^{-1} |Z^{(z)}\rangle \langle Z^{(z)}| \Phi^{-1}}{\epsilon_{zz}}, \quad (\text{A.14})$$

where

$$\epsilon_{zz} = \bar{\epsilon}_{zz} + \frac{4\pi}{\Omega} \langle Z^{(z)} | \Phi^{-1} | Z^{(z)} \rangle \quad (\text{A.15})$$

is the static dielectric constant along the out-of-plane direction. Next, the clamped-ion force response transforms as

$$|\tilde{\tilde{C}}_{z,\alpha\alpha}\rangle = |\tilde{C}_{z,\alpha\alpha}\rangle - \frac{4\pi \bar{\mu}_{zz,\alpha\alpha}}{\bar{\epsilon}_{zz}} |Z^{(z)}\rangle, \quad (\text{A.16})$$

while the corresponding lattice-mediated part is governed by the nonanalytic behavior of the force-constant matrix at first order in \mathbf{q} [see Supplemental Material of Ref. (80), Eq. (S.9)],

$$\tilde{\Phi}^{(1,z)} = \Phi^{(1,z)} + \frac{4\pi}{\Omega} \frac{|Z^{(z)}\rangle \langle Q^{(zz)}| - |Q^{(zz)}\rangle \langle Z^{(z)}|}{2\bar{\epsilon}_{zz}}. \quad (\text{A.17})$$

By combining Eq. (A.9) and Eqs. (A.16-A.17), we obtain the following result for the total force-response tensor in open circuit,

$$|\tilde{C}_{z,\alpha\alpha}\rangle = |C_{z,\alpha\alpha}\rangle - \frac{4\pi\mu_{zz,\alpha\alpha}^{\text{el}}}{\bar{\epsilon}_{zz}}|Z^{(z)}\rangle, \quad (\text{A.18})$$

It is a tedious but otherwise straightforward exercise to verify that, with the above definitions, the following relation holds,

$$\tilde{\mu}_{zz,\alpha\alpha} = \frac{\mu_{zz,\alpha\alpha}}{\epsilon_{zz}}. \quad (\text{A.19})$$

It is also worth noting that the internal-strain tensor $\tilde{\mathcal{L}}$ of the slab within mixed EBCs, defined in Eq.(4.33), similarly to the 3D tensor \mathbf{L} can be written as

$$\tilde{\mathcal{L}}_{\beta z,\alpha\alpha}^{\kappa} = \tilde{\Phi}_{\kappa\beta,\kappa'\rho} \tilde{C}_{\rho z,\alpha\alpha}^{\kappa'} \quad (\text{A.20})$$

with

$$\tilde{C}_{\beta z,\alpha\alpha}^{\kappa'} = \tilde{\tilde{C}}_{\beta z,\alpha\alpha}^{\kappa} + \Lambda_{\beta\alpha\alpha}^{\kappa} \tau_{\kappa z}. \quad (\text{A.21})$$

Here $\Lambda_{\beta,\alpha\alpha}^{\kappa}$ is the piezoelectric force-response tensor, related to Γ by $\Gamma_{\beta,\alpha\alpha}^{\kappa} = \Phi_{\kappa\beta,\kappa'\rho}^{-1} \Lambda_{\rho,\alpha\alpha}^{\kappa'}$, while $\tilde{\tilde{C}}_{\beta z,\alpha\alpha}^{\kappa}$ is the clamped-ion contribution to the mixed EBCs flexoelectric force-response tensor. It is not difficult to show that the expression

$$\tilde{\mathcal{L}}_{\beta z,\alpha\alpha}^{\kappa} = \tilde{L}_{\beta z,\alpha\alpha}^{\kappa} + \Gamma_{\beta\alpha\alpha}^{\kappa} \tau_{\kappa z}, \quad (\text{A.22})$$

is recast. The derivation of the latter result rests on the definition of $\tilde{\Phi}^{(1,z)}$: Since we are in mixed EBCs and the sample is finite along z , we can write $\tilde{\Phi}^{(1,z)}$ as the first real-space moment of $\tilde{\Phi}^{(0)}$ along z ,

$$\tilde{\Phi}_{\kappa\beta,\kappa'\gamma}^{(1,z)} = \tilde{\Phi}_{\kappa\beta,\kappa'\gamma}^{(0)} (\tau_{\kappa z} - \tau_{\kappa' z}). \quad (\text{A.23})$$

In practical calculations, we use the following procedure.

- First, we use the publicly available implementation of the bulk flexoelectric tensor in ABINIT to calculate the SC clamped-ion polarization ($\bar{\mu}_{zz,\alpha\alpha}$) and force-response ($|\bar{C}_{z,\alpha\alpha}\rangle$) tensors.
- Second, we convert these quantities to mixed EBCs boundary conditions according to the recipes of the earlier paragraphs,

$$\tilde{\mu}_{zz,\alpha\alpha} = \frac{\bar{\mu}_{zz,\alpha\alpha}}{\bar{\epsilon}_{zz}}, \quad (\text{A.24})$$

$$|\tilde{\tilde{C}}_{z,\alpha\alpha}\rangle = |\bar{C}_{z,\alpha\alpha}\rangle - \frac{4\pi\bar{\mu}_{zz,\alpha\alpha}}{\bar{\epsilon}_{zz}}|Z^{(z)}\rangle, \quad (\text{A.25})$$

- Finally, we incorporate the relevant uniform-strain contributions.

A.2 Supplemental results

A.2.1 Analysis of the clamped-ion contribution

We report in Table A.1 our results for the CI flexovoltage according to Eq.(4.27). As we mentioned, the total flexovoltage results from the nearly complete cancellation

of relatively large numbers. The sum of the first two columns of Table A.1 yield the dipole moment of the first-order charge density response to the deformation, φ^{dip} , which corresponds to the “radial polarization” as defined in Ref. (61). φ^{dip} roughly coincides, within few percents, with the quadrupolar moment of the ground-state charge density divided by $2\epsilon_0$, hence the near cancellation with the metric term, φ^{M} . This implies that an exceptional numerical accuracy is needed to compute the CI flexovoltage, $\varphi^{\text{CI}} = \varphi^{\text{dip}} + \varphi^{\text{M}}$, highlighting the advantages of our linear-response formulation.

A.2.2 Analysis of the lattice-mediated contribution

For the compound materials that we have studied in this work, there is a single out-of-plane optical (ZO) mode that produces a net dipole. Such mode consists in the antiphase motion of the cation and anion sublattices, whereas either of them behaves as a rigid unit. This means that, in terms of these two degrees of freedom, the (open-circuit) force-constant matrix reduces to

$$\tilde{\Phi}_{\kappa\kappa'z} = a \begin{pmatrix} 1 & -1 \\ -1 & 1 \end{pmatrix}, \quad (\text{A.26})$$

with a a positive number, quantifying the strength of the restoring force. The reason is that $\tilde{\Phi}_{\kappa\kappa'z}$ must be a 2×2 matrix, and one of its eigenvalues must be zero (translational invariance), the other positive; this leaves only one free parameter.

To calculate φ^{LM} we need the pseudoinverse of this. To this end, we first calculate eigenvalues and eigenvectors,

$$\lambda_1 = 0, \quad v_1 = \frac{1}{\sqrt{2}}(1, 1), \quad (\text{A.27})$$

$$\lambda_2 = 2a, \quad v_2 = \frac{1}{\sqrt{2}}(1, -1). \quad (\text{A.28})$$

We can write then

$$\tilde{\Phi}_{\kappa\kappa'}^{-1} = \frac{1}{4a} \begin{pmatrix} 1 & -1 \\ -1 & 1 \end{pmatrix}, \quad (\text{A.29})$$

	$\frac{L\bar{\mu}_{zz,\alpha\alpha}}{\epsilon_0\bar{\epsilon}_{zz}}$	$\frac{\mathcal{Q}[\bar{\rho}_{\alpha\alpha}^{\text{U}}]}{2\epsilon_0}$	$-\frac{\mathcal{Q}[\rho^{(0)}]}{2\epsilon_0}$	φ^{CI}
C	-2.4658	-1.4932	3.8456	-0.1134
Si	-2.3766	-1.0755	3.5106	+0.0585
P (zigzag)	-5.2371	-0.9364	6.4059	+0.2323
P (armchair)	-5.5274	-0.8915	6.4059	-0.0130
BN	-2.2805	-1.3320	3.5744	-0.0381
MoS ₂	-9.4562	-1.1129	10.2987	-0.2704
WSe ₂	-11.4534	-0.9254	12.0630	-0.3158
SnS ₂	-7.1838	-0.9945	8.3647	+0.1864

TABLE A.1: Decomposition of the clamped-ion flexovoltage coefficient, φ^{CI} , into the three contributions of Eq.(4.27).

	LDA			GGA		
	Z	f	a	Z	f	a
BN	0.2445	-0.1131	0.1620	0.2444	-0.1173	0.1515
MoS ₂	-0.0854	0.3655	0.3323	-0.0701	0.2980	0.3056
WSe ₂	-0.0992	0.4222	0.3134	-0.0805	0.2871	0.2876
SnS ₂	0.3429	0.2291	0.2030	0.3557	0.1794	0.1854

TABLE A.2: Dynamical charge (Z), flexocoupling coefficient (f) and ZO mode stiffness (a) for selected materials (atomic units) calculated with LDA and GGA. The sign of the polar mode eigenvector is set in such a way that the cation moves outwards.

The longitudinal dynamical charges,

$$\tilde{Z}_{\kappa Z}^{(z)} = (Z, -Z), \quad (\text{A.30})$$

and the (OC) flexoelectric force response,

$$\tilde{C}_{zz,\alpha\alpha}^{\kappa} = (f, -f). \quad (\text{A.31})$$

are also governed by a single parameter each. (The sublattice sum of the dynamical charges vanishes due to the acoustic sum rule; moreover, since the crystal is a 2D layer suspended in vacuum, the sum of the flexoforces must vanish.) Thus, the LM flexovoltage is given by

$$\varphi^{\text{LM}} = \frac{1}{\epsilon_0 S} \frac{Zf}{4a} \begin{pmatrix} 1 & -1 \end{pmatrix} \begin{pmatrix} 1 & -1 \\ -1 & 1 \end{pmatrix} \begin{pmatrix} 1 \\ -1 \end{pmatrix} = \frac{1}{\epsilon_0 S} \frac{Zf}{a}, \quad (\text{A.32})$$

Thus, the lattice-mediated effect acquires the intuitive physical meaning of a geometric field distorting the lattice along the ZO mode coordinate by an amount u that is proportional to the coupling f and inversely proportional to the mode stiffness, a . Such displacement, in turn, produces a dipole per unit area that goes like $u \times Z$. Note that the mode stiffness a relates to the ZO phonon frequency ω via $a = m\omega^2$, where m is the reduced mass of the two-body system.

To help understand the lattice-mediated part, we have calculated the physical constants entering Eq.(A.32). From the results reported in Table A.2, one can see that the flexocoupling strength is roughly proportional (in absolute value) to the mode stiffness; this means that in these materials the magnitude of the LM response is largely determined by the dipolar strength of the ZO mode, Z . The sign of the effect, as in the CI response, varies across the tested set. Bending tends to produce an outward force on the cation, except in BN; however, in some TMDs the anomalous sign (81) of the dynamical charges results in a negative LM response in spite of f being positive.

A.2.3 Toy model

The transverse deformation of Sec. 4.1.1 can be described as a displacement of each atom l to a distorted location,

$$\mathbf{R}_l = \mathbf{f}(\mathbf{R}_l^{(0)}), \quad (\text{A.33})$$

where $\mathbf{R}_l^{(0)}$ span the unperturbed 2D Bravais lattice and \mathbf{f} is the mapping of Eq. (4.1b). The fact that the atoms “do not see each other” implies that the total (electronic and ionic) charge density of the system in both the unperturbed and perturbed configurations is simply a superposition of the spherical atomic densities,

$$\rho^{(0)}(\mathbf{r}) = \sum_l \phi^{\text{Xe}}(\mathbf{r} - \mathbf{R}_l^{(0)}), \quad \rho(\mathbf{r}) = \sum_l \phi^{\text{Xe}}(\mathbf{r} - \mathbf{R}_l). \quad (\text{A.34})$$

This observation explains why the flexovoltage vanishes: each atom remains perfectly spherical, and hence cannot generate a long-range potential no matter how much the “layer” is deformed (i.e., how far the constituent atoms are moved around).

To understand the result of Fig. 4.7 for the individual (dipolar and metric) contributions to the total flexovoltage, we need to solve the same problem in the curvilinear coordinate system that corresponds to the nanotube geometry described in Sec. 4.1. $\rho(\mathbf{r})$ transforms as a scalar density, which yields the following relation between its curvilinear and Cartesian representation, (29)

$$\rho^{\text{Cart}}(\mathbf{r}') = h^{-1} \hat{\rho}(\mathbf{r}), \quad (\text{A.35})$$

where h is the Jacobian determinant of the coordinate transformation. This is very convenient, as in the curvilinear frame the atoms do not move from their original location, and the charge density $\hat{\rho}(\mathbf{r})$ retains the full translational periodicity of the undeformed 2D crystal. This, however, also implies that an atom that is spherically symmetric in the Cartesian frame is generally no longer spherical in the curvilinear system. In other words, for the noninteracting atoms to retain their spherical ground state in the deformed configuration, *the curvilinear charge density must respond to the deformation in order to compensate for the consequences of the coordinate transformation*. This results in an apparent transfer of charge, $\Delta\hat{\rho}$, that does not originate from the local chemistry (and indeed no chemistry is going on in this system), but is simply a mathematical by-product of the coordinate transformation: it can be calculated analytically by inverting Eq. (A.35).

Within the regime of small deformations, $\Delta\hat{\rho}(\mathbf{r})$ can be written as (29)

$$\Delta\hat{\rho}(\mathbf{r}) = z\rho_{xx}^{\text{U}}(\mathbf{r}) + \rho_{xx,z}^{\text{G}}(\mathbf{r}), \quad (\text{A.36})$$

where the two functions on the rhs are the microscopic density response to a uniform (U) strain and a strain gradient (G). (22; 23) The latter functions are easy to derive by using Eqs.(90–91) of Ref. (29), in conjunction with Eq. (75) of Ref. (22), and by observing that the charge-density response to the displacement of an isolated atom is given by translational invariance as

$$\frac{\partial \rho(\mathbf{r})}{\partial R_{l\beta}} = \phi_{\beta}^{\text{Xe}}(\mathbf{r} - \mathbf{R}_l), \quad \phi_{\beta}(\mathbf{r}) = -\frac{\partial}{\partial r_{\beta}} \phi^{\text{Xe}}(\mathbf{r}). \quad (\text{A.37})$$

We find

$$\rho_{xx}^{\text{U}} = \rho^{(0)}(\mathbf{r}) - \sum_l (x - X_l) \phi_x(\mathbf{r} - \mathbf{R}_l), \quad (\text{A.38a})$$

$$\rho_{xx,z}^{\text{G}} = \sum_l (x - X_l)(z - Z_l) \phi_x(\mathbf{r} - \mathbf{R}_l) - \frac{1}{2} (x - X_l)^2 \phi_z(\mathbf{r} - \mathbf{R}_l). \quad (\text{A.38b})$$

After few steps of straightforward algebra, we obtain (an illustration is provided in Fig. ??)

$$\Delta\hat{\rho}(\mathbf{r}) = \sum_{\kappa} \xi(\mathbf{r} - \mathbf{R}_{\kappa}), \quad \xi(\mathbf{r}) = z\phi(\mathbf{r}) + \frac{x^2}{2} \frac{\partial\phi(\mathbf{r})}{\partial z}. \quad (\text{A.39})$$

Since $\Delta\hat{\rho}(\mathbf{r})$ retains in-plane periodicity, $\mathcal{D}[\Delta\hat{\rho}]$ reduces to the dipolar moment of $\xi(\mathbf{r})$,

$$\begin{aligned} \mathcal{D}[\Delta\hat{\rho}] &= \frac{1}{S} \int d^3r \, z \xi(\mathbf{r}) \\ &= \frac{1}{S} \int d^3r \left[z^2 \phi(\mathbf{r}) + \frac{x^2}{2} z \frac{\partial\phi(\mathbf{r})}{\partial z} \right] \\ &= \frac{Q}{\epsilon_0 S} - \frac{Q}{2\epsilon_0 S} = \frac{Q}{2\epsilon_0 S}, \end{aligned} \quad (\text{A.40})$$

thus proving por point. (We used the spherical symmetry of $\phi(\mathbf{r})$ and an integration by parts along x .)

Appendix B

In-plane response

B.1 Relation to type-I bulk flexocoefficients

Here we shall demonstrate that the “2D” type-II flexoelectric coefficients derived in Sec. 5.3 directly relate to the macroscopic “3D” type-I flexoelectric coefficients of the supercell through the following relationship

$$\mu_{\alpha z, \beta \gamma}^{2D} = -L \mu_{\alpha z, \beta \gamma}^I. \quad (\text{B.1})$$

Regarding the clamped-ion part, notice that, exploiting the relation $\Gamma_{\alpha, z\beta}^\kappa = \Gamma_{\alpha, \beta z}^\kappa = -\delta_{\alpha\beta} \tau_{\kappa z}$ valid for an isolated slab (the internal-strain tensors are supposed to be calculated within mixed EBCs), Eq.(5.11) can be recast in the form

$$\mu_{\alpha z, \beta \gamma}^{2D, \text{CI}} = -\frac{1}{2} L \left(\mu_{\alpha \gamma, z\beta}^{\text{II, el}} + \mu_{\alpha \beta, z\gamma}^{\text{II, el}} \right), \quad (\text{B.2})$$

with $\mu_{\alpha \gamma, z\beta}^{\text{II, el}}$ being the type-II bulk *electronic* flexoelectric tensor defined as in Ref. (28):

$$\mu_{\alpha \gamma, z\beta}^{\text{II, el}} = \mu_{\alpha \gamma, z\beta}^{\text{II, CI}} - \bar{P}_{\alpha, \kappa \rho}^{(1, \gamma)} \Gamma_{\rho, z\beta}^\kappa \quad (\text{B.3})$$

Regarding the lattice-mediated contribution, notice that in a free-standing layer the shear components of the type-I internal-strain tensor \mathbf{N} (22) and the transverse components of the type-II tensor are related by

$$N_{\rho z, \beta \gamma}^\kappa = -\Gamma_{\rho, \beta \gamma}^\kappa \tau_{\kappa z} - L_{\rho z, \beta \gamma}^\kappa = -\mathcal{L}_{\rho z, \beta \gamma}^\kappa. \quad (\text{B.4})$$

Now, recalling the relationship between the type-I and type-II representations of the flexoelectric tensor (29; 22),

$$\frac{1}{2} \left(\mu_{\alpha \gamma, z\beta}^{\text{II}} + \mu_{\alpha \beta, z\gamma}^{\text{II}} \right) = \mu_{\alpha z, \beta \gamma}^{\text{I}} \quad (\text{B.5})$$

we can conclude that

$$\mu_{\alpha z, \beta \gamma}^{2D, \text{CI}} = -L \mu_{\alpha z, \beta \gamma}^{\text{I, el}}, \quad \mu_{\alpha z, \beta \gamma}^{2D, \text{LM}} = -L \mu_{\alpha z, \beta \gamma}^{\text{I, LM}} \quad (\text{B.6})$$

which proves Eq. (B.1).

B.2 Nontrivial topological examples

Here we provide the mathematical derivations for the topological polarization fields induced by the ripples considered in section 5.6.

B.2.1 Single Gaussian bump

Let us consider a gaussian deformation of the kind

$$u_z(\mathbf{r}) = A \exp\left(-\frac{x^2 + y^2}{\sigma^2}\right), \quad (\text{B.7})$$

with A and σ constants (the center of the Gaussian deformation is assumed to be located in the origin). For the second fundamental form, we find

$$b_{\beta\gamma}(\mathbf{r}) = \left(4\frac{r_\beta r_\gamma}{\sigma^4} - 2\frac{\delta_{\beta\gamma}}{\sigma^2}\right) u_z(\mathbf{r}), \quad (\text{B.8})$$

and then

$$P_x(\mathbf{r}) = \frac{8A\mu}{\sigma^4} xy \exp\left(-\frac{x^2 + y^2}{\sigma^2}\right), \quad (\text{B.9})$$

$$P_y(\mathbf{r}) = \frac{4A\mu}{\sigma^4} (x^2 - y^2) \exp\left(-\frac{x^2 + y^2}{\sigma^2}\right). \quad (\text{B.10})$$

The maximum of the in-plane polarization amplitude field is equal to (see Fig. B.1)

$$|\mathbf{P}_\parallel|^{\max} \simeq 1.476 \frac{A\mu}{\sigma^2}. \quad (\text{B.11})$$

This field corresponds to a specific topological figure, described by a winding number equal to $Q = -2$ (see top panel of Fig. 5.5). In the case of the single Gaussian bump considered here the value of the winding number, that is visually inferred from Fig. 5.5, can be calculated analytically. Indeed, by representing Eqs. B.9 and B.10 in polar coordinates, one finds

$$P_x(r, \theta) = \frac{8A\mu}{\sigma^4} r^2 \cos(\theta) \sin(\theta) \exp\left(-\frac{r^2}{\sigma^2}\right), \quad (\text{B.12})$$

$$P_y(r, \theta) = \frac{4A\mu}{\sigma^4} r^2 (\cos^2(\theta) - \sin^2(\theta)) \exp\left(-\frac{r^2}{\sigma^2}\right). \quad (\text{B.13})$$

By noticing that

$$\cos(\theta) \sin(\theta) = \frac{1}{2} \sin(2\theta), \quad (\text{B.14})$$

$$\cos^2(\theta) - \sin^2(\theta) = \cos(2\theta), \quad (\text{B.15})$$

one arrives to

$$\frac{P_y(r, \theta)}{P_x(r, \theta)} = \frac{\cos(2\theta)}{\sin(2\theta)} = \cot(2\theta). \quad (\text{B.16})$$

Notice that the direction of the polarization is r -independent, as it is clear from Fig. 5.5. It is possible to show that the relation $\cot(2\theta) = \tan(-2\theta - \frac{\pi}{2})$ holds. Inserting this result in Eq. (5.19), employing polar coordinates ($d\mathbf{l} = (dr, d\theta)$) and by integrating on a closed path (no matter which one the chosen path is) one finally arrives to

$$Q = -\frac{1}{2\pi} \int_0^{2\pi} 2d\theta = -2. \quad (\text{B.17})$$

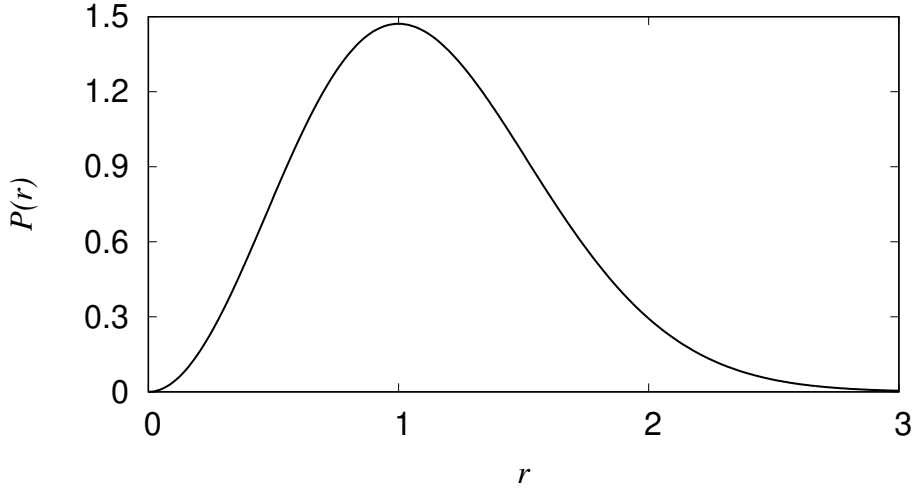


FIGURE B.1: Amplitude of the in-plane polarization field induced by a Gaussian bump, as a function of the radial coordinate and in units of $\frac{A\mu}{\sigma^2}$.

B.2.2 Hexagonal lattice of Gaussian bumps

Here we consider a ripple consisting of a superposition of gaussian-like bumps centered in correspondence with the vectors of an hexagonal lattice of the form

$$\mathbf{R}_l = l_1 \mathbf{a}_1 + l_2 \mathbf{a}_2, \quad (\text{B.18})$$

with l_1, l_2 integers and $\mathbf{a}_1, \mathbf{a}_2$ the primitive vectors describing the structures considered in this work and defined in section 5.4. We also consider each gaussian bump as described by the same amplitude A and the same decay σ . The ripple field is then

$$u_z(\mathbf{r}) = A \sum_l \exp\left(-\frac{|\mathbf{r} - \mathbf{R}_l|^2}{\sigma^2}\right). \quad (\text{B.19})$$

We define $r_{l,\alpha} = r_\alpha - R_{l,\alpha}$ and, analogously to the single Gaussian bump, we find

$$P_x(\mathbf{r}) = \frac{8A\mu}{\sigma^4} \sum_l r_{l,x} r_{l,y} \exp\left(-\frac{r_l^2}{\sigma^2}\right), \quad (\text{B.20})$$

$$P_y(\mathbf{r}) = \frac{4A\mu}{\sigma^4} \sum_l (r_{l,x}^2 - r_{l,y}^2) \exp\left(-\frac{r_l^2}{\sigma^2}\right), \quad (\text{B.21})$$

with r_l the modulo of the vector \mathbf{r}_l . The induced field is described by a winding number equal to $Q = -2$ (see bottom panel Fig.5.5).

B.2.3 Three-phonon perturbation

Let us consider a three-fold symmetric periodic deformation obtained by the superposition of three sinusoidal deformations respectively described by three wave vectors $\mathbf{q}_1, \mathbf{q}_2, \mathbf{q}_3$ having the same modulo q and rotated each other by an angle $\theta = \frac{2\pi}{3}$,

$$u_z(\mathbf{r}) = A(\sin(\mathbf{q}_1 \cdot \mathbf{r}) + \sin(\mathbf{q}_2 \cdot \mathbf{r}) + \sin(\mathbf{q}_3 \cdot \mathbf{r})). \quad (\text{B.22})$$

The second fundamental form is

$$b_{\beta\gamma}(x, y) = -A \sum_i q_{i\beta} q_{i\gamma} \sin(\mathbf{q}_i \cdot \mathbf{r}), \quad (\text{B.23})$$

(here i labels the three wave vectors and Greek indexes indicate their Cartesian components) and then

$$P_\alpha(\mathbf{r}) = -A \mu_{\alpha z, \beta\gamma}^{2D} q_{i\beta} q_{i\gamma} \sin(\mathbf{q}_i \cdot \mathbf{r}), \quad (\text{B.24})$$

where the sum on repeated indices is understood. We shall consider three particular cases, where the set of the three wave vectors describing the considered deformation is progressively rotated by an angle $\pi/3$. We find that the three resulting polarization fields, while different between them, are described by the same topological number.

Case 1

Here we consider three wave vectors of the form

$$\mathbf{q}_1 = q(1, 0), \quad \mathbf{q}_2 = q\left(-\frac{1}{2}, \frac{\sqrt{3}}{2}\right), \quad \mathbf{q}_3 = q\left(-\frac{1}{2}, -\frac{\sqrt{3}}{2}\right). \quad (\text{B.25})$$

The resulting polarization field is

$$P_x(\mathbf{r}) = -\frac{\sqrt{3}}{2} A \mu q^2 (\sin(\mathbf{q}_3 \cdot \mathbf{r}) - \sin(\mathbf{q}_2 \cdot \mathbf{r})), \quad (\text{B.26})$$

$$P_y(\mathbf{r}) = -A \mu q^2 \left(\sin(\mathbf{q}_1 \cdot \mathbf{r}) - \frac{1}{2} (\sin(\mathbf{q}_2 \cdot \mathbf{r}) + \sin(\mathbf{q}_3 \cdot \mathbf{r})) \right). \quad (\text{B.27})$$

We find that the induced polarization field corresponds to a hexagonal lattice of clockwise circulating vortices described a winding number $Q = 1$. (top panel of Fig.5.6)

Case 2

Let us consider three wave vector of the form

$$\mathbf{q}_1 = q\left(\frac{1}{2}, \frac{\sqrt{3}}{2}\right), \quad \mathbf{q}_2 = q(-1, 0), \quad \mathbf{q}_3 = q\left(\frac{1}{2}, -\frac{\sqrt{3}}{2}\right). \quad (\text{B.28})$$

The related polarization field is given by

$$P_x(\mathbf{r}) = -\frac{\sqrt{3}}{2} A \mu q^2 (\sin(\mathbf{q}_1 \cdot \mathbf{r}) - \sin(\mathbf{q}_3 \cdot \mathbf{r})), \quad (\text{B.29})$$

$$P_y(\mathbf{r}) = -A \mu q^2 \left(\sin(\mathbf{q}_2 \cdot \mathbf{r}) - \frac{1}{2} (\sin(\mathbf{q}_1 \cdot \mathbf{r}) + \sin(\mathbf{q}_3 \cdot \mathbf{r})) \right). \quad (\text{B.30})$$

The resulting polarization field corresponds to an hexagonal lattice of counterclockwise vortices with winding number $Q = 1$.

Case 3

Here we consider the following reciprocal space vectors

$$\mathbf{q}_1 = q \left(\frac{\sqrt{3}}{2}, \frac{1}{2} \right), \quad \mathbf{q}_2 = q \left(-\frac{\sqrt{3}}{2}, \frac{1}{2} \right), \quad \mathbf{q}_3 = q (0, -1), \quad (\text{B.31})$$

leading to a polarization field of the form

$$P_x(\mathbf{r}) = -\frac{\sqrt{3}}{2} A \mu q^2 (\sin(\mathbf{q}_1 \cdot \mathbf{r}) - \sin(\mathbf{q}_2 \cdot \mathbf{r})), \quad (\text{B.32})$$

$$P_y(\mathbf{r}) = A \mu q^2 \left(\sin(\mathbf{q}_3 \cdot \mathbf{r}) - \frac{1}{2} (\sin(\mathbf{q}_1 \cdot \mathbf{r}) + \sin(\mathbf{q}_2 \cdot \mathbf{r})) \right). \quad (\text{B.33})$$

The resulting polarization field is shown in the bottom panel of Fig.5.6 and corresponds to an hexagonal lattice of center-divergent vortices with topological charge $Q = 1$.

Bibliography

- [1] A. Jain, S. P. Ong, G. Hautier, W. Chen, W. D. Richards, S. Dacek, S. Cholia, D. Gunter, D. Skinner, G. Ceder and K. A. Persson. *Commentary: The Materials Project: A materials genome approach to accelerating materials innovation*. APL Materials, **1**, 011002 (2013).
- [2] X. Zhuang, B. He, B. Javvaji and H. S. Park. *Intrinsic bending flexoelectric constants in two-dimensional materials*. Phys. Rev. B, **99**, 054105 (2019).
- [3] T. Pandey, L. Covaci, M. V. Milošević and F. M. Peeters. *Flexoelectricity and transport properties of phosphorene nanoribbons under mechanical bending*. Phys. Rev. B, **103**, 235406 (2021).
- [4] W. Shi, Y. Guo, Z. Zhang and W. Guo. *Flexoelectricity in Monolayer Transition Metal Dichalcogenides*. The Journal of Physical Chemistry Letters, **9**, 6841 (2018).
- [5] T. Pandey, L. Covaci and F. Peeters. *Tuning flexoelectricity and electronic properties of zig-zag graphene nanoribbons by functionalization*. Carbon, **171**, 551 (2021).
- [6] T. D. Nguyen, S. Mao, Y.-W. Yeh, P. K. Purohit and M. C. McAlpine. *Nanoscale Flexoelectricity*. Advanced Materials, **25**, 946 (2013).
- [7] L. C. Lew Yan Voon and M. Willatzen. *Electromechanical phenomena in semiconductor nanostructures*. Journal of Applied Physics, **109**, 031101 (2011).
- [8] S.M.Kogan. Sov.Phys.Solid State, **5**, p.2069 (1964).
- [9] E. Bursian and O. Zaikovskii. Sov.Phys.Solid State, **10**, p.1121 (1968).
- [10] L. E. Cross. *Flexoelectric effects: Charge separation in insulating solids subjected to elastic strain gradients*. Journal of materials science, **41**, 53 (2006).
- [11] J. Fousek, L. Cross and D. Litvin. *Possible piezoelectric composites based on the flexoelectric effect*. Materials Letters - MATER LETT, **39**, 287 (1999).
- [12] W. Zhu, J. Y. Fu, N. Li and L. Cross. *Piezoelectric composite based on the enhanced flexoelectric effects*. Applied physics letters, **89** (2006).
- [13] H. Lu, C.-W. Bark, D. Esque De Los Ojos, J. Alcala, C.-B. Eom, G. Catalan and A. Gruverman. *Mechanical writing of ferroelectric polarization*. Science, **336**, 59 (2012).
- [14] L. J. McGilly, A. Kerelsky, N. R. Finney, K. Shapovalov, E.-M. Shih, A. Ghiotto, Y. Zeng, S. L. Moore, W. Wu, Y. Bai, K. Watanabe, T. Taniguchi, M. Stengel, L. Zhou, J. Hone, X. Zhu, D. N. Basov, C. Dean, C. E. Dreyer and A. N. Pasupathy. *Visualization of moiré superlattices*. Nature Nanotechnology, **15**, 580 (2020).
- [15] C. J. Brennan, R. Ghosh, K. Koul, S. K. Banerjee, N. Lu and E. T. Yu. *Out-of-Plane Electromechanical Response of Monolayer Molybdenum Disulfide Measured by Piezoresponse Force Microscopy*. Nano Letters, **17**, 5464 (2017).

- [16] C. J. Brennan, K. Koul, N. Lu and E. T. Yu. *Out-of-plane electromechanical coupling in transition metal dichalcogenides*. *Applied Physics Letters*, **116**, 053101 (2020).
- [17] S. V. Kalinin and V. Meunier. *Electronic flexoelectricity in low-dimensional systems*. *Phys. Rev. B*, **77**, 033403 (2008).
- [18] I. Naumov, A. M. Bratkovsky and V. Ranjan. *Unusual Flexoelectric Effect in Two-Dimensional Noncentrosymmetric sp^2 -Bonded Crystals*. *Phys. Rev. Lett.*, **102**, 217601 (2009).
- [19] W. Shi, Y. Guo, Z. Zhang and W. Guo. *Strain Gradient Mediated Magnetism and Polarization in Monolayer VSe₂*. *J. Phys. Chem. C*, **123**, 24988 (2019).
- [20] B. Javvaji, B. He, X. Zhuang and H. S. Park. *High flexoelectric constants in Janus transition-metal dichalcogenides*. *Phys. Rev. Materials*, **3**, 125402 (2019).
- [21] K.-A. N. Duerloo and E. J. Reed. *Flexural electromechanical coupling: a nanoscale emergent property of boron nitride bilayers*. *Nano letters*, **13**, 1681 (2013).
- [22] M. Stengel. *Flexoelectricity from density-functional perturbation theory*. *Phys. Rev. B*, **88**, 174106 (2013).
- [23] M. Stengel. *Microscopic response to inhomogeneous deformations in curvilinear coordinates*. *Nature Communications*, **4**, 2693 (2013).
- [24] C. E. Dreyer, M. Stengel and D. Vanderbilt. *Current-density implementation for calculating flexoelectric coefficients*. *Phys. Rev. B*, **98**, 075153 (2018).
- [25] A. Schiaffino, C. E. Dreyer, D. Vanderbilt and M. Stengel. *Metric wave approach to flexoelectricity within density functional perturbation theory*. *Phys. Rev. B*, **99**, 085107 (2019).
- [26] M. Stengel. *Surface control of flexoelectricity*. *Phys. Rev. B*, **90**, 201112 (2014).
- [27] M. Royo and M. Stengel. *First-Principles Theory of Spatial Dispersion: Dynamical Quadrupoles and Flexoelectricity*. *Phys. Rev. X*, **9**, 021050 (2019).
- [28] M. Royo and M. Stengel. *Lattice-mediated bulk flexoelectricity from first principles*. *Phys. Rev. B*, **105**, 064101 (2022).
- [29] M. Stengel and D. Vanderbilt. *First-principles theory of flexoelectricity*. A. K. Tagantsev and P. V. Yudin (editors), *Flexoelectricity in Solids From Theory to Applications*, chapter 2, 31–110. World Scientific Publishing Co., Singapore (2016).
- [30] P. Hohenberg and W. Kohn. *Inhomogeneous Electron Gas*. *Phys. Rev.*, **136**, B864 (1964).
- [31] W. Kohn and L. J. Sham. *Self-Consistent Equations Including Exchange and Correlation Effects*. *Phys. Rev.*, **140**, A1133 (1965).
- [32] M. Born and R. Oppenheimer. *Zur Quantentheorie der Molekeln*. *Annalen der Physik*, **389**, 457 (1927).
- [33] D. Vanderbilt. *Soft self-consistent pseudopotentials in a generalized eigenvalue formalism*. *Phys. Rev. B*, **41**, 7892 (1990).
- [34] P. E. Blöchl. *Projector augmented-wave method*. *Phys. Rev. B*, **50**, 17953 (1994).

- [35] D. R. Hamann. *Optimized norm-conserving Vanderbilt pseudopotentials*. Phys. Rev. B, **88**, 085117 (2013).
- [36] X. Gonze. *Adiabatic density-functional perturbation theory*. Phys. Rev. A, **52**, 1096 (1995).
- [37] X. Gonze. *First-principles responses of solids to atomic displacements and homogeneous electric fields: Implementation of a conjugate-gradient algorithm*. Phys. Rev. B, **55**, 10337 (1997).
- [38] S. Baroni, S. de Gironcoli and A. D. Corso. *Phonons and related crystal properties from density-functional perturbation theory*. Rev. Mod. Phys., **73**, 515 (2001).
- [39] X. Gonze and C. Lee. *Dynamical matrices, Born effective charges, dielectric permittivity tensors, and interatomic force constants from density-functional perturbation theory*. Phys. Rev. B, **55**, 10355 (1997).
- [40] D. R. Hamann, X. Wu, K. M. Rabe and D. Vanderbilt. *Metric tensor formulation of strain in density-functional perturbation theory*. Phys. Rev. B, **71**, 035117 (2005).
- [41] M. Stengel and D. Vanderbilt. *Quantum theory of mechanical deformations*. Phys. Rev. B, **98**, 125133 (2018).
- [42] J. J. Sakurai and J. Napolitano. *Modern quantum mechanics; 2nd ed.* Addison-Wesley, San Francisco, CA (2011).
- [43] A. Zabalo and M. Stengel. *Natural Optical Activity from Density-Functional Perturbation Theory*. Phys. Rev. Lett., **131**, 086902 (2023).
- [44] A. Zabalo, C. E. Dreyer and M. Stengel. *Rotational g factors and Lorentz forces of molecules and solids from density functional perturbation theory*. Phys. Rev. B, **105**, 094305 (2022).
- [45] A. K. Tagantsev. *Piezoelectricity and flexoelectricity in crystalline dielectrics*. Phys. Rev. B, **34**, 5883 (1986).
- [46] M. Born and K. Huang. *Dynamical Theory of Crystal Lattices*. International series of monographs on physics. Clarendon Press (1988).
- [47] R. Resta. *Towards a Bulk Theory of Flexoelectricity*. Phys. Rev. Lett., **105**, 127601 (2010).
- [48] R. M. Martin. *Piezoelectricity*. Phys. Rev. B, **5**, 1607 (1972).
- [49] J. Hong and D. Vanderbilt. *First-principles theory of frozen-ion flexoelectricity*. Phys. Rev. B, **84**, 180101 (2011).
- [50] J. Narvaez, S. Saremi, J. Hong, M. Stengel and G. Catalan. *Large Flexoelectric Anisotropy in Paraelectric Barium Titanate*. Phys. Rev. Lett., **115**, 037601 (2015).
- [51] J. Hong and D. Vanderbilt. *First-principles theory and calculation of flexoelectricity*. Phys. Rev. B, **88**, 174107 (2013).
- [52] M. Stengel. *From flexoelectricity to absolute deformation potentials: The case of SrTiO₃*. Phys. Rev. B, **92**, 205115 (2015).
- [53] A. K. Tagantsev and A. S. Yurkov. *Flexoelectric effect in finite samples*. Journal of Applied Physics, **112**, 044103 (2012).

- [54] A. H. Romero, D. C. Allan, B. Amadon, G. Antonius, T. Applencourt, L. Baguet, J. Bieder, F. Bottin, J. Bouchet, E. Bousquet, F. Bruneval, G. Brunin, D. Caliste, M. Côté, J. Denier, C. Dreyer, P. Ghosez, M. Giantomassi, Y. Gillet, O. Gingras, D. R. Hamann, G. Hautier, F. Jollet, G. Jomard, A. Martin, H. P. C. Miranda, F. Naccarato, G. Petretto, N. A. Pike, V. Planes, S. Prokhorenko, T. Rangel, F. Ricci, G.-M. Rignanese, M. Royo, M. Stengel, M. Torrent, M. J. van Setten, B. Van Troeye, M. J. Verstraete, J. Wiktor, J. W. Zwanziger and X. Gonze. *ABINIT: Overview and focus on selected capabilities*. The Journal of Chemical Physics, **152**, 124102 (2020).
- [55] M. P. Do Carmo. *Differential geometry of curves and surfaces: revised and updated second edition*. Courier Dover Publications (2016).
- [56] M. Springolo, M. Royo and M. Stengel. *Direct and converse flexoelectricity in two-dimensional materials*. Phys. Rev. Lett., **127**, 216801 (2021).
- [57] M. Royo and M. Stengel. *Exact Long-Range Dielectric Screening and Interatomic Force Constants in Quasi-Two-Dimensional Crystals*. Phys. Rev. X, **11** (2021).
- [58] X. Gonze, B. Amadon, P.-M. Anglade, J.-M. Beuken, F. Bottin, P. Boulanger, F. Bruneval, D. Caliste, R. Caracas, M. Côté, T. Deutsch, L. Genovese, P. Ghosez, M. Giantomassi, S. Goedecker, D. Hamann, P. Hermet, F. Jollet, G. Jomard, S. Leroux, M. Mancini, S. Mazevet, M. Oliveira, G. Onida, Y. Pouillon, T. Rangel, G.-M. Rignanese, D. Sangalli, R. Shaltaf, M. Torrent, M. Verstraete, G. Zerah and J. Zwanziger. *ABINIT: First-principles approach to material and nanosystem properties*. Computer Phys. Commun., **180**, 2582 (2009).
- [59] M. van Setten, M. Giantomassi, E. Bousquet, M. Verstraete, D. Hamann, X. Gonze and G.-M. Rignanese. *The PseudoDojo: Training and grading a 85 element optimized norm-conserving pseudopotential table*. Comp. Phys. Comm., **226**, 39 (2018).
- [60] K. Novoselov, A. Mishchenko, A. Carvalho and A. Castro Neto. *2D materials and van der Waals heterostructures*. Science, **353**, aac9439 (2016).
- [61] D. Codony, I. Arias and P. Suryanarayana. *Transversal flexoelectric coefficient for nanostructures at finite deformations from first principles*. Phys. Rev. Materials, **5** (2021).
- [62] J. P. Perdew, K. Burke and M. Ernzerhof. *Generalized Gradient Approximation Made Simple*. Phys. Rev. Lett., **77**, 3865 (1996).
- [63] D. R. Hamann, K. M. Rabe and D. Vanderbilt. *Generalized-gradient-functional treatment of strain in density-functional perturbation theory*. Phys. Rev. B, **72**, 033102 (2005).
- [64] B. Amorim and F. Guinea. *Flexural mode of graphene on a substrate*. Phys. Rev. B, **88**, 115418 (2013).
- [65] X. Wang, A. Cui, F. Chen, L. Xu, Z. Hu, K. Jiang, L. Shang and J. Chu. *Probing Effective Out-of-Plane Piezoelectricity in van der Waals Layered Materials Induced by Flexoelectricity*. Small, **15**, 1903106 (2019).
- [66] S. Kumar and P. Suryanarayana. *Bending moduli for forty-four select atomic monolayers from first principles*. Nanotechnology, **31**, 43LT01 (2020).

- [67] Y. Zhou, K. M. Rabe and D. Vanderbilt. *Surface polarization and edge charges*. Phys. Rev. B, **92**, 041102 (2015).
- [68] S. Zhou, J. Han, S. Dai, J. Sun and D. J. Srolovitz. *van der Waals bilayer energetics: Generalized stacking-fault energy of graphene, boron nitride, and graphene/boron nitride bilayers*. Phys. Rev. B, **92**, 155438 (2015).
- [69] R. S. Pease. *An X-ray Study of Boron Nitride*. Acta Crystallographica, **5**, 356 (1951).
- [70] B. Wang, Y. Gu, S. Zhang and L.-Q. Chen. *Flexoelectricity in solids: Progress, challenges, and perspectives*. Progress in Materials Science, **106**, 100570 (2019).
- [71] J. Junquera, Y. Nahas, S. Prokhorenko, L. Bellaiche, J. Íñiguez, D. G. Schlom, L.-Q. Chen, S. Salahuddin, D. A. Muller, L. W. Martin and R. Ramesh. *Topological phases in polar oxide nanostructures*. Rev. Mod. Phys., **95**, 025001 (2023).
- [72] D. Bennett, G. Chaudhary, R.-J. Slager, E. Bousquet and P. Ghosez. *Polar meron-antimeron networks in strained and twisted bilayers*. Nature Communications, **14**, 1629 (2023).
- [73] G. Kresse and J. Hafner. *Ab initio molecular dynamics for liquid metals*. Phys. Rev. B, **47**, 558 (1993).
- [74] G. Kresse and J. Hafner. *Ab initio molecular-dynamics simulation of the liquid-metal–amorphous-semiconductor transition in germanium*. Phys. Rev. B, **49**, 14251 (1994).
- [75] G. Kresse and J. Furthmüller. *Efficiency of ab-initio total energy calculations for metals and semiconductors using a plane-wave basis set*. Computational Materials Science, **6**, 15 (1996).
- [76] G. Kresse and D. Joubert. *From ultrasoft pseudopotentials to the projector augmented-wave method*. Phys. Rev. B, **59**, 1758 (1999).
- [77] S. M. Nakhmanson, A. Calzolari, V. Meunier, J. Bernholc and M. B. Nardelli. *Spontaneous polarization and piezoelectricity in boron nitride nanotubes*. Physical Review B, **67**, 235406 (2003).
- [78] G. et al. *ABINIT: First-principles approach to material and nanosystem properties*. Computer Physics Communications, **180**, 2582 (2009).
- [79] A. Edström, D. Amoroso, S. Picozzi, P. Barone and M. Stengel. *Curved Magnetism in CrI₃*. Phys. Rev. Lett., **128**, 177202 (2022).
- [80] M. Royo, K. R. Hahn and M. Stengel. *Using High Multipolar Orders to Reconstruct the Sound Velocity in Piezoelectrics from Lattice Dynamics*. Phys. Rev. Lett., **125**, 217602 (2020).
- [81] N. A. Pike, B. Van Troeye, A. Dewandre, G. Petretto, X. Gonze, G.-M. Rignanese and M. J. Verstraete. *Origin of the counterintuitive dynamic charge in the transition metal dichalcogenides*. Phys. Rev. B, **95**, 201106 (2017).